X-ray Phase Contrast Tomography

Setup and Scintillator Development

Dierks, Hanna

2023

Document Version:
Publisher's PDF, also known as Version of record

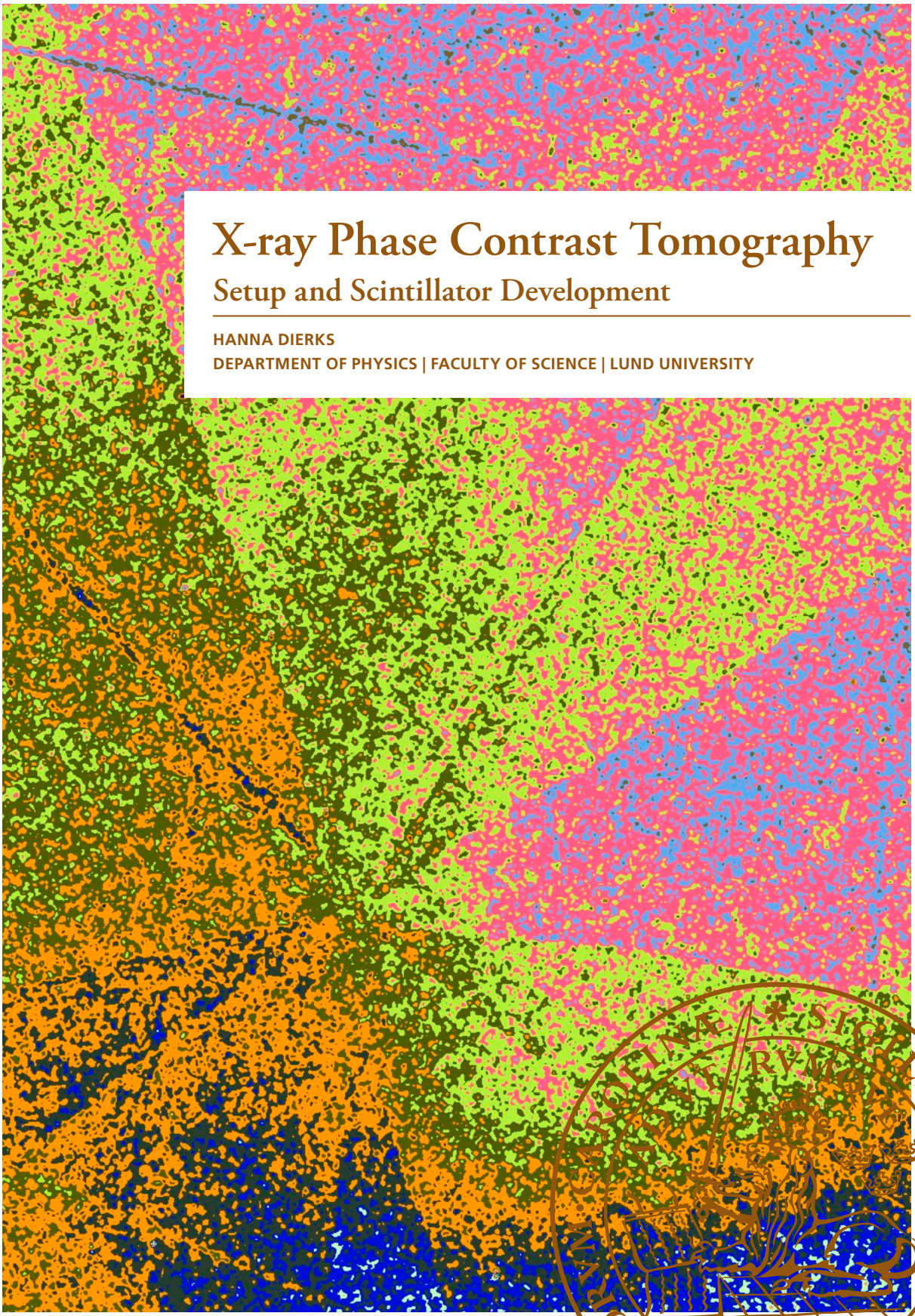

X-ray Phase Contrast Tomography

Setup and Scintillator Development

HANNA DIERKS
DEPARTMENT OF PHYSICS | FACULTY OF SCIENCE | LUND UNIVERSITY

X-ray Phase Contrast Tomography

Setup and Scintillator Development

Hanna Dierks

LUND
UNIVERSITY

DOCTORAL DISSERTATION

Doctoral dissertation for the degree of Doctor of Philosophy (PhD) at the Faculty of Science at Lund University to be publicly defended on 5th of May 2023 at 9.15 in Rydberg lecture Hall, Department of Physics

Faculty opponent
Prof. Alessandro Olivo, University College London

Organization LUND UNIVERSITY Division of Synchrotron Radiation Research Department of Physics, Box 118 S-22100 Lund	**Document name** Doctoral dissertation **Date of issue** 2023-05-05
Author Hanna Dierks	Sponsoring organization

Title and subtitle X-ray Phase Contrast Tomography – Setup and Scintillator Development

Abstract

X-ray microscopy and micro-tomography (µCT) are valuable non-destructive examination methods in many disciplines such as bio-medical research, archaeometry, material science and palaeontology. Besides being implemented at synchrotronsradiation sources, laboratory setups using an X-ray tube and high-resolution scintillation detector routinely provide information on the micrometre scale. To improve the image contrast for small and low-density samples, it is possible to introduce a propagation distance between sample and detector to perform propagation-based phase contrast imaging (PB-PCI). This contrast mode relies on a sufficiently coherent illumination and is characterised by the appearance of an additional intensity modulations ('edge enhancement fringes') around interfaces in the image. The strength of this effect depends on hardware as well as geometry parameters.

This thesis describes the development of a laboratory setup for X-ray µCT with a PB-PCI option. It contains the theoretical and technical background of the setup design as well the characterization of the achieved performance. Moreover, the optimization of the PB-PCI geometry was explored both theoretically as well as experimentally for three different setups. A simple rule for finding the optimal magnification to achieve high phase contrast for edge features was deduced. The effect of the polychromatic source spectrum und detector sensitivity was identified and included into the theoretical model.

Besides application and methodological studies, the setup was used to test and characterise new X-ray scintillator materials. Recently, metal halide perovskite nanocrystals (MHP NCs) have gained attention due to their outstanding opto-electronic performance. The main challenge for their use and commercialization is their low long-term stability against humidity, temperature, and light exposure. Here, a $CsPbBr_3$ scintillator comprised of an ordered array of nanowires (NW) in an anodized aluminium oxide (AAO) membrane is presented as a promising new scintillator for X-ray microscopy and µCT. It shows a high light yield under X-ray exposure which improves with smaller NW diameter and higher NW length. In contrast to many other MHP materials this scintillator shows good stability under continuous X-ray exposure and changing environmental conditions over extended time spans of several weeks. This makes it suitable for tomography, which is demonstrated by acquiring the first high-resolution tomogram using a MHP scintillator with the presented laboratory setup.

Key words X-rays, X-ray imaging, X-ray microscopy, X-ray detectors, laboratory setup, phase contrast, propagation-based phase contrast, PB-PCI, tomography, µCT, scintillators, perovskites, MHP

Classification system and/or index terms (if any)

Supplementary bibliographical information	**Language** English
ISSN and key title	**ISBN** 978-91-8039-590-8 (print) 978-91-8039-591-5 (electronic)
Recipient's notes	**Number of pages** 95 / Price
	Security classification

Signature Date 2023-03-20

X-ray Phase Contrast Tomography

Setup and Scintillator Development

Hanna Dierks

LUND
UNIVERSITY

Front cover: X-ray phase contrast image of a broken Si_3N_4 window. Smoothed and plotted with artistic color map © Hanna Dierks

Back cover: Illustration "Figuring things out" © Hanna Dierks

Division of Synchrotron Radiation Research
Department of Physics, Faculty of Science
Lund University

ISBN 978-91-8039-590-8 (print)
ISBN 978-91-8039-591-5 (electronic)

Printed in Sweden by Media-Tryck, Lund University
Lund 2023

To my grandma

Acknowledgements

Nothing really prepares you for what it means to pursue a PhD. Yet, we also don't start as a blank slate. When I packed my bags to move to Sweden, I also packed a suitcase full of advice, expectations and hopes. Some of these were borrowed, some inherited and some my own making. Looking back, I can see that the reality of my PhD didn't really fit into any of them. I had to grow in unexpected places, a process that wasn't always easy. But luckily, I was always surrounded by people who helped me to sort, repair, acknowledge or adjust, people that shared the good and the bad. People that helped me to pack a new suitcase, full of memories, to take with me wherever I go. And I want to thank you for that, from the bottom of my heart.

First and foremost, I want to thank my main supervisor Jesper Wallentin. You had optimism where I had doubt, you had patience where I wanted to give up and you trusted in me when I couldn't trust myself. I know it must have been difficult for you at times, but I'm immensely grateful for your guidance. Thanks for the open door and open ear, this thesis would have been impossible without you.

Similarly, I want to thank my co-supervisors, Martin Bech, Pablo Villanueva Perez, and Johan Gustafson. You all brought unique perspectives to my work and your feedback and advice have helped me to widen and deepen my understanding.

Although most of my project was rather solitary, I had the pleasure to practically work with some of my colleagues on beamtimes and sub-projects. Thank you, Zhaojun Zhang and Nils Lamers, for introducing me to the fascinating topic of perovskites. Thank you, Dima Dzhigaev, Lucas Marçal and Huaiyu Chen, for all your expertise on diffraction. And thank you, Till Dreier and Niccolò Peruzzi, for tackling the challenges of tomography with me. I also want to thank my master students, Philip Stjärneblad and Robin Krüger, who have been both help and inspiration.

Working at SLJUS has been a true pleasure – I could not have wished for better colleagues and a more welcoming workplace! The community I have found here, in- and outside the office, has been an anchor to my life in Sweden. I can't name all of you, but I'm grateful for all the shared lunches and after works, badminton matches, kick-offs and BBQs. Please continue to take care of yourself and each other!

However, some of you have long stopped being 'only' colleagues and became my second family here. From shared vacations to wedding celebrations, you have made my life immensely colourful and rich! Giuseppe – thank you for always making me feel welcome and simply being the best office mate. Giulio – thank you for bringing flavour and energy to my life. Lukas – thank you for exploring creativity with me. Sanna – thank you for laughter, units, and well-deserved breaks. Sandra – thank you for leading me out of the forest when I get lost. Virginia – thank you for being my summer, even when I felt like the rain would never end. All of you have been the greatest support I could ever wish for, and I wouldn't be here without your friendship. And not only that; you have also brought your loved ones into my life: Monica, Valeria, Veronika, Johannes, Konstantin, and Jack – thank you for helping us busy PhD students to keep in touch with the world outside of university.

Besides personal friendships, there is one person at SLJUS that plays a very special role in the life of every PhD student: Patrik! Thank you for patiently helping us with the things that most of us are notoriously bad at, it meant a lot.

There are some people that have been an immense support to me outside the university: Anna – you finally made me feel at home. Arvid – you have taught me so much about the real challenges of the world. Hedvig – thank you for walking the hardest bit of the path with me.

Finally, I want to thank my family. *Ihr wart ihr immer für mich da und habt mir Geduld, Liebe, Verständnis und Vertrauen geschenkt, danke!*

Table of Contents

List of Publications ..... **i**
Publications included in this thesis i
Publications not included in this thesis iii
Popular Science Abstract ..... **v**
Populärwissenschaftlicher Abstract ..... **vii**
List of Abbreviations ..... **xi**
1 Introduction **1**
2 Fundamentals of X-ray Imaging **5**
2.1 X-rays and their Interactions with Matter 5
2.1.1 The Atomic View: Absorption and Scattering 6
2.1.2 The Continuum View: Refractive Index 8
2.1.3 Coherence 13
2.2 Imaging Metrics 17
2.2.1 Point Spread Function and Optical Transfer Function 17
2.2.2 Contrast 18
2.2.3 Resolution 19
2.3 Tomography: Accessing 3D Information 24
2.3.1 Radon Transform and Filtered Back Projection 25
2.3.2 Reconstruction Artefacts 30
3 X-ray µCT with a Laboratory Setup **33**
3.1 Hardware and Geometry 33
3.1.1 Laboratory X-ray Sources 33
3.1.2 X-ray Detectors 35
3.1.3 Setup Geometries 36
3.1.4 State-of-the-art X-ray µCT Laboratory Setups 37
3.2 The Lab Setup at SLJUS 38
3.2.1 Instrumental Design Choices and Performance 38
3.2.2 Alignment 41

3.2.3 Outlook 43

4 Phase Contrast Imaging 45

4.1 Overcoming the Phase Problem 46
4.1.1 Grating-based Techniques (interferometric) 47
4.1.2 Mask-based Techniques (non-interferometric) 47

4.2 Propagation-Based Phase Contrast Imaging 48
4.2.1 Free-space Propagation 49
4.2.2 Transport-of-intensity Equation 50
4.2.3 Paganin Filter 52
4.2.4 Phase Contrast Tomography 54

4.3 PB-PCI at a Laboratory Setup 54
4.3.1 Divergent Beams: Fresnel Scaling Theorem 54
4.3.2 Optimization of Laboratory Setups 56

5 Scintillator Detectors 65

5.1 Scintillators 65
5.1.1 Common Scintillator Types 68

5.2 Metal Halide Perovskite Scintillators 69
5.2.1 Properties as an X-ray Scintillator 69
5.2.2 Challenges 71

5.3 $CsPbBr_3$ Nanowires in AAO 72
5.3.1 State-of-the-art $CsPbBr_3$ Scintillators 72
5.3.2 Fabrication and Characterisation of $CsPbBr_3$ NW/AAO 75
5.3.3 Tomography with a $CsPbBr_3$ NW/AAO Scintillator 77
5.3.4 Outlook 80

6 Conclusion and Outlook 81

References 83

List of Publications

Publications included in this thesis

This thesis includes the following publications which are referred to as '**paper X**' and their Roman numerals as listed here:

I. **A versatile laboratory setup for high resolution X-ray phase contrast tomography and scintillator characterization**

H. Dierks, P. Stjärneblad, and J. Wallentin,

Journal of X-Ray Science and Technology, 31: p. 1-12. (2023)

DOI: 10.3233/XST-221294.

I was the main responsible for designing and building the setup. I measured and analysed the presented data, prepared the figures, and wrote the manuscript.

II. **Experimental optimization of X-ray propagation-based phase contrast imaging geometry**

H. Dierks and J. Wallentin

Optics Express, 28(20): p. 29562-29575. (2020)

DOI: 10.1364/OE.399819

I was the main responsible for the setup, measured and analysed the presented data, prepared the figures, and wrote the manuscript.

III. Optimization of phase contrast imaging with a nano-focus X-ray tube

H. Dierks, T. Dreier, R. Krueger, M. Bech and J. Wallentin

manuscript

I measured and analysed the presented data, prepared the figures, and wrote the manuscript.

IV. Single-Crystalline Perovskite Nanowire Arrays for Stable X-ray Scintillators with Micrometer Spatial Resolution

Z. Zhang, **H. Dierks**, N. Lamers, C. Sun, K. Nováková, C. Hetherington, I. Scheblykin, and J. Wallentin

ACS Applied Nano Materials, 5(1): p. 881-889 (2022)

DOI: 10.1021/acsanm.1c03575

I measured and analysed the presented X-ray imaging data and contributed to the editing of the manuscript.

V. 3D X-ray microscopy with a $CsPbBr_3$ nanowire scintillator

H. Dierks, Z. Zhang, N. Lamers, and J. Wallentin

Nano Research 16, 1084–1089 (2023)

DOI: 10.1007/s12274-022-4633-7

I was the main responsible for the setup, measured and analysed the presented X-ray imaging data and wrote the manuscript. The scintillators were developed and fabricated by Z. Zhang.

Publications not included in this thesis

I contributed to the following publications during my PhD, which are not part of this thesis.

- **Combining Nanofocused X-Rays with Electrical Measurements at the NanoMAX Beamline**

  L. Chayanun, S. Hammarberg, **H. Dierks**, G. Otnes, A. Björling, M. Borgström, and J. Wallentin

  Crystals, 9(8): 432 (2019)

  DOI: 10.3390/cryst9080432

I participated in the beamtime at MAX IV and the editing of the manuscript.

- **X-ray in-line holography and holotomography at the NanoMAX beamline**

  S. Kalbfleisch, Y. Zhang, M. Kahnt, K. Buakor, M. Langer, T. Dreier, **H. Dierks**, P. Stjärneblad, E. Larsson, K. Gordeyeva, L. Chayanun, D. Soderberg, J. Wallentin, M. Bech, and P. Villanueva-Perez

  J Synchrotron Radiation, 29(Pt 1): p. 224-229 (2022)

  DOI: 10.1107/S1600577521012200

I participated in the beamtime at MAX IV and the editing of the manuscript.

Popular Science Abstract

You have looked everywhere. Nothing. How can your phone disappear like this? Have you lost it? However unlikely, eventually you get down and look under your bed. Nothing. But - what's that? A small box, wrapped in shiny red paper, beautiful, with a tidy little bow and a nametag. Badly hidden behind a storage container. A Christmas present! You pull it out and turn the tag. It's for you! You can't hide a smile. What did they get you? You start tugging the little bow, then stop yourself – it's still 3 weeks to Christmas. Obviously, you can't open it. You start to turn it, maybe shake it a little, but nothing gives away its content. How nice it would be to have a peek, just a short look, then seal it again. Like nothing happened. You stare at it, thinking. You know you would never manage to restore its initial condition, but…

Many things around us are like such a closed box. Things we cannot open without leaving noticeable traces. Things that are too precious to destroy. But still, we burn with curiosity to *see* what is inside.

Luckily, what is opaque under visual light can be transparent when we use a different kind of light. *X-rays* are such a light. We cannot see them directly, but they can 'help us to see.' They have such a high energy that they are transmitted through most materials. Therefore, if we were looking with X-rays the box would seem to be made of glass, not cardboard. Indeed, most of us have been in contact with this capacity of X-rays many times: dentists use X-rays when they are looking for cavities in our teeth and the security at the airport uses X-rays when they are checking our luggage. X-rays are a powerful tool, and widely used in society.

A single X-ray image can already reveal much about an object if we have a general idea what it could be. But sometimes it is not enough to look at an object from only one direction to understand how it works. We need to look at the object from different angles, to see its full three-dimensional structure. If we do this with X-rays it is called *tomography or computed tomography* (CT), a technique that we most commonly encounter at the hospital, when they look at a broken leg or hip.

As you can see, X-rays are a great tool to learn something about the inside of an object without needing to open it. But this strength can become a problem. Since they are easily transmitted, very small objects or objects that are consisting of very similar

materials can be difficult to distinguish. It is like having glass objects in a glass box – you can hardly see them. Fortunately, materials do not only absorb light, but also change its phase. We know the effect of such a phase shift from visible light lenses: they change the direction of the light, leading to a focus or de-focus, without absorbing much.

Using the phase shift to generate more contrast in the image is called *phase contrast imaging*. The phase shift causes the propagation direction of the light to change a tiny bit – enough to create a distinct fringe pattern around edges in the sample, but not enough to move or distort the overall image. If we use phase contrast, the image will show bright and dark fringes around all interfaces, which highlight the structures, but will otherwise look like an ordinary shadow image. Like someone took a pen and marked the outlines with a black and white line. We can use a computer algorithm to translate these fringes to a more pronounced contrast, proportional to the phase shift of the material.

As mentioned, X-rays are invisible to the human eye. So, we need a special kind of detector to make them visible for us. There are materials, called *scintillators,* that start glowing visible light when they are exposed to X-rays, that can be used as a screen to detect them. Although many such materials exist, they often are not good enough to detect all X-ray light. Scientists therefore continuously try to find better materials.

In my PhD project I have worked on these three topics: X-ray CT, phase contrast, and scintillator development. They came together in a very practical sense: I have been building a laboratory setup for X-ray microscopy and CT, with a phase contrast modality and the option to test different scintillators. Essentially, I have built a machine that helps me to look inside tiny, closed boxes without needing to open them. These boxes could be anything, for example, a blueberry seed, or filter layers in a covid mask, or even rock grains from a meteoroid impact site (but unfortunately no Christmas presents yet). I planned and built the setup, made it work, improved it, and then used it with samples. This included tweaking the geometry to get the best phase contrast and finally testing newly developed detectors materials. The results of my work are summarized in my publications and contextualized in this thesis.

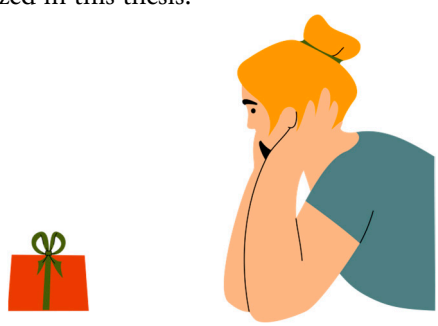

Populärwissenschaftlicher Abstract

Du hast überall nachgesehen. Nichts. Wie kann dein Handy einfach so verschwinden? Hast du es verloren? Egal wie unwahrscheinlich, irgendwann bückst du dich und schaust unters Bett. Wieder nichts. Aber - was ist das? Eine kleine Schachtel, verpackt in rotes Geschenkpapier, hübsch, mit einer kleinen Schleife und Namenschild. Schlecht versteckt hinter einer Lagerbox. Ein Weihnachtsgeschenk! Du ziehst es hervor und wendest das Namensschild. Es ist für dich! Du musst lächeln. Was wohl drin ist? Du beginnst sacht an der Schleife zu ziehen, doch dann hältst du inne – Weihnachten ist erst in 3 Wochen. Natürlich kannst du es nicht öffnen. Du drehst es in deinen Händen, schüttelst ein wenig, aber nichts verrät den Inhalt. Wie schön es wäre einen Blick hineinzuwerfen, nur ganz kurz, und es dann wieder zu verschließen. Als wäre nichts geschehen. In Gedanken versunken starrst du auf das Geschenk. Du weißt, dass du es nicht wieder in seinen Ausgangszustand zurückversetzen könntest, aber…

Viele Dinge in unserer Umgebung sind wie solch eine verschlossene Schachtel. Dinge, die wir nicht öffnen können, ohne Spuren zu hinterlassen. Dinge, die zu wertvoll sind, um zerstört zu werden. Aber dennoch, wir brennen vor Neugier *hineinsehen* zu können.

Glücklicherweise können Objekte, die unter sichtbarem Licht undurchsichtig sind, transparent unter anderen Arten von Licht sein. *Röntgenstrahlung* ist so eine Art von Licht. Obwohl unsichtbar fürs menschliche Auge, kann sie uns „helfen zu sehen“, denn Röntgenstrahlung hat eine so hohe Energie, dass sie die meisten Materialien durchdringt. Das sieht dann aus, als bestünde die Schachtel aus Glas, nicht Karton. Die meisten von uns sind schon in Kontakt mit dieser Eigenschaft von Röntgenstrahlung gekommen: beim Zahnarzt benutzen wir sie, um Karies aufzuspüren, und die Sicherheitskontrolle am Flughafen durchleuchtet damit unser Gepäck. Bildgebung mit Röntgenstrahlung ist eine praktische und weit verbreitete Methode.

Eine einzelne Röntgenaufnahme kann bereits viel über ein Objekt verraten, wenn man eine generelle Idee hat, was das Objekt sein könnte. Doch manchmal reicht es nicht aus nur aus einer Richtung zu schauen, um zu verstehen, wie etwas funktioniert. Man muss verschiedene Blickwinkel kombinieren, um die gesamte dreidimensionale Struktur zu sehen. Wenn man dies mit Röntgenstrahlung tut, bezeichnet man es als

Computer Tomographie (CT), eine Methode, die wir vorranging im Krankenhaus antreffen, wenn gebrochene Knochen untersucht werden.

Röntgenstrahlen sind also ein großartiges Hilfsmittel, um etwas über das Innere eines Objekts zu lernen, ohne es öffnen zu müssen. Diese Stärke kann jedoch auch zum Problem werden. Da Röntgen viel Materialien so leicht durchdringen, können kleine Objekte oder Objekte, die aus sehr ähnlichen Materialien zusammengesetzt sind, schlecht auseinandergehalten werden. Man kann sich das vorstellen, als betrachtete man den Schatten von Glasgegenständen in einer Glasschachtel – der Kontrast ist niedrig. Glücklicherweise jedoch absorbieren Materialen nicht nur, sondern sie verändern auch die Phase des Lichts. Wir kennen diesen Effekt des Phasenverschubs von Linsen: sie verändern die Richtung des Lichts, fokussieren oder defokussieren aber absorbieren kaum.

Diesen Phasenverschub kann man nutzten, um einen höheren Kontrast im Bild zu erhalten, was man als *Phasenkontrast Bildgebung* bezeichnet. Der Phasenverschub ändert die Ausbreitungsrichtung des Lichts ein klein wenig – genug um eine markante Struktur um Grenzflächen im Objekt zu erzeugen, aber nicht genug um das Bild als solches zu bewegen oder zu verzerren. Bilder mit Phasenkontrast zeichnen sich durch helle und dunkle Linien um alle Kanten im Bild aus, welche die Struktur betonen. Das Bild sieht also aus wie ein klassisches Röntgenbild in dem jemand mit einem hellen und dunklen Stift die Kanten nachgezogen hat. Mit Hilfe eines Computeralgorithmus kann man dies dann in ein Bild umwandeln, in dem der Kontrast höher und proportional zum Phasenverschub der Probe ist.

Wie erwähnt sind Röntgenstrahlen unsichtbar für das menschliche Auge. Daher benötigt man eine besondere Art von Detektor, um sie sichtbar zu machen. Glücklicherweise gibt es Materialien, die anfangen zu leuchten, wenn sie mit Röntgen bestrahlt werden. Diese so-genannten *Szintillatoren* können als Schirm benutzt werden, um Röntgenstrahlen zu messen. Obwohl solche Materialen existieren, sind viele von ihnen nicht sehr effizient. Forscher sind daher stetig auf der Suche nach besseren Materialien.

Während meiner Doktorarbeit habe ich an diesen drei Themenfeldern gearbeitet: Röntgen CT, Phasenkontrast und Szintillatorentwicklung. Für mich waren sie auf sehr praktische Art verknüpft: ich habe einen Laboraufbau für Röntgenmikroskopie und CT mit einer Phasenkontrastmodalität und der Option verschiedene Szintillatoren zu testen, gebaut. Im Grunde ist es eine Maschine, die ermöglicht in kleine, verschlossene Schachteln zu blicken, ohne sie zu öffnen. Diese „Schachteln“ können quasi alles sein, z.B. der Samen einer Blaubeere, die Filter in einer Covid Maske oder Steinchen vom Krater eines Meteoriten (aber leider bisher keine Weihnachtsgeschenke). Ich habe den Aufbau geplant und gebaut, ihn zum Laufen gebracht und verbessert, und schlussendlich benutzt, um Proben zu vermessen. Dies beinhaltete die Optimierung

der Geometrie, um den besten Phasenkontrast zu erhalten und das Testen von neu entwickelten Szintillatoren. Die Ergebnisse meiner Arbeit sind in meinen Veröffentlichungen zusammengefasst und werden in dieser Dissertation in Kontext gesetzt.

List of Abbreviations

1D, 2D, 3D	1-dimensional, 2-dimensional, 3-dimensional
AAO	anodized aluminium oxide
ART	algebraic reconstruction technique
CDI	coherent diffractive imaging
CMOS	complementary metal-oxide-semiconductor
CNR	contrast-to-noise ratio
CT	computed tomography
CTF	contrast transfer function
ESF	edge spread function
FBP	filtered back projection
FFT	fast Fourier transform
FRC	Fourier ring correlation
FSC	Fourier shell correlation
FOV	field-of-view
FWHM	full width at half maximum
GGG	gadolinium gallium garnets
JIMA	Japanese institute of metrology (test pattern)
LSF	line spread function
MHP	metal halide perovskite
MTF	modulation transfer function
µCT	micro computed tomography
NA	numerical aperture

NC	nanocrystal
NW	nanowire
OTF	optical transfer function
PB-PCI	propagation-based phase contrast imaging
PhTF	phase transfer function
PL	photoluminescence
PSF	point spread function
SC	single crystal
SNR	signal-to-noise ratio
TIE	transport of intensity equation
QD	quantum dot
QY	quantum yield

1 Introduction

"One image is worth a thousand words" – most of us will have encountered this popular saying. And as it goes with such sayings, there is some truth to it. Who has never struggled explaining something complex that becomes utterly obvious with the help of an image?

Today, we live in an increasingly visual society where images have power. We often prefer images over the written word because they feel familiar and can convey dense information instinctively – both in our everyday life and in science. Images have always been a big part of how we make sense of the world and as such they also play their role in the scientific quest for knowledge and understanding. We strive not only to measure but also to *see* the world around us clearer, faster, and more reliably, from astronomic scales down to atoms. Accordingly, imaging technologies have undergone an astonishing development in the past century. We have become able to access the world beyond what we can see with our own eyes, broadening our perception with modern technologies on both sides of the visible spectrum. Seeing and understanding what has previously been invisible is one of the greatest wonders of science.

Figure 1.1: **X-ray imaging.** a) The bones of a hand with a ring on one finger, viewed through X-ray. Photoprint from radiograph by W.K. Röntgen, 1895. Attribution-NonCommercial 4.0 International (CC BY-NC 4.0) b) Aerial view of the MAX IV synchrotron radiation source in Lund, Sweden, 2018 (photo by Perry Nordeng, Lund University Image and Media Bank), c) X-ray micro tomography lab setup at Lund University.

In this context it is not difficult to imagine how Wilhelm Conrad Röntgen must have felt when he looked at that famous X-ray radiograph showing the bones inside his wife's hand (see fig. 1.1a). It was the first time that an opaque object, moreover a living one,

revealed its inner structure without the need to open or destroy it. That day in the end of 1895, just as a new century was around the corner, a new kind of radiation, the *X-rays*, was about to change the way we see the world around us.

Since this fortunate discovery more than 125 years ago, X-rays have proven to be a valuable tool to answer diverse scientific questions. Applications stretch across the disciplines from basic physics, chemistry, to biology and medicine. Like visible light, X-rays can be used as a probe for chemical and structural investigations, such as spectroscopy and diffraction. Nevertheless, they are best-known for their application in imaging, mostly at the hospital or airport.

Today, we can access not only 2D but 3D information via X-rays, thanks to the invention of *computed tomography* (CT).[1] Like X-rays themselves, this invention was rewarded with a Nobel prize and today CT imaging is an essential diagnostic technique, helping to save lives every day. Moreover, it finds applications in various disciplines, such as archaeology,[2, 3] material science,[4, 5] bio-medical imaging,[6-9] industrial quality control,[10] and palaeontology.[11] Whenever the integrity of the sample is important, X-ray imaging is the method of choice.

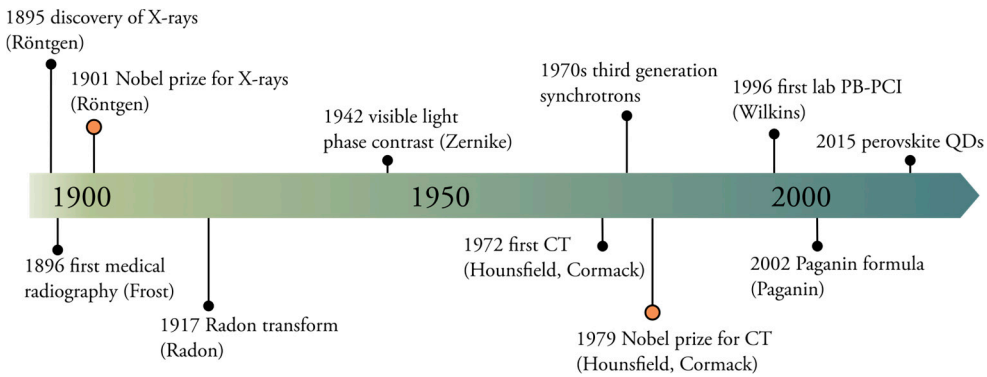

Figure 1.2: Milestones in X-ray imaging. Selected as relevant for this thesis.

Over the last century, X-ray imaging has also become an established *microscopy* technique, striving to provide the highest possible resolution. Using laboratory sources and modern detectors, X-ray microscopes and µCT scanners routinely provide micrometre spatial resolutions, and some are even pushing towards nano.[12]

An important step towards even higher resolution and shorter measurement times came with the advent of large-scale X-ray sources in the 1970s, the *synchrotron radiation sources* (see fig. 1.1b).[13] Although synchrotron radiation was first discovered as an unwanted side effect in particle accelerators, today dedicated synchrotron radiation facilities provide up to ten orders of magnitude higher intensities than conventional X-

ray tubes, collimated beams, and an unprecedented degree of coherence. However, the high brilliance comes at a price – quite literally: building a synchrotron radiation source is a hundreds-of-million-euro endeavour. Accordingly, the number of these sources around the world is limited and the available measurement time needs to be shared within the research community. This restricted access often does not meet the demand. Laboratory setups with X-ray tubes (see fig. 1.1c) are therefore still an important complementary and accessible resource to their sister-setups at synchrotron radiation sources.

Besides the resolution, one of the main challenges in X-ray microscopy is the contrast. The low attenuation of X-rays in most materials allows us to see the inside of visually opaque objects but also provides only low contrast. This becomes problematic if the sample is small or made from materials with a similar density and attenuation. For example, traditional absorption imaging at the hospital can easily distinguish between bone and tissue, but different tissue types such as cancerous and healthy tissue are difficult to differentiate, which often makes the use of additional contrast agents necessary.

A way to overcome this inherent limitation of absorption contrast imaging is to use a different contrast mechanism based on the *phase shift* in the sample. Unfortunately, the phase shift cannot be measured directly, but indirect measurement methods exist. These are based for example on gratings, masks, or free-space propagation, and make it possible to extract phase information from intensity measurements. At laboratory setups the experimental simplicity of *propagation-based phase contrast imaging* (PB-PCI) is especially intriguing since no additional optical elements or multiple exposures are necessary.[14]

Indeed, many strategies to improve X-ray microscopy are currently explored. Besides finding new measurement approaches, the technological improvement of the hardware components keeps changing the research field. Innovative lab sources, aiming at higher brightness and smaller spot sizes, as well as new X-ray detectors with lower noise, higher sensitivity and resolution are constantly developed. These strategies are complementary and involve a joint effort of experts ranging from engineering to material science.

Detectors for X-ray imaging can be either direct, using a semiconductor sensor that is sensitive to X-rays, or indirect, using a *scintillation* screen that converts X-rays to visible light which is then read-out via an optical sensor. The bottleneck of these detectors is often the scintillator itself and new materials are constantly explored.

Recently, *metal halide perovskites* (MHP) have gained increasing attention as promising candidates for a new generation of X-ray scintillators. They are easy to fabricate and have demonstrated a remarkably high light yield and fast scintillation.[15] Therefore, research on MHP scintillators is a fast-moving field and the prompt testing of new scintillators in real imaging scenarios is important to keep up with the pace of

the fabrication methods. Synchrotron radiation measurements often cannot offer the necessary feedback speed because the delay times between proposals and actual experimental sessions are long. Luckily, laboratory setups can fill this gap if they provide the necessary experimental flexibility.

A major part of my PhD was designing, building, and using a laboratory µCT setup with PB-PCI mode and the option to mount and assess scintillators in real imaging scenarios. This thesis documents this process. It consists of an introductory *kappa* (Swedish for 'cape or wrap') to provide background and context for the collection of scientific publications written during my PhD. The publications can be found in the second half of the print version or online under the given references. The *kappa* starts with a general introduction to X-ray imaging and tomography (chapter 2) and then follows the three main topics of my PhD: the µCT setup (chapter 3, **paper I**), phase contrast imaging (chapter 4, **paper II** & **III**), and scintillator development (chapter 5, **papers IV** & **V**). All topics are connected to the setup, which is the red thread as well as the physical manifestation of my PhD project. It is introduced in detail in **paper I** and referenced throughout the *kappa.*

2 Fundamentals of X-ray Imaging

In this chapter I will introduce the fundamentals of X-ray imaging and define relevant terminology. The chapter is divided in three sections: X-ray interaction with matter, imaging metrics and tomography.

The first section gives a brief overview of the most important properties of X-rays and how they interact with matter. The second section introduces the most important imaging metrics and how they can be extracted from an image. These metrics are not limited to X-ray imaging but apply to any full-field imaging technique. They serve as tools to practically evaluate the image quality. Finally, the basic math behind tomography is presented, together with an overview of the most common artefacts that can be encountered in real experiments.

For a more exhaustive treatment of these topics I refer the reader to relevant textbooks on X-rays.[16, 17]

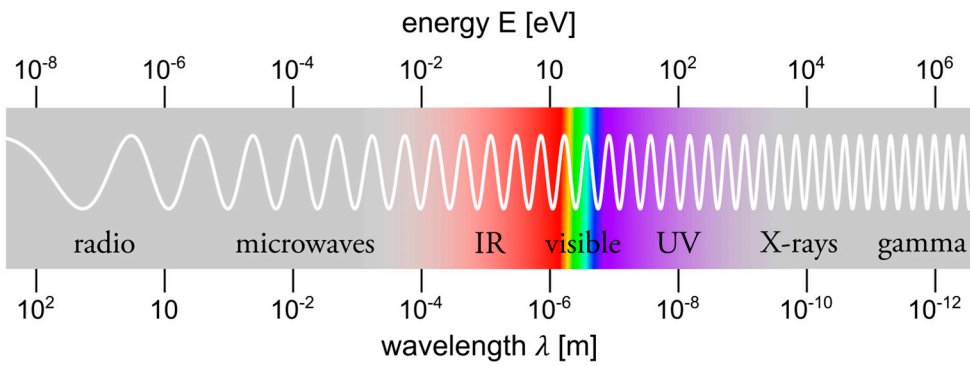

Figure 2.1: The electro-magnetic spectrum. Energies and wavelengths from radio waves to gamma rays. X-rays are located on the high-energy side of visible light, between UV and gamma.

2.1 X-rays and their Interactions with Matter

X-rays are electro-magnetic waves, i.e., synchronized oscillations of electric and magnetic fields. Conceptually this makes them similar to other forms of radiation, like visible light or radio waves, but they have a much higher frequency (and accordingly

energy). Their energy E is in the order of kilo electron volts (keV) and wavelengths λ in the order of 0.1 nm ($E[\mathrm{keV}] = \frac{hc}{\lambda} \approx \frac{1.2398}{\lambda[\mathrm{nm}]} = 12.4\ \mathrm{keV}$), which is high enough to ionize core electrons of an atom. Spectrally they are located on the high energy (short wavelength) side compared to visible light (see fig. 2.1). In the following I will focus on the energy range between 5-50 keV (0.25-0.025 nm).

Mathematically, they can be described by Maxwell's equations and are subject to the wave-particle duality, which means that they show wave- as well as particle-like behaviour. In the following I will use both descriptions interchangeably, depending on which view gives better insight into the process.

In this thesis I will work with a scalar description of waves instead of an electromagnetic vector field, thus neglecting all polarization effects. Scalar waves obey the scalar wave equation (d'Alembert equation) that can be derived from Maxwell's equations. Since a full derivation is outside of the scope of this thesis, I refer the reader to relevant textbooks on optics such as Saleh & Teich or Born & Wolf.[18, 19]

The scalar wave equation in vacuum is

$$\left(\frac{1}{c^2}\frac{\partial^2}{\partial t^2} - \nabla^2\right)\psi(x, y, z; t) = 0. \tag{2.1}$$

Mathematically this defines what a wave is, i.e., any wave is a solution to this equation. The simplest wave solving this equation is a *plane wave*

$$\psi(\vec{x}; t) = \psi_0 \exp\left(-i\vec{k}\vec{x}\right)\exp(i\omega t) \tag{2.2}$$

of frequency ω traveling along the propagation direction that is described by the wavevector $\vec{k}$. The planes of constant phase are called wavefronts and are normal to the wavevector. The magnitude of the wavevector $k = \left|\vec{k}\right| = \frac{2\pi}{\lambda} = \frac{\omega}{c} = \frac{E}{\hbar c}$ is linked to the wavelength λ, frequency ω and energy E. The amplitude ψ_0 depends on the field strength and the intensity is given by the square of the amplitude $I_0 = |\psi_0|^2$.

Alternatively, in the particle view a wave can be described as a flux of photons in direction $\vec{k}$, each carrying the energy $E = hc/\lambda$ and momentum $\vec{p} = \hbar\vec{k}$.

2.1.1 The Atomic View: Absorption and Scattering

In the energy range we are considering (5-50 keV), X-rays mainly interact with the electrons in the atom, while the interaction with heavier protons and neutrons can be disregarded.

On the atomic level, the interaction of X-rays with matter can be grouped into two kinds of processes: scattering and absorption. Element-specific *cross sections* are used to describe the relative likelihood for these processes depending on the energy of the radiation.

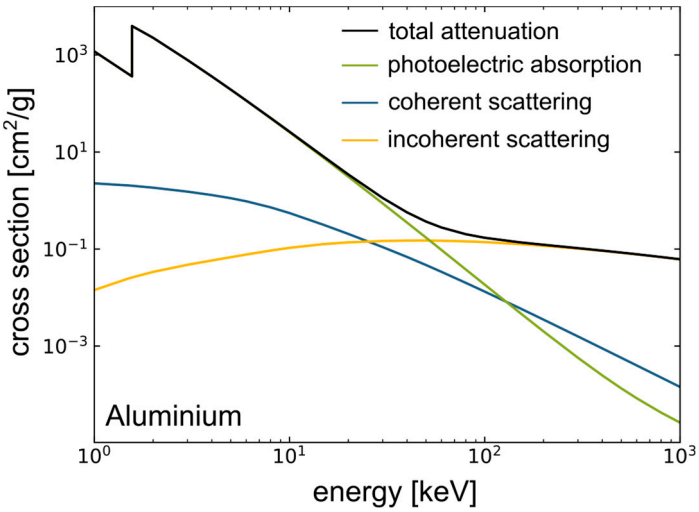

Figure 2.2: X-ray attenuation cross sections of aluminium plotted over energy. Data for aluminium from 1 keV to 1 MeV extracted from the NIST database.[20] Note the absorption edge at 1.5 keV and the increasing contribution of incoherent scattering. Effects at higher energies (pair production) are not included here, because they are not relevant to this thesis.

When X-rays *scatter* their propagation direction (wavevector $\vec{k}$) changes. Scattering processes can be divided into elastic and inelastic scattering. Elastic scattering leaves the energy of the outgoing X-rays unchanged, while inelastic scattering includes an energy transfer, and the outgoing wave/photon has a lower energy compared to the incoming.

The elastic scattering on a single, free electron is known as *Thomson scattering* and is independent of the energy of the incoming photon. The electron is forced to oscillate in the electric field of the incident wave, thus becoming a source of radiation itself with a phase difference of π. The efficiency of the scattering process is described by the *differential scattering cross-section*, which depends on the orientation between the polarization of the incoming X-rays and the observation direction.

However, for bound electrons in atoms the description of elastic scattering needs to be corrected. This is formulated in the *atomic form factor*, which includes both the effect of the spatial arrangement of electrons in the atom (charge distribution), as well as the fact that these atoms are not free. The first effect can be modelled as an integration over the electron density with a factor that accounts for the phase difference between the respective volume elements. Mathematically, this is recognizable as the Fourier

transform of the charge distribution and depends on the scattering vector $\vec{Q} = \vec{k}' - \vec{k}$, where $\vec{k}'$ is the wavevector of the scattered wave.

Moreover, since the electrons are bound, they can be described classically as a 'forced harmonic oscillator' and their reaction to the driving field will be damped. Accordingly, an additional energy dependent *dispersion correction* is needed. This introduces a dissipation of energy, expressed in the imaginary part of the atomic form factor, which is related to the absorption and shows resonances at the absorption edges of the atom (see below).

During inelastic scattering energy is transferred between the X-rays and the scatterer. Inelastic scattering of X-rays on a resting electron is known as *Compton scattering*, which is angle dependent. In general, inelastic scattering becomes more likely with higher energies, compared to elastic scattering (see fig. 2.2). In contrast to elastic scattering, which is a coherent process, meaning that waves scattered at different atoms in a crystal add up coherently when the diffraction condition is fulfilled, Compton scattering is incoherent.

Besides being scattered, X-rays can be *absorbed*. When an X-ray photon is absorbed, it transfers all its energy to the atom by exciting an electron. The energy of X-rays is high enough for photoelectric absorption, which means the excitation of inner shell electrons to the vacuum energy level and thus ionization of the absorbing atom. The absorption cross section for a material decreases with X-ray energy but shows sharp increases, the so-called *absorption edges*, whenever the energy exceeds the binding energy of the next more tightly bound electron shell (see fig. 2.2).

Secondary processes such as *fluorescence* and *Auger electron emission* can follow the absorption. After the emission of the electron the remaining inner shell vacancy (hole) is filled by an electron from a higher shell, to reach an energetically more favourable state of the atom. The energy freed by this transition is simultaneously emitted in form of a fluorescence photon or, alternatively, excites another outer shell electron that is emitted (Auger electron). Fluorescence and Auger emission are competing processes and their respective yields depend on the element. Auger emission is dominant in low-Z elements, while high-Z elements show mostly fluorescence.

2.1.2 The Continuum View: Refractive Index

Complementary to the atomic view one can describe X-ray interactions with matter on a continuum level. In this view the whole material, which can be a single chemical element or a compound, is characterised by its *complex refractive index* $n = 1 - \delta + i\beta$, where both $\delta, \beta > 0$. The real part δ describes the elastic scattering while the imaginary part β signifies the absorption in the material. In this macroscopic picture, working in

the wave description, the scattering is associated with a *phase shift* of the incoming wave (see fig. 2.5) and the absorption with a *damping* of the amplitude. Note, that for X-rays the real part of the refractive index $1-\delta$ is smaller but close to 1, which means that the phase velocity c/n of the wave inside a material is higher compared to the vacuum propagation. This does not contradict relativity theory, since the group velocity is still below the speed of light c. However, it entails the possibility of total external reflection. It is worth noting that δ is small compared to unity (order 10^{-5} in solids), and the imaginary part β is usually several orders of magnitudes smaller than δ (see fig. 2.3).

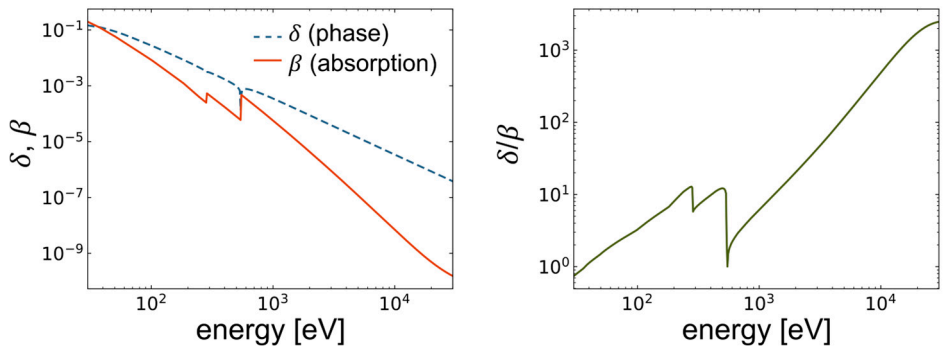

Figure 2.3: Real and imaginary component of the complex index of refraction $n = 1 - \delta + i\beta$ for cellulose ($C_{12}H_{20}O_{10}$, mass density 1.5 g/cm³). Note the absorption edges at low energies due to C and O and the different slopes of δ and β.[21]

Let us now briefly review what happens to a wave travelling in z direction when it passes through an object with refractive index $n(x,y,z)$ and thickness $T(x,y)$, as illustrated in fig. 2.4.[17]

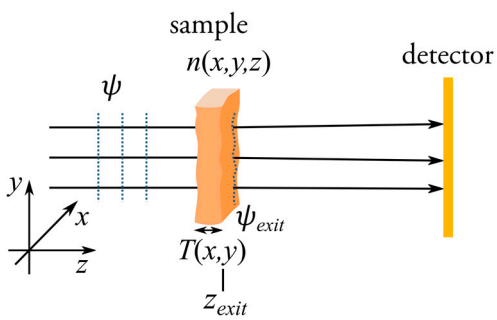

Figure 2.4: Geometry and coordinate system for X-ray imaging described in this thesis. The optical axis is parallel to the z direction and the sample is described as a distribution of the refractive index $n(x,y,z)$ over a thickness $T(x,y)$. Note that here the illumination is assumed to be a plane wave ψ.

The Helmholtz Equation

As mentioned above, the behaviour of electro-magnetic waves in vacuum or in the presence of matter can be described by the wave equation. The wave equation (2.1) has a temporal as well as a spatial component, but here we are only interested in the spatial part, which is described by the *Helmholtz equation*. To derive the Helmholtz equation from eq. (2.1), one assumes that the wave function $\psi(x, y, z;\ t)$ is separable into two functions, one only dependent on time t and the other only on space (x, y, z). This is equivalent to assuming that the polychromatic wavefield is a superposition of monochromatic fields ψ of wavelength $\lambda = \frac{2\pi}{k}$. The Helmholtz equation or 'time-independent wave equation' in vacuum is then

$$(k^2 + \nabla^2)\psi(x, y, z) = 0. \tag{2.3}$$

In the presence of matter, it includes the refractive index $n(x, y, z; \lambda)$ to account for scatterers and is called the *inhomogeneous Helmholtz equation:*

$$(k^2 n^2(x, y, z; \lambda) + \nabla^2)\psi(x, y, z) = 0. \tag{2.4}$$

To solve this for a normalised incident plane wave $\psi_0 = \sqrt{I_0}\exp(ikz)$ travelling along the optical axis z, we assume that the outgoing wave after passing through the sample is still similar to the incoming wave. This means that its wave function can also be described by a plane wave but modulated with an envelope $\hat{\psi}$ that accounts for the interaction with the sample

$$\psi(x, y, z) = \hat{\psi}(x, y, z)\exp(ikz)\ . \tag{2.5}$$

Inserting this *Ansatz* into eq. (2.4) and performing the Laplacian on the plane wave part we find a new differential equation for the envelope $\hat{\psi}$

$$\left[2ik\frac{\partial}{\partial z} + \nabla^2 + k^2(n^2 - 1)\right]\hat{\psi}(x, y, z) = 0. \tag{2.6}$$

Next, we try to solve this equation by simplifying it based on two common approximations: the paraxial and the projection approximation.

The Paraxial Approximation

To understand the paraxial approximation, it is instructive to use the picture of rays instead of waves. A ray can be understood as the trajectory that is parallel to the phase gradient or a vector that points along the propagation direction. The paraxial

approximation assumes that the envelope of the wave function is 'beamlike,' which means that it varies negligibly along the propagation direction compared to the variations perpendicular to it. This is equivalent to assuming that all rays only make a small angle with respect to the optical axis (here z).

Mathematically the *paraxial approximation* is expressed by neglecting the second derivative in the Laplacian along the propagation direction z:

$$\nabla^2 = \frac{\partial^2}{\partial x^2} + \frac{\partial^2}{\partial y^2} + \frac{\partial^2}{\partial z^2} \approx \frac{\partial^2}{\partial x^2} + \frac{\partial^2}{\partial y^2} \equiv \nabla_\perp^2. \tag{2.7}$$

The Laplacian is thus approximated as the *transverse Laplacian* $\nabla_\perp^2$ and the inhomogeneous Helmholtz equation becomes the *paraxial inhomogeneous Helmholtz equation*

$$\left[2ik\frac{\partial}{\partial z} + \nabla_\perp^2 + k^2(n^2 - 1)\right]\hat{\psi}(x, y, z) \approx 0. \tag{2.8}$$

Projection Approximation

The projection approximation assumes that the wave's direction within the sample is not changed compared to vacuum, only its phase and amplitude. This is valid if the sample is weakly scattering and is stricter than the paraxial approximation above. It allows us to express the phase and amplitude of the wave at the exit surface of the sample solely in terms of the phase and amplitude changes along the ray path. This is equivalent to assuming that the thickness $T(x, y)$ of the sample is projected along z onto a single plane.

Mathematically, the *projection approximation* means neglecting the coupling of neighbouring rays, which is equivalent to neglecting the transverse Laplacian $\nabla_\perp^2$ in the paraxial equation (2.8)

$$\left[2ik\frac{\partial}{\partial z} + k^2(n^2 - 1)\right]\hat{\psi}(x, y, z) \approx 0. \tag{2.9}$$

Physically this means to exclude multiple interactions.

This simplified expression can now be solved via integration. If we furthermore consider that $n = 1 - \delta + i\beta$ and δ and β are small compared to unity, we can neglect their second orders, so $n^2 \approx 1 - 2(\delta - i\beta)$.

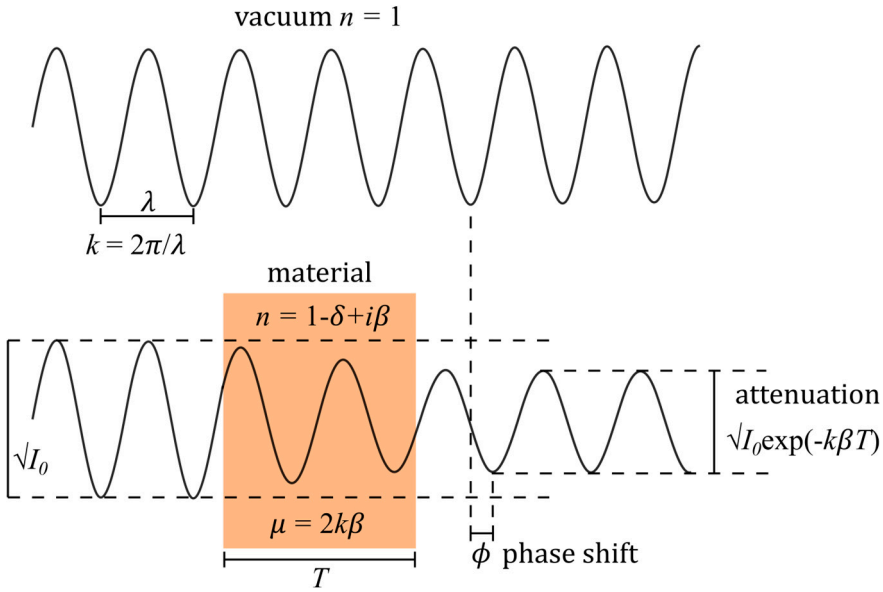

Figure 2.5: X-ray interaction with matter on the continuum level. When a wave passes through a homogeneous slab of material with refractive index $n = 1 - \delta + i\beta$ the wave is attenuated (damped) as well as phase shifted compared to a wave propagating the same distance in vacuum. For a homogeneous material the attenuation is described by the Beer-Lambert law (see eq. (2.12)).

Under these assumptions, a solution for the envelope $\hat{\psi}_{exit}$ at the exit surface z_{exit} of the sample after passing through a sample of thickness $T(x, y)$ solely depends on the initial envelope and the integrated refractive index:

$$\hat{\psi}_{exit} \approx \exp\left(-ik \int_{z_{exit}-T(x,y)}^{z_{exit}} \left(\delta(x,y,z) - i\beta(x,y,z)\right) dz\right) \hat{\psi}\left(x, y, z_{entry}\right) \quad (2.10)$$

For the incoming plane wave ψ_0 from above the envelope is a constant $\hat{\psi}\left(x, y, z_{entry}\right) = \sqrt{I_0}$ and the exit wave can be written as $\psi_{exit} = \sqrt{I_{exit}(x,y)}\exp\left(i\phi_{exit}(x,y)\right)$. The intensity in the exit plane $I_{exit} = |\psi_{exit}|^2$ can then be expressed as

$$I_{exit}(x,y) = I_0 \exp\left(-2k \int_{z_{exit}-T(x,y)}^{z_{exit}} \beta(x,y,z) dz\right). \quad (2.11)$$

If the sample is a homogeneous slap of material of uniform thickness $T(x, y) = T = const.$ the intensity I_{exit} further simplifies to an exponential decay with the linear absorption coefficient $\mu = 2k\beta$ and thickness T. This is the *Beer-Lambert law*

$$I_{exit} = I_0 e^{-\mu T}. \tag{2.12}$$

Similarly, the integrated phase shift ϕ_{exit} after passing through the slab is

$$\phi_{exit} = -k \int_{z_{exit}-T(x,y)}^{z_{exit}} \delta(x,y,z)\, dz = -k\delta T. \tag{2.13}$$

This is illustrated in fig. 2.5: the wave is damped in amplitude and shifted in phase compared to the vacuum propagation.

Linking this back to the atomic view this means that measuring the absorption of a sample gives information about the integrated electron density ρ_{at} and attenuation cross section σ_a: $\mu = \rho_{at}\sigma_a$. The phase shift can be understood as a small refraction or tilt of the wavefront due to scattering. Both phase shift and absorption can generate image contrast, as we shall see in chapter 4.

2.1.3 Coherence

The previous chapter derived a description of a single plane wave interacting with a material. But what happens when several waves overlap in time and space? Under certain circumstances they can combine to form a new wavefront which differs from a simple superposition. This effect is called *interference*. The ability of waves to interfere is expressed in their *coherence* (from Latin *cohaerentia*, 'to stick together'). Two types of coherence can be distinguished: longitudinal coherence and transversal/spatial coherence. The longitudinal coherence depends on the bandwidth or wavelength spread. The transverse/spatial coherence is linked to the spread in propagation direction of the waves, which in turn is linked to the angular distance of their source points.

Electro-magnetic radiation is not fully coherent or fully incoherent but has a certain degree of *partial coherence*. Nevertheless, it is helpful to define a *coherence length* as a simplified threshold for judging the visibility of interference effects.

Longitudinal Coherence: Polychromatic Radiation

As mentioned above, the longitudinal coherence depends on how close two waves are in wavelength. Imagine two plane waves with the same propagation direction: one wave has the wavelength λ, the other a slightly shorter wavelength $\lambda - \Delta\lambda$ (see fig. 2.6). These two waves will be progressively out of phase. The *longitudinal coherence length* is defined as the distance along the propagation direction at which the phase difference is exactly π (fully out of phase)

$$L_L = \frac{\lambda^2}{2 \cdot \Delta\lambda}. \tag{2.14}$$

It is inversely proportional to the spectral bandwidth $\Delta\lambda$. Radiation with a broad spectrum therefore has a lower degree of coherence than quasi-monochromatic radiation.

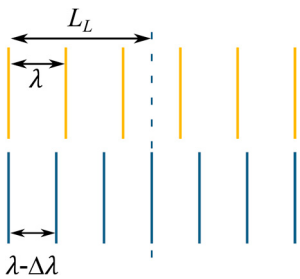

Figure 2.6: Longitudinal coherence. The coherence length is defined as the distance at which two waves with slightly different wavelengths λ and $\lambda - \Delta\lambda$ are half a period out of phase.

Spatial Coherence: Young Double Slit Interferometer

An intuitive understanding of spatial coherence can be gained by considering the Young double-slit interferometer, illustrated in fig. 2.7a. For simplicity we restrict ourselves to the 2D case, following the derivation by Paganin.[17].

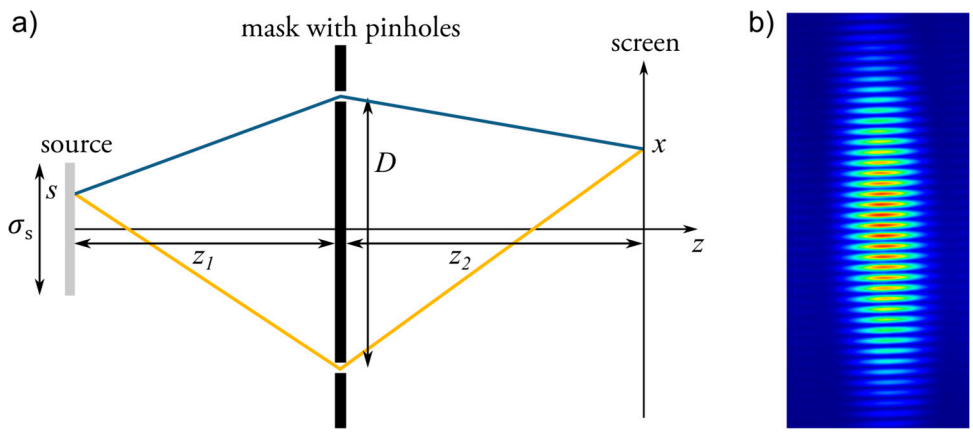

Figure 2.7: Spatial coherence. a) Schematic of the Young double slit interferometer using an incoherent source of size σ_s. The two pinholes (separation D) are located in the mask at distance z_1 from the source and the interference pattern is observed on a screen at a distance z_2 behind the mask. The two possible ray paths from a source point s to a screen point x through the respective pinholes are indicated in blue and yellow. b) Detector image of a double slit experiment at the NanoMax beamline at the MAX IV synchrotron radiation source. The slit distance was smaller than the coherence length and pronounced interference fringes are visible. The double slit pattern is modulated with the single slit interference pattern coming from the slit shape.

Imagine a fully incoherent monochromatic line source σ_s, a thin opaque mask at a distance z_1 with two identical small pinholes and an observation screen at a distance z_2 from the mask. The distance between the pinholes is D, see fig. 2.7a.

We can calculate the length difference between the two possible ray paths going from a source point s to a screen point x: one passing through the first, one through the second pinhole (blue and yellow path in fig. 2.7a, respectively). Assuming that both source and screen are far from the mask $z_1, z_2 \gg s, x, D$ (binomial approximation = angles are small) we find the path difference to be

$$\eta(s,x) \approx \frac{sD}{z_1} + \frac{xD}{z_2}. \tag{2.15}$$

To convert this into a phase difference we need to multiply it with the wavevector $k = \frac{2\pi}{\lambda}$

$$\Delta\phi(s,x) \approx \frac{2\pi}{\lambda} \cdot \left(\frac{sD}{z_1} + \frac{xD}{z_2}\right). \tag{2.16}$$

If both pinholes are identical and sufficiently close to each other the two realisations of the wave $\psi(x)$ and $\psi_2(x)$ interfering at the screen will be identical except for this phase difference $\Delta\phi$

$$\psi_2(x) = \psi(x)\exp(i\Delta\phi) \tag{2.17}$$

and the measured intensity $I(s,x)$ at the screen becomes

$$I(s,x) = |\psi(x) + \psi_2(x)|^2$$
$$= |\psi(x) + \psi(x)\exp(i\Delta\phi)|^2 = 2|\psi(x)|^2 \left(1 + \cos\left(\frac{2\pi D}{\lambda}\left(\frac{s}{z_1} + \frac{x}{z_2}\right)\right)\right). \tag{2.18}$$

This describes the interference pattern originating from one point radiator s on the source, which is fully coherent to itself and thus can interfere. Since the source is assumed to be fully spatially incoherent, meaning the interference patterns from different points on the source do not interfere with each other, the contribution of all other source points is a superposition of many single point interference patterns (i.e., an integration over the source size σ_s) that are slightly offset to each other in x

$$I(x) = \int_{-\frac{\sigma_s}{2}}^{\frac{\sigma_s}{2}} I(s,x)ds = 2I_0\sigma_s + \frac{2I_0\lambda z_1}{\pi D}\sin\left(\frac{\sigma_s \pi D}{\lambda z_1}\right)\cos\left(\frac{2\sigma_s \pi D x}{\lambda z_2}\right) \tag{2.19}$$

with $I_0 = |\psi|^2$.

Looking at expression (2.19) it becomes clear that the minima between the fringes do not longer go to 0, as was the case for a single point radiator above (eq. (2.18)). This 'loss of visibility' can be used to describe and measure the quality of the interference and thus characterise the *degree of coherence* of the source. Using the *visibility* ϑ as defined by Michelson[22]

$$\vartheta = \frac{I_{max} - I_{min}}{I_{max} + I_{min}} \tag{2.20}$$

we find

$$\vartheta = \frac{|\sin(\varsigma)|}{\varsigma}. \tag{2.21}$$

This is a *sinc* function that depends on the dimensionless coefficient $\varsigma = \frac{\sigma_s \pi D}{\lambda z_1}$.

If we look at this coefficient, we can define a measure for the spatial coherence length L_T as the pinhole separation at which the visibility drops to its first minimum ($\varsigma = \pi$):

$$L_T = \frac{\lambda z_1}{\sigma_s}. \tag{2.22}$$

At this distance, the interference patterns from different source points cancel each other out completely.

Both the longitudinal and transversal coherence length set a (simplified) upper limit to the distances where interference effects between scatterers occur. If the wavelength spread or transversal distance exceeds the coherence length, the visibility of interference fringes will be low. Here, several important observations can be made:

- 'Full' longitudinal coherence requires completely monochromatic light.
- 'Full' spatial coherence can only be reached for an ideal point source, a source at infinite distance (ideal plane wave) or a coherent generation process (such as lasing, not discussed here).
- Even if two pinholes (or scatterers) are closer than the coherence length the visibility of the interference fringes will depend on their actual distance. Their scattering is partially coherent, and the visibility is a *sinc* function with several minima.
- A larger source size σ_s will reduce the transversal coherence length.
- A larger source distance z_1 will increase the transversal coherence length.

The last point is especially useful in experiments since the source size is often fixed. It allows us to preserve the visibility of the interference pattern by increasing the source distance. Note that this usually comes at the cost of flux, especially for divergent sources. This effect and its implications for phase contrast imaging are explored further in chapter 4 and **paper II** & **III**.

2.2 Imaging Metrics

Although most of us will have an intuitive understanding of what an *image* is, I want to take a moment to review the terminology. Mathematically, images are a function of 2D real space location. In principle any quantity (e.g., flow rate, altitude, pressure) can be presented as such a 2D function, creating 2D plots that are essentially images. But, in the common understanding of 'imaging' the function value is an intensity of electromagnetic radiation. What influences the recorded intensity, i.e., which physical property of the object it signifies, depends on how the image is acquired. For example, it can be the reflected intensity or the transmitted intensity, and the detected signal could be created by electrons or photons. Often additional data transformations and/or prior knowledge are necessary to translate image intensities into physical quantities. Scientific image analysis trying to extract object properties from the recorded image thus requires a thorough understanding of the underlying processes, both in the imaging system as well as in the sample (also see chapter 2.1).

There are some fundamental properties of the image – which I will call *imaging metrics* - that can be used to characterise and compare images: *contrast* and *resolution*. They contain important information about the performance of the imaging system and are linked by the optical transfer function. In this chapter I want to introduce these terms in their general meaning and how they can be measured in practice. Obviously, the experimental parameters that influence them will vary depending on the way the image is recorded. For sake of conciseness, I will restrict the discussion to contrast and resolution in X-ray full-field transmission imaging.

2.2.1 Point Spread Function and Optical Transfer Function

Imaging systems respond differently to different spatial frequencies. Low frequencies (large features) are often better transmitted by the system than high frequencies (small features). A convenient way to test the response of the system is to feed it with a single, well-known delta pulse and observe how that pulse looks when detected. Since an ideally sharp delta pulse contains all spatial frequencies (Fourier transform of a delta

pulse is a constant), this will simultaneously test the effect of the system on the whole spatial frequency range. In imaging systems this method is equivalent to measuring the *point spread function* (PSF), which means the response to or image of an ideal point source or pinhole.

The *optical transfer function* (OTF) is the Fourier transform of the PSF. It is a complex valued function over the spatial frequencies (u, v) and is often separated into its modulus and phase. The modulus is known as the *modulation transfer function* (MTF). The MTF will be equal to the OTF if the PSF is symmetric, otherwise an additional *phase transfer function* (PhTF) describes the translation of the PSF

$$OTF(u,v) = \mathcal{F}(\mathrm{PSF(x,y)}) = MTF(u,v) \cdot \exp\big(i \cdot PhTF(u,v)\big) \tag{2.23}$$

2.2.2 Contrast

Contrast is given by the relative difference of intensities in an image. It describes how easily features can be distinguished in intensity value and is sometimes also referred to as *visibility*. The image contrast is influenced by the contrast transfer of the imaging system as well as the contrast present in the sample itself.

There are different definitions of contrast, depending on the type of image. A common definition of contrast is the *Michelson contrast/visibility* that compares the image maximum and minimum intensities[22]

$$\vartheta_M = \frac{I_{max} - I_{min}}{I_{max} + I_{min}}. \tag{2.24}$$

This definition is mostly used for images which contain many features of similar size but varying intensity.

Alternatively, the *Weber contrast*[22] is defined for a small feature I_f compared to a homogeneous background I_b

$$\vartheta_W = \frac{I_f - I_b}{I_b}. \tag{2.25}$$

Like the MTF the *contrast transfer function* (CTF) gives information about the influence of the imaging system on the contrast provided by the sample. It is defined as the transfer function for an equal-width blocking-and-non-blocking stripe pattern of increasing spatial frequency and measures the visibility dependent on the stripe width. The difference to the MTF is that the MTF is defined for a periodic sine-wave pattern

instead of a stripe pattern. A common test pattern for the CTF is the Siemens star (see also resolution chapter below).

Experimentally, an upper limit to the contrast of the system is given by the dynamic range of the detector, a lower limit by the detector sensitivity. Both can be energy dependent.

Obviously, the final image contrast also depends on the physical properties of the sample that are used to generate it. As described above (chapter 2.1), absorption contrast is the most common contrast type in X-ray full-field imaging. Moreover, we will see that it is also possible to generate contrast based on the local variation of the phase shift (chapter 4). Other contrast types that can be probed in X-ray imaging are for example magnetic contrast,[23] elemental contrast (X-ray fluorescence),[24] or chemical contrast (X-ray absorption spectroscopy), which are not included in the scope of this thesis.

2.2.3 Resolution

Resolution is a measure for the minimum distance between neighbouring image features that still allows to differentiate them. The simplest features could be for example two points or lines next to each other. In any image a point or line would not appear ideally sharp, but rather slightly blurred. How strong this blurring is, is quantified by the resolution. But what limits the resolution and how can we measure it?

A fundamental limit of the resolution is given by the diffraction limit of the used radiation. The two most famous formulations of the diffraction limit are the Abbe limit and the Rayleigh limit. The Abbe limit describes the radius of the central maximum of one single Airy disk at its *full width at half maximum* (FWHM)[25]

$$l_{Abbe} = \frac{0.5\,\lambda}{\mathrm{NA}}. \tag{2.26}$$

The Rayleigh limit is defined as the distance that is reached when this central maximum overlaps with the first minimum of another Airy disk[26]

$$l_{Rayleigh} = \frac{0.61\,\lambda}{\mathrm{NA}} = 1.22\,l_{Abbe}. \tag{2.27}$$

Both limits are proportional to the quotient of the wavelength and the range of angles an optical system can accept, known as the *numerical aperture* (NA).

In most experiments, the resolution is not limited by the diffraction limit, but by the hardware. Besides imperfections in the optical components, they are also fundamentally

limited: sources are not ideally small, lenses have a finite NA, distances are limited, and the digital recording of the image introduces discrete sampling. Although these limiting factors can often be evaluated in simulations, the real resolution needs to be deducted from the image itself. Therefore, the following sections will describe some experimental methods to estimate the spatial resolution from an image.

Nyquist Frequency

Modern imaging relies on the digitalization of the image function via sensor chips and read-out electronics. This means that the physical signal is discretized or sampled, both in space and intensity. The spatial sampling is characterised by the pixel size p of the sensor chip, which is usually the same in x and y. Obviously, this introduces a fundamental limit to the achievable resolution in a single image, which is based on the sampling criterion formulated by Nyquist and Shannon.[27]

The *Nyquist frequency* is given by the pixel size p

$$f_N = \frac{1}{2p}. \tag{2.28}$$

The resolution is often given in fractions of the Nyquist frequency, and values above $2/3$ (equivalent to 3 pixels) should be evaluated with care.[28]

Resolution Test Patterns

The most obvious approach to measure resolution (and contrast) is the use of a standardised test pattern. These patterns are fabricated to high accuracy by different metrological institutes around the world. They usually consist of several line patterns (see Japanese institute of metrology (JIMA) pattern in fig. 2.8) of varying width/pitch or a star of tapered wedges, known as a Siemens star. When imaged, the visibility of the pattern will go down with higher spatial frequencies (thinner lines and wedges) and eventually the features cannot be distinguished anymore. Line patterns probe the modulation/contrast transfer at distinct spatial frequencies, while in a Siemens star the spatial frequency continuously decreases with larger radius. Accordingly, a common unit for expressing resolution in terms of spatial frequency is line pairs/mm (lp/mm). The main challenge for test patterns is the fabrication: making precise, very small and high aspect ratio (high contrast) depositions on a mostly transparent substrate. Moreover, for high X-ray energies reaching the necessary absorption contrast becomes increasingly difficult.

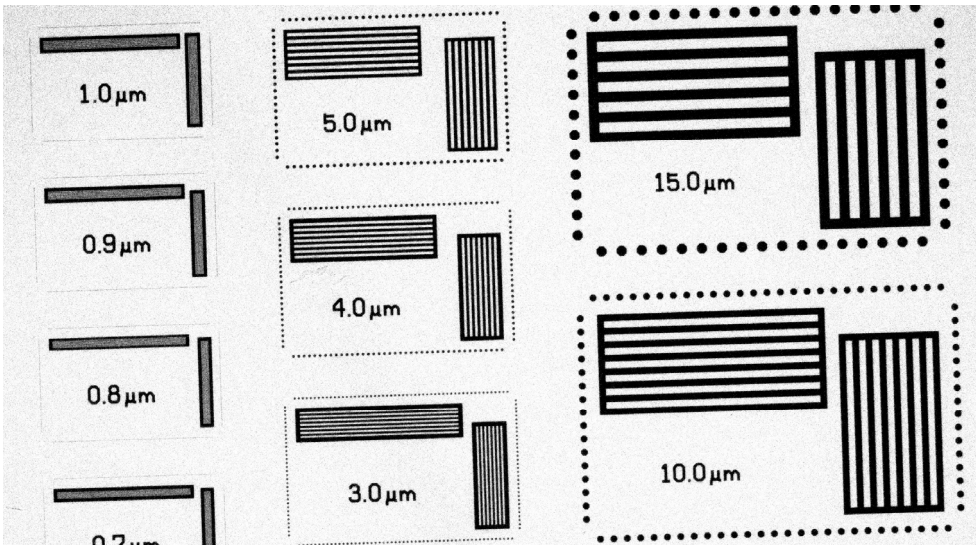

Figure 2.8: Image of a JIMA test pattern taken with an X-ray microscope. The visibility of thinner bars (high spatial frequency) is reduced compared to wide bars (lower spatial frequency). Bars thinner than the resolution of the system cannot be distinguished.

Slanted edge Method

It is common to measure the resolution of the system via measuring the MTF. As we have seen the MTF is the modulus of the Fourier transform of the PSF (see eq. (2.23)). Obviously no 'ideal point' (i.e., light source) can be created in practice, but this is also not necessary. If the initial signal contains higher frequencies than the Nyquist frequency it will cover the entire relevant frequency range and help to estimate the resolution of the system.

In practice it is easier to measure the *line spread function* (LSF), which is the one-directional equivalent to the PSF, by imaging a thin wire or slit. The PSF can then be assembled from different orientations of the LSF. Even more common than measuring the LSF directly is to use an edge to first extract the *edge spread function* (ESF). Edges are comparably easy to fabricate and provide a stronger signal. The LSF can then be retrieved as the first derivative of the ESF

$$LSF(x) = \frac{d}{dx} ESF(x). \tag{2.29}$$

For one spatial direction, the MTF can thus be measured via the *slanted edge method*.[29] Here, an image of a sharp, slightly slanted edge is taken with the imaging system, thus measuring the ESF (see fig. 2.9). For the x-direction (MTF_x) the edge is slightly tilted towards the pixel columns y to provide sufficient over-sampling of the edge. A

composite lineout comprised of datapoints from several pixel rows with sub-pixel displacement is assembled before the LSF is calculated. For more details see Buhr et al.[29] The MTF for the given edge orientation (here denoted as MTF_x) is then derived as the modulus of the 1D Fourier transform of the LSF (see fig. 2.9):

$$MTF_x(u) = \left|\mathcal{F}\big(LSF(x)\big)\right| = \left|\mathcal{F}\left(\frac{d}{dx}ESF(x)\right)\right|. \tag{2.30}$$

In practice it is often advisable to not perform the gradient and Fourier transform numerically on the signal, since high frequency noise can lead to artifacts. Instead, one can perform a fit on the extracted ESF and work analytically with the fit parameters to estimate the resolution. This obviously idealizes the signal because all noise contributions are ignored after the fitting step and the used fit-function is pre-defined. To avoid missing noise textures which could provide important information about the system, one should also examine the noise power spectrum.

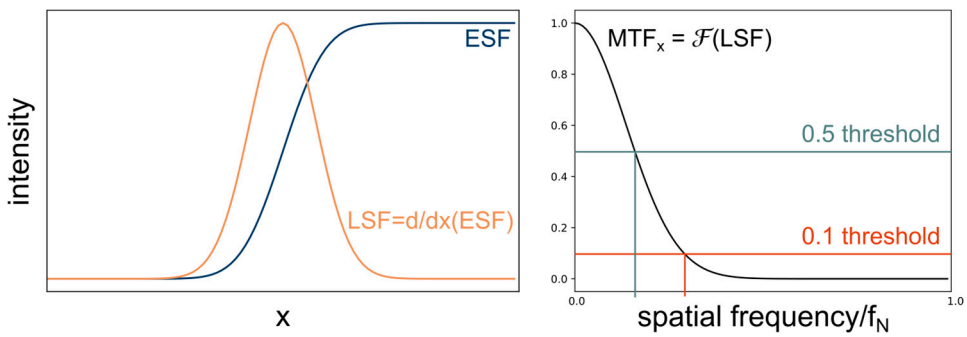

Figure 2.9: Illustration of 1D MTF calculation from an edge. The resolution of the imaging system can be measured by imaging an edge. A lineout over the edge gives the ESF, from which the LSF is calculated as the gradient. The MTF is then extracted as the Fourier transform of the LSF. The spatial frequency at which the MTF falls under a given threshold estimates the spatial resolution. Note that these are simulations based on the edge model of a Gaussian blurred error function.

An ideal system would transfer all spatial frequencies up to the Nyquist frequency equally. However, in practice the imaging system works as a low-pass filter. The highest frequency that is still transmitted sufficiently can be used to estimate the resolution. What is 'sufficient' is usually defined by a threshold. Several different threshold definitions are popular in literature; therefore, it is sometimes difficult to compare resolution values. The most common thresholds for the normalized MTF are 0.1, 0.143 and 0.5.

Fourier Ring/Shell Correlation

An alternative method to estimate the resolution is the *Fourier ring correlation* (FRC) which was originally developed for structural biology.[30, 31] One of its advantages is that it has an equivalent for 3D data (*Fourier shell correlation*, FSC). For simplicity I will describe the 2D case, which can be easily generalized into 3D.

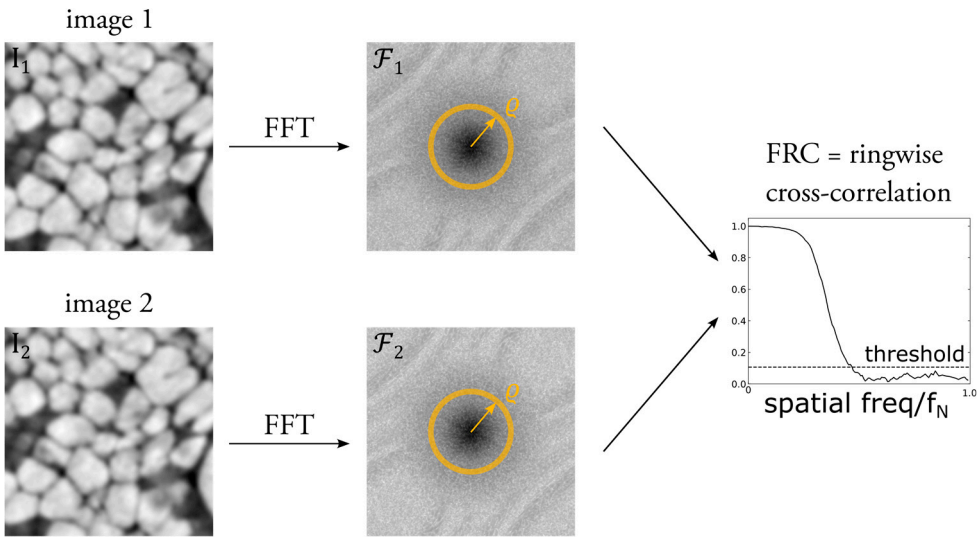

Figure 2.10: Illustration of the Fourier ring correlation. The Fourier ring correlation is a cross-correlation carried out in Fourier space. Two independent images of the same object are Fourier transformed and the complex-conjugated product is calculated ring-wise and normalized with the product of their absolute values, see eq. (2.31).

Conceptually it is a *similarity measure* to compare two equivalent but independent images of the same sample, acquired with the same imaging system. This stands in contrast to the MTF, which measures the frequency response directly. While the MTF only uses one measurement and thus represents a snapshot of the performance of the imaging system and its noise, the FRC contains information about the reproducibility of the measurement. As such, the FRC is used to find a value for the highest spatial frequency which is consistently carrying the same information in two independent images.[32] Mathematically it is the normalized Fourier transformation of the cross-correlation between the images, evaluated over frequency rings ϱ in Fourier space

$$FRC(\varrho) = \frac{\sum_{\varrho_i \in \varrho} \mathcal{F}_1(\varrho_i)\mathcal{F}_2(\varrho_i)^*}{\sqrt{\sum_{\varrho_i \in \varrho} |\mathcal{F}_1(\varrho_i)|^2 \sum_{\varrho_i \in \varrho} |\mathcal{F}_2(\varrho_i)|^2}}. \tag{2.31}$$

Here $\mathcal{F}_{1,2}(\varrho_i) = \mathcal{F}(I_{1,2})(\varrho_i)$ denotes the Fourier transforms of the images I_1 and I_2, as a function of radius in spatial frequencies $\varrho = \sqrt{u^2 + v^2}$. The summation is carried out over all pixels ϱ_i in the corresponding ring ϱ in Fourier space. Note that the ring-wise integration necessarily provides only an average resolution of all directions.

The resulting curve has usually a similar shape to the MTF and analogously a threshold criterium can be defined to find a value for the estimated resolution. Besides constant thresholds several frequency dependent thresholds like the half-bit criterium were proposed. These consider the average information content in each voxel, based on a target value of the *signal-to-noise ratio* (SNR) in the final reconstruction and accounting for the number of voxels in each frequency ring/shell.[28]

To avoid artefacts from the image boundaries in the numerical *fast Fourier transform* (FFT) or correlation between reconstruction artefacts (see chapter 2.3.2), it is common to use an apodization filter, such as a Kaiser window, on the data to smoothly bring the intensity to zero at the boundaries.

2.3 Tomography: Accessing 3D Information

Although 2D X-ray imaging can already reveal much about the inner structure of a sample, the 2D image of any 3D object still contains an inherent ambiguity – the contrast generated by a thickness or material variation cannot be distinguished in a projection and it is impossible to know which feature is in front of the other. This often makes the image analysis and interpretation difficult or even impossible. To overcome this, several different projections of the sample are necessary.

The combination of many 2D projections to a 3D volume is called *tomography*, which comes from the Greek words *tomos*, 'slice, section,' and *graphō*, 'to write,' referring to the reconstruction of slices through a 3D volume. Various analogue tomographic techniques which used projections in different geometries were developed as early as the 1920s,[33] although the technological means to reconstruct a full volume were still missing. A paradigm-change in all fields of imaging, but especially in tomographic imaging, came with the availability of computers to quickly perform complicated mathematical operations. Since its first proposal by Hounsfield and Cormack in 1972, *computed tomography* (CT) has revolutionized non-destructive imaging.[1] In 1979 the importance of this invention was acknowledged with the Nobel prize in medicine (see fig. 1.2).

This chapter introduces the mathematical concepts of CT imaging, followed by a more practical overview of the most common artefacts that can be encountered in a CT reconstruction.

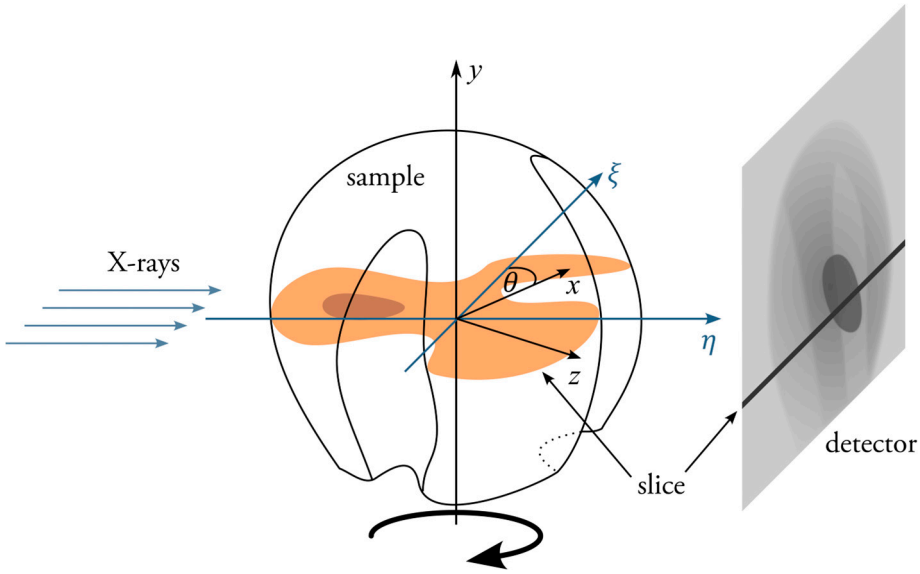

Figure 2.11: Concept and coordinate system of an X-ray tomography measurement. The (parallel) X-ray beam is transmitted through the sample at a specific rotation around the y-axis and a projection image is recorded with the detector. The projection of a horizontal slice through the sample is equivalent to one pixel row in the detector image.

2.3.1 Radon Transform and Filtered Back Projection

In a tomography experiment we want to retrieve the 3D distribution of the absorption coefficient $\mu(x, y, z)$ from a series of 2D projections through the sample. Commonly these projections are taken when the sample is rotated around an axis perpendicular to the X-ray beam, which is in the following denoted as y (see fig. 2.11).

We can imagine the 3D volume of the sample as a stack of 2D slices along the y-axis. For sake of simplicity, the following derivations are for only one of these slices (see fig. 2.11) which is a 2D distribution of the absorption coefficient $\mu(x, z)$. For parallel beam illumination, the slices are independent from each other, and the formalism can easily be extended into 3D. If a row of parallel rays passes through a slice and the projection approximation (see chapter 2.1.2) holds, the ray path within the sample will not change and the detected intensity behind the sample will depend only on the *line integral or projection* of the refractive index along the ray. Each slice is projected onto one pixel row of the detector. This projection is called the *Radon transform*. Note that in the following I will use the terms Radon transform and projection interchangeably.

Now, the challenge of tomography is to inverse the projection step and reconstruct the local absorption coefficient. One way to do so is using the *inverse Radon transform.* Obviously, the projection collapsed one spatial direction, so it is necessary to combine many projections at different rotations to retrieve the 3D information. Mathematically,

it is irrelevant if the beam or the sample rotates, as long as they rotate relative to each other. In practice the choice depends on practical considerations: in medical CTs usually the patient is at rest, while in microscopy and/or synchrotron radiation applications it is easier to rotate the sample. For this derivation, I will work with a resting sample and a rotating beam.

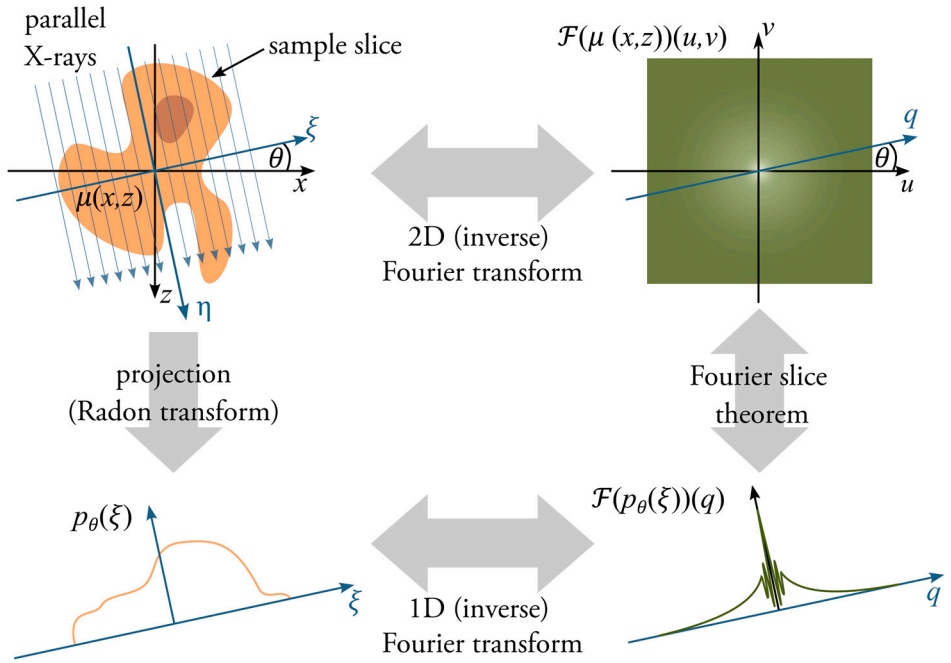

Figure 2.12: Illustration of the Fourier slice theorem and Radon transform. Left side from top to bottom: When an image at angle θ is taken with parallel X-rays, a 1D signal proportional to the projection of the absorption coefficient $\mu(x,z)$ is measured in one detector pixel row. Right side: To retrieve the full 2D information of $\mu(x,z)$ the Fourier slice theorem can be used, which states that the 1D Fourier transform of this projection is equivalent to the slice along θ through the 2D Fourier transform of $\mu(x,z)$. By assembling the Fourier transforms of many projections at different angles and performing an inverse 2D Fourier transform the real space distribution of the absorption coefficient can be reconstructed.

The Radon Transform (Projection)

To describe the projection process for an arbitrary orientation of sample and beam, we define two coordinate systems: (ξ, η) that rotates with the beam around the sample, (blue in fig. 2.12) and (x, z) that is fixed to the resting sample (black in fig. 2.12). This means that in all rotations the beam remains parallel to η. The two coordinate systems are linked to each other by a rotation operator with the rotation angle θ, so that

$$\xi = x\cos(\theta) + z\sin(\theta) \tag{2.32}$$

$$\eta = -x\sin(\theta) + z\cos(\theta) \tag{2.33}$$

The beam is a set of rays parallel to η but offset to each other in ξ (see fig. 2.12). This means that the path of a single ray at rotation angle θ can be described by $\xi = const$, where the value of ξ gives the offset of the beam from the rotation axis y, as well as the horizontal pixel position on the detector.

The projection $p_\theta(\xi)$ or *Radon transform* $\mathcal{R}$ of the absorption coefficient is thus the integration of $\mu(x,z)$ along $\xi = const$.

$$\begin{aligned}\mathcal{R}\big(\mu(x,z)\big)(\xi,\theta) &= p_\theta(\xi) \\ &= \int_{-\infty}^{\infty}\int_{-\infty}^{\infty} \mu(x,z)\delta(x\cos(\theta) + z\sin(\theta) - \xi)dx\,dz\,.\end{aligned} \tag{2.34}$$

Here, the Kronecker δ-function restricts the integration to the coordinates that coincide with the ray path ξ. This describes a parallel beam X-ray transmission image as a projection along the ray path.

The Inverse Radon Transform (Simple Back-Projection)

To go from the above description of the measurement back to the sample volume the problem needs to be inversed. One way to do this is using the *Fourier slice theorem*, which connects the 1D Fourier transform of the projection $p_\theta(\xi)$ with the 2D Fourier transform of the sample. It can be derived from the 1D Fourier transform of the projection by executing the integration over the Kronecker δ-function and identifying the reciprocal slice coordinates u and v:

$$\begin{aligned}\mathcal{F}\big(p_\theta(\xi)\big)(q) &= \iiint_{-\infty}^{\infty} \mu(x,\mathrm{z})\delta(x\cos(\theta) + z\sin(\theta) - \xi)\, e^{-2\pi i q\xi} dx\,dz\,d\xi \\ &= \iint_{-\infty}^{\infty} \mu(x,z)\, e^{-2\pi i(xq\cos\theta + zq\sin\theta)}\, dx\,dz \\ &= \iint_{-\infty}^{\infty} \mu(x,z)\, e^{-2\pi i(xu+zv)}\, dx\,dz\,.\end{aligned} \tag{2.35}$$

In words, this means that the 1D Fourier transform of the projection image $p_\theta(\xi)$ at angle θ is equal to a slice along angle θ through the 2D Fourier transform of the sample (slice coordinates $u = q\cos\theta$ and $v = q\sin\theta$), see fig. 2.12. Accordingly, the entire sample can be reconstructed by assembling the 1D Fourier transforms of many projections at their respective θ and applying an inverse 2D Fourier transform. This

gives us a recipe for the *inverse Radon transform* $\mathcal{R}^{-1}$, which is also referred to as *simple back-projection*.

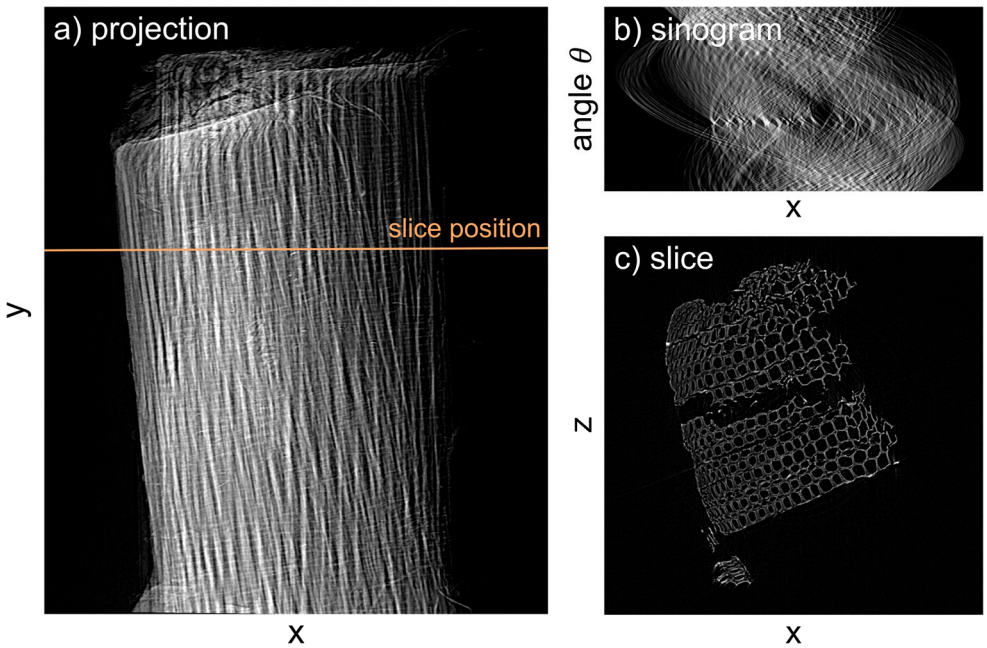

Figure 2.13: Example of tomographic data of a wood splinter acquired with our lab tomography setup (see chapter 3). a) A single projection image. Note that the projected features obscure each other, and the fibres cannot be distinguished. b) Sinogram of the pixel row indicated in a). The same pixel row is plotted over different rotation angles θ. The pattern is a superposition of sinusoidals. c) Tomographic reconstruction of the slice indicated in a), using 1000 projections and FBP. The individual fibres are now easily distinguishable and a crack in the centre of the splinter is visible.

Filtered Back-Projection

Although the simple back-projection above will result in a reconstruction of the volume, it comes with artefacts due to the change of coordinate systems. Assembling the 1D Fourier transforms along their rotation angle θ in Fourier space provides a polar coordinate system (q, θ) and the inverse Fourier transform to retrieve the real space slice $\mu(x, y)$ accordingly needs to be expressed in polar coordinates. This change from a cartesian coordinate system to a polar coordinate system introduces a ramp filter (high-pass filter) in the inverse FFT, hence it is termed *filtered back-projection* (FBP).[34] Practically, most implementations of the FFT use cartesian coordinates, therefore this comes with a re-gridding and interpolation step and entails that the sampling is not uniform over the whole Fourier space but decreases towards higher frequencies. Although mathematically correct for noiseless data, the high-pass filtering with a simple ramp filter has the unwanted side effect to amplify high-frequency noise in real data.

Therefore, many different filter shapes that suppress the highest frequencies were suggested. Some common ones are the cosine, the Shepp-Logan, the Hann and the Hamming filter. If no filter is applied (simple back-projection), an overall low frequency background will be present in the reconstruction, visible as a blurring or halo around the features.

The FBP is just one of many reconstruction algorithms that have been developed over the years. Due to its relative simplicity and speed, it is widely used. Alternatively, iterative methods have been developed, mostly based on the *algebraic reconstruction technique* (ART).[35] ART iteratively solves a set of linear equations describing the image formation. Its strength is that it can include prior knowledge, such as a sample support, into the reconstruction. Several other algebraic techniques such as SIRT,[36] MART[35] and SMART[37] have been proposed that use different orders and types of the iterative update. A further discussion of these algorithms is outside of the scope of this thesis, since I have not used them in the presented research.

Crowther Criterium

The *Crowther criterium* states how many projections m are needed to get a reconstruction with a specific spatial resolution l based on the sample diameter D:

$$m = {}^{\pi D}/_{l}. \tag{2.36}$$

Since the resolution should ideally be a few pixels, this means one needs to acquire about as many projections as the sample diameter measures in number of pixels.[38] Note that the resolution will usually not be isotropic in the volume, since the sampling within a slice is restricted by the mentioned change of coordinate systems, while the sampling along the rotation axis is given by the height of the detector pixels.

For parallel beam tomography the projections should cover at least 180°, while in cone beam scenarios an additional angular range proportional to the cone angle needs to be covered to avoid artefacts.[39]

Sinogram

A common way to plot tomographic data is the *sinogram.* It means plotting a single pixel row over the rotation angle θ. If no misalignment or drift occurred during the measurement the features should follow sinusoidal curves around the centre of rotation (see fig. 2.13b). The sinogram can also be used for post-processing like re-alignment, based on fitting of the curves,[40] or removal of artefacts.[41]

2.3.2 Reconstruction Artefacts

Naturally, a tomographic experiment is rarely as ideal as the mathematical model assumes. The deviations from the model will lead to various kinds of artefacts in the reconstruction step. The artefacts can be caused by the imaging system, due to misalignments, as well as by the sample, due to a too high or changing absorption. Understanding what causes an observed artefact is therefore important when improving the system. Most of them can be corrected or filtered (to a certain degree) using various post-processing strategies, but it is always favourable to avoid their causes in the measurement.

Ring Artefacts

Ring artefacts can occur due to spatially fixed imperfections in the imaging system that do not rotate with the sample. These could be dead/broken detector pixels or any background that was insufficiently corrected by the flat field correction, such as structures in the scintillator. Since these artefacts have a very characteristic structure as either (half) rings in the reconstructed slices or stripes in the sinogram, it is relatively easy to correct them in the data processing step.[41, 42]

To avoid these artefacts, it is important to have a good flat field correction. For that, no movements, or changes within the imaging system, such as local scintillator degradation, saturated pixels, changes of illumination, or drift of optical elements, should occur.

Centre-of-rotation Offset or Tilt

In the derivation of the inverse Radon transform we have implicitly assumed that the centre-of-rotation is in the centre of the image/detector. If this is not the case, this needs to be corrected by either cropping/shifting the images or adding an offset in the reconstruction step. A misaligned centre-of-rotation will cause half-moon shaped smearing of the features in the reconstructed slice.

Often the rotation axis has a tilt perpendicular to the optical axis (roll angle, along ξ in fig. 2.11), which means that the slices perpendicular to the rotation axis are not parallel to the pixel rows and the centre-of-rotation is slightly offset in each pixel row, which creates similar artefacts. To compensate this the images can be computationally rotated before the reconstruction, to align the rotation axis with the centreline of the detector.

Similarly, the rotation axis can be tilted along the optical axis (pitch angle). Although this can be included into some reconstruction algorithms that take the geometry into account, it is best to try avoiding it during the measurement, for example by using a goniometer or stages (see chapter 3.2.2).

Beam Hardening and Cupping Artefacts

When a polychromatic source is used, each spectral component will have a slightly different absorption in the sample. The spectrum after passing through the sample will therefore be different from the original source spectrum. The absorption of the low energies will be stronger than of the higher energies; the radiation becomes 'harder,' essentially high-pass filtered. Therefore, the mean energy of the spectrum after passing the sample will be higher than in the flat field image without a sample. Since absorption decreases with increasing energy this makes the sample appear to have a lower absorption than it has. This effect is strongest behind the thickest part of the sample. Usually the centre-of-rotation is chosen close to the radial centre-of-mass of the sample. Accordingly, the centre of a reconstructed slice has a reduced absorption compared to reality, which is known as a *cupping artefact* and looks like a smooth increase of absorption towards the periphery of the slice.

Additionally, the flat field correction might 'fail,' meaning that structures of the detector are not fully removed from the image, since the detectors are often spectrally sensitive themselves, especially if a scintillator is used (also see chapter 5).

Metal or Streak Artefacts

If the sample has features that completely absorb the incoming radiation (such as metal pieces in tissue, thus the name *metal artefacts*), no information is recorded along rays passing through these features. In every projection there is therefore a lack of information about the sample along these lines, making the reconstruction underdetermined. In the reconstruction this looks like streaks radially going through high-density features, often connecting two features. Even though they are easy to identify visually, streaks can become problematic in automated segmentation and obscure important image information.

To avoid streak artefacts, it is possible to pre-harden the beam with filters or to use higher acceleration voltages in the X-ray tube to generate a harder spectrum from the start. Additionally, iterative algorithms can be used to reduce the artefacts in post-processing.[43]

Cone Beam Artefacts

The original Radon transform and FBP assume a parallel beam illumination. This guarantees that each slice in y is independent from the neighbouring slice and that the rays within the slice are parallel. This is not the case when uncollimated lab sources are used. In a *fan beam* scenario, the beam has a horizontal divergence while in a *cone beam* scenario the beam is divergent in all directions. This means that in different projections the same detector pixel row will contain information about different parts of the

sample. If the FBP is used on such a dataset, features will show half-moon shaped artefacts around the edges.

Although every non-collimated lab source will produce a cone or fan beam, this effect becomes mostly problematic for large magnifications, where the sample-detector distance is large. In low magnification geometries the beam can often still be assumed as parallel and FBP can be used without significant artefacts. If cone beam artefacts occur, different tomography reconstruction algorithms (which include the geometry) need to be applied.[39]

Afterglow Artefacts

It is common that scintillators show a certain degree of *afterglow* – weak remains of previous images burned into the scintillator that only slowly fade due to long lived excited states in the scintillator material. This can pose a problem if the sample has a high contrast (see also streak artefacts) and/or if the scan is performed fast because it leads to (partial) ring artefacts (see above).

Although correction in post-processing is sometimes possible,[44] it is accepted that scintillators that show strong afterglow are not suited for serial image acquisitions in tomography (also see chapter 5).

3 X-ray μCT with a Laboratory Setup

A major part of my PhD project was to establish the first laboratory X-ray μCT setup at the Division of Synchrotron Radiation Research (SLJUS) at Lund University. The setup is intended as a complimentary tool to synchrotron radiation studies, for method development, scintillator testing and teaching.

Since the technical aspects and characterization of the setup are reported in detail in **paper I**, the first part of this chapter will focus on setting the context, briefly introducing hardware and geometry, and providing a short review of other state-of-the-art setups. In the second part I will discuss the motivation of the specific design choices and give some notes on alignment procedures. If not otherwise indicated, all X-ray images and research results in this thesis have been acquired with this setup.

3.1 Hardware and Geometry

Any X-ray imaging setup in a laboratory contains at least an X-ray source and a detector. Here, a very brief introduction to both technologies is given. Moreover, the two most common setup geometries are presented, and some state-of-the-art setups are reviewed.

3.1.1 Laboratory X-ray Sources

The fundamental idea behind common laboratory X-ray sources has changed little since Röntgen's times. An evacuated *X-ray tube* contains a filament that is used to create a cloud of free electrons. These are then accelerated with high voltages towards an anode where they, upon impact, drastically decelerate and emit most of their energy in form of *bremsstrahlung* (deceleration radiation). Due to their high kinetic energies, this broad-band radiation is mainly in the X-ray regime. Additionally, they can ionize the atoms in the anode by transferring their energy to an inner shell electron. Like X-ray induced fluorescence this vacancy will be filled by an electron from a higher shell. The freed energy can then be emitted as a photon (see chapter 2.1). Since the energy of the transition is element specific, the corresponding spectral features are known as *characteristic lines*.

An example of a Cu anode spectrum is shown in fig. 3.1, indicating the broad, weak bremsstrahlung background and the intense characteristic lines defined by the anode material.

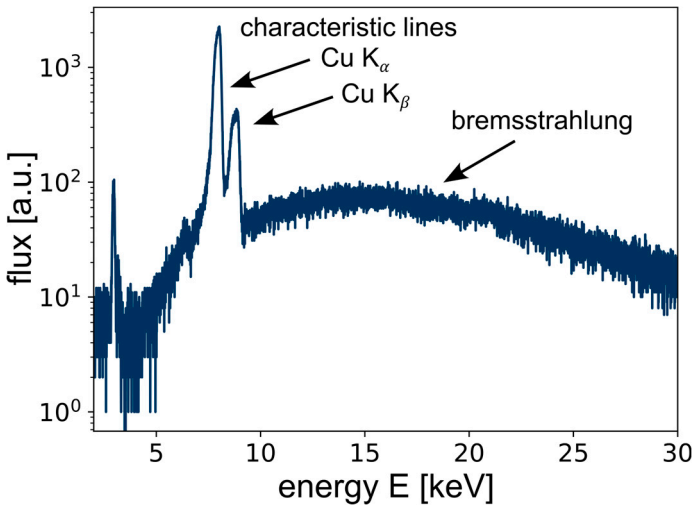

Figure 3.1: Example of the X-ray spectrum emitted by a Cu anode X-ray tube. The spectrum shows a broad bremsstrahlung background due to the deceleration of the electrons and some intense narrow peaks, the characteristic lines of the anode material. The position of the characteristic lines solely depends on the energy levels of the anode material while the background can change with tube voltage. Spectrum provided by Rigaku.

To have a high spatial coherence (see chapter 2.1.3), the electron spot on the anode needs to be as small as possible, therefore the electron beam is focussed with magnetic lenses. Although it is technically possible to focus electrons to a very tight spots in the nanometre range, like in scanning electron microscopes, this is rarely done in X-ray tubes. Since the electrons also transfer parts of their energy in form of heat to the anode, it can melt under too high power densities. A trade-off between spot size and beam current is therefore necessary. Sources with small spots accordingly work at low powers and the X-ray flux is low.

However, there are technologies that partly overcome these limitations: *rotating anode sources* continuously move the target under the electron beam. The integrated heat load is then spread over a larger area. Similarly, *liquid metal jet sources* use a constant flow of an already liquid metal alloy. This technology is fundamentally limited by the evaporation temperature, which pushes the limiting power density several orders of magnitude.[45] Finally, *transmission target sources* use only thin layers of the anode material on crystalline substrates (e.g., diamond) that have a better heat transport. Electron spot sizes in the range of a few hundred nanometres can thus be reached, at powers similar to traditional micro-focus sources. Nevertheless, since the metal layer

itself is very thin the absolute X-ray flux is still lower than in traditional reflection target sources.

3.1.2 X-ray Detectors

Over the last century imaging screens and photographic film have been almost completely replaced by digital sensors. Today, two main types of X-ray detectors can be distinguished: direct detectors and indirect detectors.

In *direct detectors* the impinging X-rays generate a charge cloud in a bulk semiconductor layer which is then directly read out via a thin film transistor or complementary metal-oxide-semiconductor (CMOS) layer and converted into an electrical signal (see fig. 3.2a). The most sensitive detectors to date are *photon counting detectors* with an essentially noise free read-out. They also offer a variable build-in energy thresholding, enabling energy filtering and multi-energy imaging without the need for filters or a second source.[46] Due to the necessary on-chip electronics the physical pixel size of photon counting detectors is relatively large (several micrometres).

In contrast, *indirect or scintillator detectors* use a scintillator screen that emits visible light when excited with X-rays. This is then detected with a common visible light photodetector, e.g., a charge-coupled device (CCD) or CMOS (see fig. 3.2b). Having sensor and detector decoupled comes with the possibility to use visible light optics for additional magnification. Effective pixel sizes below 1 µm can thus be reached, even with moderate physical pixel sizes of the photodetector. In contrast to direct detectors no energy thresholding is possible. For further information on scintillators, please see chapter 5.

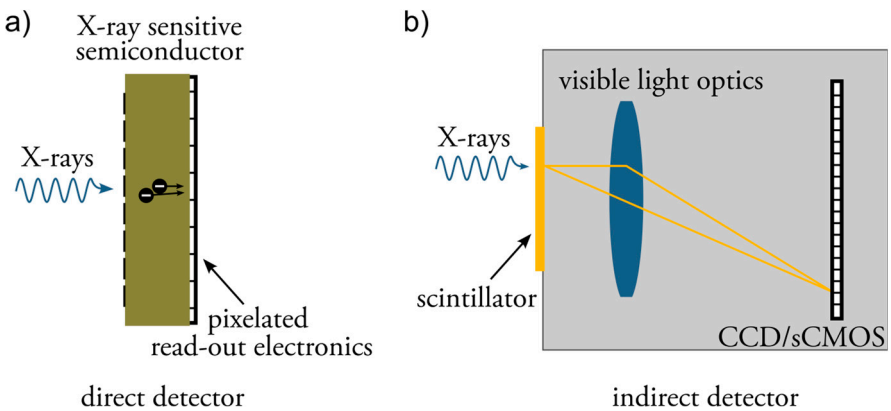

Figure 3.2: Types of X-ray detectors. a) In a direct detector the X-ray photon is absorbed in a semiconductor layer and the generated charges are directly collected to generate an electric signal. b) In an indirect detector the X-rays are absorbed in a scintillation screen which then emits visible light. The visible light signal can be detected with a common pixelated light sensor. Additional magnification with visible light optics is possible.

3.1.3 Setup Geometries

There are two main strategies to achieve high resolutions in full-field laboratory X-ray projection imaging without employing additional optics: a *high-magnification geometry* using a small source or a *low-magnification geometry* using a high-resolution detector (see fig. 3.3).

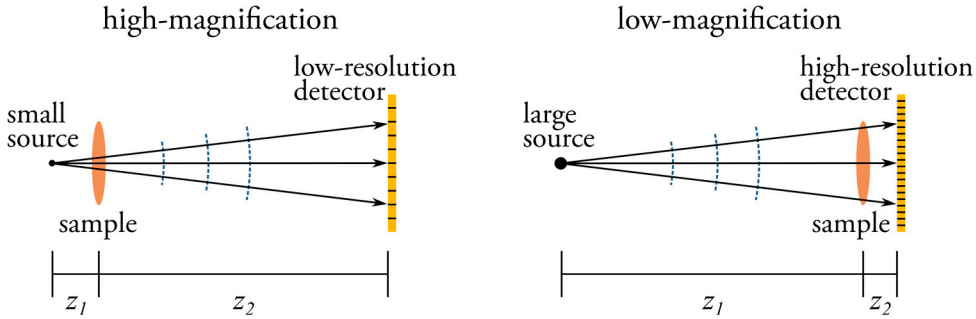

Figure 3.3: Illustration of the two main cone beam full-field imaging geometries. Left: In the high-magnification geometry the small source spot allows the sample to be close to the source and the detector can have a lower resolution, since the sample structures are highly magnified. Right: In the low-magnification geometry the resolution is provided by the detector. A relatively large source spot can be used, but the sample needs to be placed close to the detector to avoid source blurring.

The geometrical magnification is given by the source-sample distance z_1 and sample-detector distance z_2 in the setup (see fig. 3.3):

$$M = \frac{z_1 + z_2}{z_1}\,, \tag{3.1}$$

and weights the contribution of the source spot size and detector PSF to the overall spatial resolution of the setup (also see chapter 2.2.3 and 4.3.2).

Accordingly, in the high-magnification geometry the spatial resolution is limited by the source spot size, while the requirements on the detector resolution and/or pixel size are more relaxed. The drawback of this approach is the need for very small electron spots in the source, which limits the source power (see chapter 3.1.1). To reach high magnifications z_1 needs to be very small compared to z_2. This means either positioning the sample very close (a few tens of micrometres to millimetres) to the source, which can be challenging depending on the source housing, or providing large distances behind the sample (up to several hundred of centimetres). Moreover, in divergent beam setups large total distances come with the loss of many photons, since the intensity scales inversely with the square of the distance. Another consideration is the need for proper cone-beam treatment in the tomography reconstruction (see chapter 2.3).

The low-magnification approach uses the inverse geometry: large source-sample distances z_1 and small sample-detector distance z_2. The resolution is here limited by the detector resolution, and it is possible to use conventional micro-focus sources with up to a few tens of micrometre spot sizes. The highest resolution detectors available today are indirect detectors using a scintillator and optical magnification to reach effective pixel sizes in the sub-micron range. Since the magnification is close to 1, the tomographic projections of thin samples can be approximately treated as parallel beam projections. With uncollimated sources the drawback of this approach is that most photons from the source never reach the sample. Although this also means a low dose, it sets a practical limit to reasonable overall distances.

3.1.4 State-of-the-art X-ray µCT Laboratory Setups

With the technological advancement in X-ray sources and detectors many different setups have been reported over the last years. Since publications focussing on technical aspects and instrumentation are often not considered very prestigious, I expect that many more setups are in use, but not reported in a dedicated publication. The following overview is thus only a small selection, with no claim to completeness.

Recently, the most exciting development in full-field X-ray laboratory microscopy is probably the achievement of sub-micron resolution by using a nano-focus transmission source.[12] The source spot in transmission sources like the NanoTube (Excillum) or the FXE series (Comet) reaches down to a few hundred nanometres. In a high-magnification geometry this allows to reach true sub-micron resolution without additional optics. Fella et al.[12] paired this source with a photon counting detector (pixels size 75 µm) and reached 150 nm resolution already in 2018.

Some commercial systems, such as the Xradia series (Zeiss), provide a combination of several detectors for high- and low-resolution imaging, as well as multiple energy filters. Due to the convenience of such an integrated solution, they are popular in 'application labs' for example at biomedical research facilities that have a high number of similar tomography applications. The drawback is that the user has only limited possibilities to change or improve the system. Method development is thus difficult.

Usually, laboratory sources are polychromatic and uncollimated, which stands in contrast to setups at synchrotron radiation sources. In 2019 Brombal et al.[47] presented a setup based on a rotating anode source paired with a monochromator and pinhole collimator in a low-magnification geometry with a scintillator detector, which is closer to the situation at a synchrotron radiation source. Due to the monochromaticity it allows for quantitative phase contrast imaging (see chapter 4), which is usually difficult in laboratory setups.

Eckermann et al.[48] compared two setups that use different approaches to achieve the same performance: one setup based on a nano-focus transmission tube with a photon counting detector and the other setup using a micro-focus rotating anode with a high-resolution scintillator detector. Both setups achieved a comparable spatial resolution of ~1.8 µm in the presented application, but the SNR and exposure times were shorter for the transmission target setup, although not drastically. This shows that a clear verdict of one approach being superior to the other is often difficult and can depend on other factors. Some of these design considerations are presented in the next chapter.

Besides pushing for higher resolutions or faster scans the availability of many, complementary setups is good news for the field. With every new setup, the accessibility of tomographic X-ray imaging is increased, opening new possibilities for many disciplines.

3.2 The Lab Setup at SLJUS

This chapter documents the design process that led to the setup in our lab which is described in **paper I**. Building this setup, starting with an empty room, and going all the way to the implementation of control and analysis software, has been the foundation of the research results presented in the remainder of this thesis. Here, I present additional insights into the thoughts behind the current design and how it performs in terms of resolution. Finally, I provide some more practical information about the use of the setup. Additional technical details about the used hardware and performance can be found in **paper I**.

3.2.1 Instrumental Design Choices and Performance

Our setup was designed for X-ray microscopy and µCT with the option of propagation-based phase contrast imaging (PB-PCI) and scintillator testing, which will be discussed in more detail in chapter 4 and 5, respectively. Here I only briefly indicate when choices have been dictated by these modalities and refer the reader to the respective chapters for understanding the underlying theory. In summary, the initial considerations were:

a) resolution in the 1-5 µm range
b) *field-of-view* (FOV) in millimetre range
c) as few optical elements as possible (for maintaining the flux)
d) high spatial coherence in the micrometre range at the sample position (for phase contrast)

e) flexibility to change the propagation distance in the range of 5 - 100 cm (for phase contrast)
f) low X-ray energies, around 10 keV (for phase contrast)
g) option for scintillator testing
h) stability over several hours (thermal, mechanical)
i) compact setup, fitting on optical table of max. 1 x 2 m (room size constraint)

Moreover, in our lab a major design goal was the idea to be able to use the setup as a test bench for scintillator testing and development. A detailed description of scintillators and how to test them is given in chapter 5. Scintillator detectors can provide a smaller effective pixel size (see chapter 3.1.2) and are commonly used in low-magnification setups. Therefore, the first design choice was to use the low-magnification geometry (see fig. 3.3) for a realistic testing scenario.

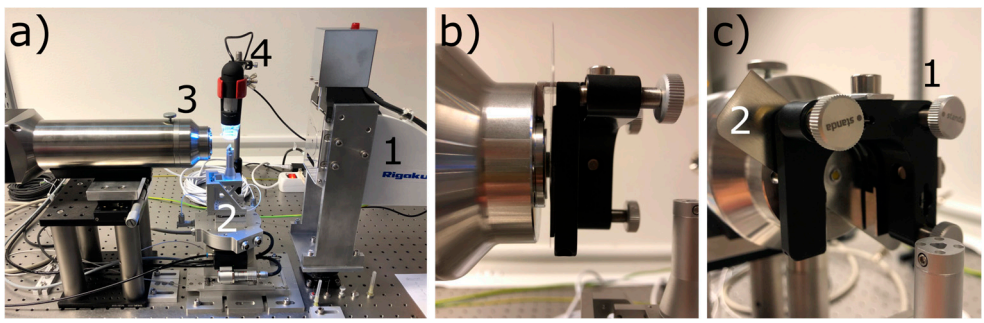

Figure 3.4: Photo of the lab setup. a) Labelled components: 1 - Cu micro-focus source, 2 – five-axis tomography stage, 3 – Scintillator detector with commercial objective, 4 – alignment microscope, b) detail of the scintillator mount (black) attached to the objective without build-in scintillator (side view) c) scintillator mount: 1 – kinematic mount with micrometre screws, 2 – magnetically attachable holder with pinhole for the scintillator. Reproduced with permission from **paper I** © IOS Press.[49]

Since in this configuration the requirements on the source spot were low, we decided on a standard micro-focus Cu source from Rigaku. The Cu anode has its main characteristic lines at 8.04 keV. We choose this low X-ray energy because the phase contrast term (and the transversal coherence length) scales inversely with the energy (see chapter 4). The source spot size is about 28 µm (FWHM) = 12 µm (σ_s), at 45 kV and 1 mA. The transversal coherence length at around 10 cm from the source is therefore about 1.5 µm, which matches the expected resolution and feature size in which we are interested. Typical exposure times per image for a tomogram are in the 10-60 s range, depending on the contrast provided by the sample and the chosen source-detector distance. This means that a full scan can take several hours, which is unproblematic for many dry samples, as e.g., seeds or fibres (see fig. 3.6).

We were aiming for a compact setup, with a small footprint of the tomography stage, in the range of a couple of centimetres side lengths. We chose a 5-axis system instead of a hexapod, consisting of two longer linear axes that carry the air-bearing rotation stage and three linear axes on top of the rotation stage. The upper axes are used for aligning the sample on the centre-of-rotation, while the lower ones move the rotation axis into the FOV and change the propagation distance. All axes have sub-micrometre positioning accuracy and are encoded. The sample mount is compatible with standard SEM stubs. Commonly the sample itself is fixated inside a Kapton tube for easier handling.

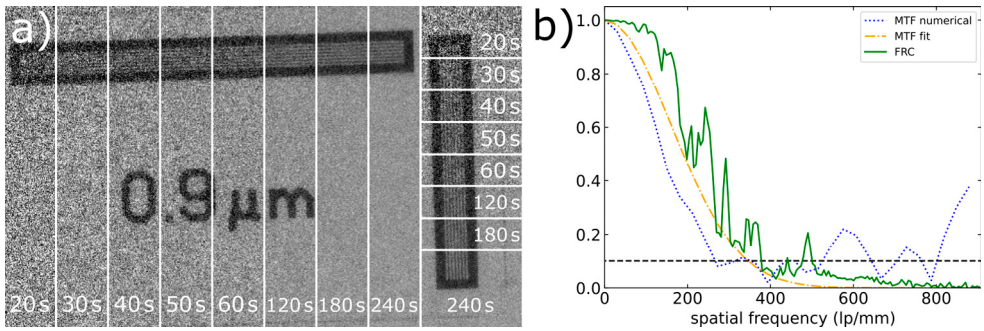

Figure 3.5: Spatial resolution of the lab setup. a) JIMA bar pattern with 0.9 µm bars imaged at different exposure times. b) MTF and FRC curves. The MTF was measured using an edge in the JIMA pattern and analysed both numerically and via fitting of the edge with a Gauss blurred error function and extracting the fit parameters. The FRC was calculated using an image of the JIMA pattern. Reproduced with permission from **paper I** © IOS Press.[49]

The chosen detector, the Rigaku XSight Micron CCD camera, comes with the useful option to exchange the objective depending on the desired FOV and resolution. Moreover, we acquired a customized objective without a built-in scintillator. Together with a scintillator mount that is directly attached to the objective, the same setup can thus be used to test scintillators under real measurement conditions. This is a substantial advantage considering that most material science labs that work on scintillator development have only limited access to setups that are designed for high-resolution X-ray CT. In many recent publications in this field either the photosensor and/or visible light optics themselves cannot reach resolutions better than several tens of lp/mm (see chapter 5). Judging if the resolution is limited by the scintillator or the sensor is thus difficult. On the other hand, time at synchrotron radiation facilities for high resolution measurements is often challenging to get, sparse and the dose rates sometimes too high to study degradation mechanisms in detail. The first results of our lab-based scintillator studies are presented in detail in chapter 5 and **paper V**.

A detailed characterization of the setup is provided in **paper I**. In summary we achieve a spatial resolution of 1.3 µm at the 10% threshold of the MTF, measured via

the slanted edge method as well as with FRC and JIMA pattern (see chapter 2.2 and fig. 3.5). In 3D we achieve a similar resolution to 2D which confirms the high mechanical stability of the setup over long measurement times.

An introduction to phase contrast and how it is realized in our setup will follow in the next chapter. It includes the summary of a dedicated study on finding the optimal experimental geometry for PB-PCI which is presented in **paper II**.

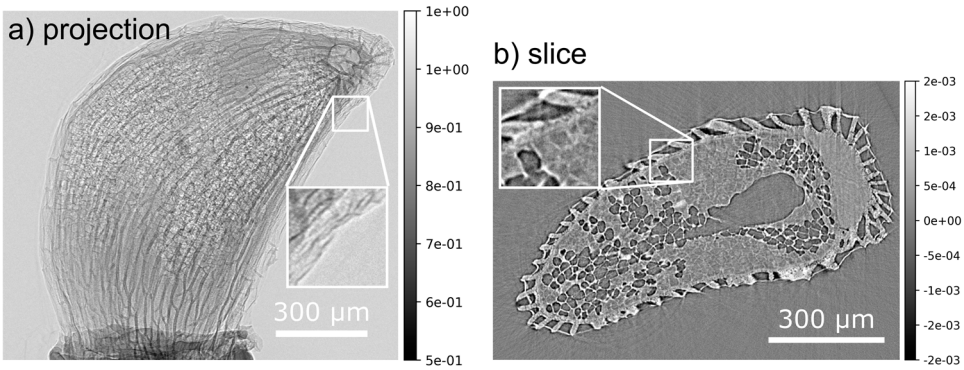

Figure 3.6: Tomography results using the lab setup. Single projection image and slice through a tomography reconstruction of a blueberry seed acquired with the lab setup. Reprinted with permission from **paper I** © IOS Press.[49]

3.2.2 Alignment

Roll and Pitch Angle

Even with careful mounting, it is likely that the rotation axis has a slight tilt towards the optical axis. Commonly the tilt in the detector plane is referred to as the *roll angle*, while the tilt along the optical axis is named *pitch angle*. Both tilts can cause artefacts in the tomography reconstruction. The roll angle can be easily identified and corrected in post-processing by a slight rotation of the images (see chapter 2.3.2). While it is also possible to correct for the pitch angle during reconstruction if the complete geometry is known (for example by using algebraic reconstruction algorithms, see chapter 2.3), it is not as straight forward. Instead, we chose to account for the pitch angle experimentally.

Since our setup does not contain a goniometer to correct the tilts directly, an approximate correction can be performed using the linear stages.[50] To do so, the source and detector are slightly vertically offset to each other (y axis), thus re-defining the optical axis in a way that makes it perpendicular to the tilted rotation axis. Since the source is approximately isotropic, this does not change the illumination if the pitch is smaller than the opening angle of the source cone.

This procedure will not correct that the detector is not perfectly perpendicular to the optical axis, which causes a slight skew of the projected images (i.e., the upper pixel rows will have a different magnification than the lower). Luckily, for small pitch angles and low magnification this skew is equally small and normally negligible compared to the detector resolution. For high magnifications, this effect becomes more severe.

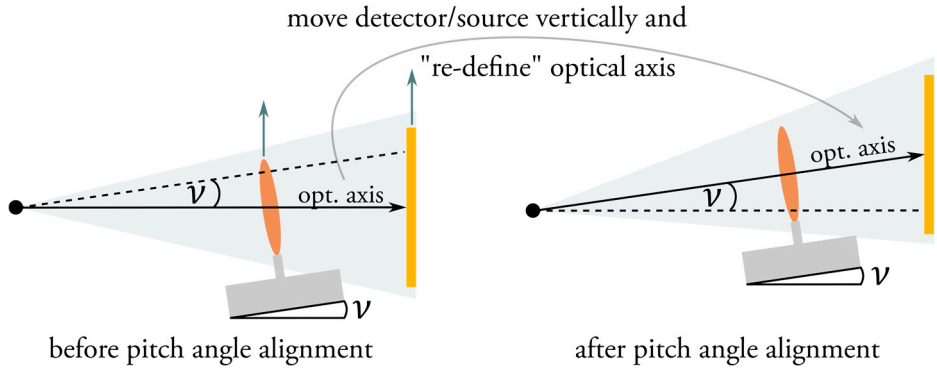

Figure 3.7: Illustration of the experimental pitch angle compensation without the use of a goniometer. The optical axis is 're-defined' from horizontal to tilted by moving the detector vertically relative to the source. How much the detector (or source) needs to move is defined by the pitch angle ν and source-detector distance. Note that ν is exaggerated for sake of clarity.

Scintillator Mount

One of the distinctive features of our setup is the possibility to mount a different scintillator, while leaving the rest of the setup unaffected. The scintillator is mounted in front of a special objective that is identical to the commercial high-resolution objective but has no built-in scintillator. The focal plane of this objective is about 1.2 mm outside of the housing, which makes it difficult to fit an additional motorized stage without interfering with the tomography stage. Instead, we use a customized kinematic optical mount that is attached directly to the camera housing via brackets. The mount has three micrometre screws that allow us to align the scintillator with the focal plane (see fig. 3.4c). Since the depth of focus of the optics is only a couple of micrometres, we are limited to flat and thin scintillators. The scintillator itself is mounted on a detachable magnetic slide with a pinhole. This makes it possible to change the scintillator while keeping the (coarse) alignment intact. The alignment via the micrometre screws is manual, therefore it is performed by using UV illumination and the video function of the camera.

Since the camera is sensitive to visible light, any stray light needs to be blocked in the actual measurement, for example by using an optical blanket to cover the whole setup. Any remaining light can be corrected for via the flat field correction. If necessary, a final fine alignment can be performed with X-rays, using a sharp edge. The mount is

designed in a way that makes absorption contrast imaging and tomography at small sample-detector distances possible, as demonstrated in **paper V**.

3.2.3 Outlook

There are several aspects of the setup that can be improved in the future. They are mostly about reducing measurement and alignment time, convenience of use and reproducibility.

A motorization of all components, including the detector and source in x, y and z would improve the operational convenience and quicken the alignment procedure substantially whenever a change in the setup geometry is wanted. Ideally a (motorized) goniometer would be placed under the sample tower. Although the alignment is possible without, this would improve the control over the experimental geometry.

Although the used source satisfies the design requirements it is currently the bottleneck for measurement speed and noise. More flux, as provided by a rotating anode or metal jet source, would make faster acquisitions possible and open perspectives for other sample systems with low contrast, dynamic behaviour, or higher absorption.

The sample mounting is currently based on SEM stubs and attachment with various tapes/glues. Since many samples have a cylindrical shape (or can be embedded in a Kapton tube), a mounting option with a more reproducible centre alignment, for example with a Huber head or OMNY pin mount, would reduce the alignment times. A better and motorized observation microscope for alignment would improve the alignment process further.

Although the control software combines all components in a python library, the usage is currently command line-/script-based. This is sufficient for the expert user, but a graphical user interface would improve the user experience, especially during teaching.

4 Phase Contrast Imaging

Traditionally the contrast used in X-ray imaging and tomography is based on variations of the local absorption coefficient μ, as has been discussed in chapter 2. However, it is also possible to use the phase shift, i.e., the refraction or scattering, as a contrast mechanism.

At this point it is often argued that phase contrast naturally dominates over absorption contrast due to the different orders of magnitude between β and δ especially for higher energies (see fig. 2.3). However, this overly simplifies the argument since both parameters describe very different wave properties that cannot be compared directly (see chapter 2.1). Instead of the absolute value of δ, the image contrast depends more on the sensitivity of the respective phase imaging technique. Nevertheless, it has been found that, depending on the sample and phase contrast method, an increased contrast of up to two orders of magnitude can be observed.[51, 52]

Similar considerations have led to the development of phase contrast modes in traditional visible light microscopy[53] and electron microscopy[54] and the first demonstration of phase contrast using an X-ray interferometer was reported already in 1965 by Bonse and Hart.[55] However, the difficulties in making efficient X-ray optics as well as high-coherence sources have delayed the real breakthrough of X-ray phase contrast imaging to the mid-1990s. Since then, fuelled by the availability of 3rd generation synchrotron radiation sources[56] and micro-focus sources, many new techniques have been proposed. Among others, phase contrast finds applications in biomedical and clinical imaging,[6, 57-59] material science,[5, 60] archaeology,[3] metrology and wavefront sensing.[61, 62]

This chapter contains a briefly overview of some phase contrast imaging methods before it focusses on one specific method, propagation-based phase contrast imaging (PB-PCI). Finally, I will discuss how this technique can be implemented in laboratory setups, including the key findings from an optimization study performed with the setup introduced in the previous chapter, a commercial Xradia system (see **paper II**) and a high-magnification setup using a nano-focus source (**paper III**).

4.1 Overcoming the Phase Problem

The high frequency of X-rays (1 nm $\approx 3 \cdot 10^5$ THz) makes it impossible to measure the phase shift directly. Instead, the intensity of the wave is measured, which is the squared absolute of the complex wave field $I = |\psi|^2$. The phase information is thus lost in the measurement process. This is commonly referred to as *'the phase problem.'*

Over the years many strategies to retrieve phase information from intensity measurements have been developed.[63] Broadly, they can be grouped into near field and far field approaches, according to the distance between sample and detector. Often it is convenient to think of different distances as *imaging regimes*, meaning that specific approximations are valid, and a certain type of contrast is dominant in this range of distances. A convenient measure for this is the *Fresnel number*

$$N_F = {a^2}/{\lambda z_2}. \tag{4.1}$$

It depends on the propagation distance z_2, the sample feature sizes a and the X-ray wavelength λ, thus combining the key parameters of the experiment. For microscopy, the feature size of interest is usually close to the resolution.

When increasing the propagation distance z_2 for a given feature size and wavelength, one moves from the contact regime ($N_F \gg 1$), first into the near field regime ($N_F \geq 1$), then the holographic regime ($N_F \leq 1$) and eventually into the far field regime ($N_F \ll 1$).

This thesis focusses on phase contrast imaging in the near field. From eq. (4.1) it is apparent that the near field regime for X-rays is experimentally more accessible than for visible light imaging since the wavelength is shorter. Holographic and far field imaging techniques usually require a high degree of spatial coherence and are thus predominantly implemented at synchrotron radiation sources. Some of the most common of these techniques are holography,[64] coherent diffractive imaging (CDI)[65] and ptychography.[66]

In the near field the available methods can be grouped into interferometric and non-interferometric. Note, that interferometric here means the explicit use of an interferometer, like a set of crystals or gratings, not the involvement of interference effects. All methods aim at encoding the phase information into a modulation of the measured intensity, which can then be decoded either optically or computationally in the data processing step.

4.1.1 Grating-based Techniques (interferometric)

Grating-based techniques use one or several gratings to encode and decode the phase information in the interference pattern of the grating. One of the most popular is Talbot imaging. It is based on the *Talbot self-imaging effect* of periodic gratings at specific distances behind the grating, the Talbot distances. Traditionally a phase grating right after the sample and a second absorption grating in front of the detector are used.[67]

The first grating splits the beam into diffraction orders, with the low orders carrying the main intensity. Since the wavelength is much smaller than the grating period the angle between the first and minus first diffraction order is very small and they mostly overlap, so that they can form a self-imaging interference pattern (*fringes* of the same period as the grating) downstream.[68] Any changes of the wavefront induced by the sample will lead to local displacement and/or damping of these fringes. The grating period is in the range of a few microns which makes it challenging to detect them directly. Therefore, a second absorption grating with the same period is scanned in front of the detector, creating a measurable Moiré pattern to read out the fringes.[69] This is known as *phase stepping*. The second grating can be omitted if the detector resolution is higher than the frequency of the first grating. Each individual image is proportional to the absorption and the first derivative of the phase shift in the sample, but both can be extracted individually from the stepping series.

In laboratory systems with an extended source size an additional absorption grating between source and sample can be used to divide the source into smaller secondary sources (*Talbot-Lau imaging*). By doing this, grating-based techniques can relax the requirements on spatial coherence, which makes them popular for laboratory setups.[70]

4.1.2 Mask-based Techniques (non-interferometric)

Like grating-based techniques, mask-based techniques detect the refraction due to the sample (first derivative of the phase shift). A mask is used to pattern the illumination. The sample refraction will cause slight changes of this pattern, which can be detected. In contrast to grating-based techniques, they do not rely on interference from the masks[71] and mask-types therefore range from defined regular patterns to completely random. The decoding step can be either assisted by a second mask or purely computational. Here I give two examples of mask-based techniques: edge-illumination and speckle imaging.

Edge-illumination imaging uses an absorption mask between source and sample to create several sufficiently collimated and separated beamlets.[72] These beamlets are aligned with the edges between detector pixels and insensitive regions on the detector. The insensitive regions can either be part of the detector chip itself or created by an

additional mask in front of the detector. When the beamlets pass through interfaces in the sample they will be slightly refracted, causing them to move over the edge of the pixel. The detected intensity in each pixel therefore will be increased or decreased compared to the flat field intensity. Note that this intensity change happens only if the beamlet hits an interface in the sample, since the refraction angle is proportional to the first derivative of the phase, not the phase itself. The image will therefore show an enhancement of the sample interfaces. Like in grating-based techniques a single image is proportional to a mix of attenuation and phase information. For separation and quantification of β and δ several images with displaced source masks can be used. Moreover, in multi-image acquisitions the dark field image which is proportional to sub-resolution scattering can be extracted.

Near-field speckle imaging uses a random phase mask (for example a fine-grained sandpaper) to create a highly structured wave front. In its simplest form it compares the speckle pattern with and without the sample. Even if the sample has no detectable absorption, the phase shift in the sample will change the wavefront enough to make the speckles move slightly with respect to the image without sample. The technique is experimentally quite simple, but the shift of the speckles needs to be extracted computationally via a suitable image analysis algorithm. Like Talbot and edge-illumination imaging, speckle imaging can yield a dark and bright field image simultaneously.[73-76]

4.2 Propagation-Based Phase Contrast Imaging

PB-PCI is experimentally the simplest phase imaging technique since it does not need any additional optical elements or multi-exposures. However, it requires a certain degree of spatial coherence and has thus initially been proposed as a synchrotron radiation technique. Recently, the availability of micro- and nano-focus laboratory sources and high-resolution detectors has popularized it also in the lab.[77-79]

PB-PCI relies on the near field interference of phase shifted sections of the wave front upon propagation after the sample. After propagation, bright and dark *fringes*, commonly referred to as *edge enhancement*, can be observed around interfaces in the sample. This helps to distinguish sample regions that might not have observable contrast in absorption.

In the following section I will derive how this effect can be understood and described by the *transport-of-intensity equation* (TIE). The derivation will start from the free-space propagation operator for electro-magnetic waves (for an introduction to waves see

chapter 2). Subsequently, I will present one of the main phase retrieval approaches for PB-PCI and how it can be used in combination with tomography.

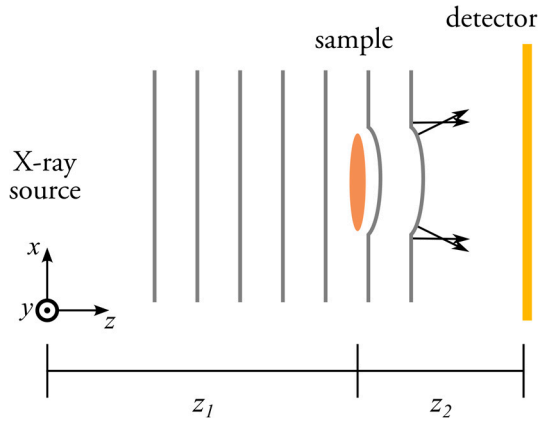

Figure 4.1: Sketch of a typical PB-PCI setup, illustrating the phase shift that provides the intensity modulation. The source illuminates an object at distance z_1 which causes a phase shift and accordingly bent wavefronts (scale exaggerated for sake of clarity). Upon propagation differently shifted parts of the wave interfere. A detector positioned at a distance z_2 after the sample is measuring the intensity pattern which contains absorption information as well as additional intensity modulations (fringes) due to the interference around interfaces. Note that only one fully coherent plane wave is shown here, for the effect of spherical waves and an extended incoherent source, see chapter 4.3.

4.2.1 Free-space Propagation

The free-space propagation of a wave field from the exit plane z_{exit} to a plane at the propagation distance $\Delta z = z_2$ can be described by the *diffraction operator* D_{z_2}. The operator can be derived from the solution of the Helmholtz equation (see eq. (2.3)) for a decomposition of a wavefield into elementary plane waves. The full derivation of the diffraction operator is outside of the scope of this thesis, but the interested reader can find a treatment in respective textbooks.[17] Here I will only state the resulting operator formulation. It can be expressed as a convolution of the exit wave ψ_{exit} directly behind the sample with a scalar plane wave $\exp(iz_2k_z)$, performed as a multiplication in Fourier space

$$\begin{aligned}\psi(x,y,z_{tot}=z_1+z_2) = D_{z_2}\psi_{exit} &= \mathcal{F}^{-1}\big(\exp(iz_2k_z)\,\mathcal{F}(\psi_{exit})\big)\\ &= \mathcal{F}^{-1}\left(\exp\left(iz_2\sqrt{k^2-k_x^2-k_y^2}\right)\mathcal{F}(\psi_{exit})\right).\end{aligned} \tag{4.2}$$

Here, the inverse Fourier transform $\mathcal{F}^{-1}$ is taken only over the transversal Fourier space coordinates, $k_{x/y}$. Note that the subscript 'exit' (as in z_{exit}, ψ_{exit}) is used to explicitly

signify the passage of the wave through the sample, meaning the wave has undergone absorption and phase shift (see chapter 2.1), while z_1 is the sample position relative to the source and z_2 is the distance between sample and detector. The origin of the coordinate system is located at the source and the source-detector distance is $z_{tot} = z_1 + z_2$ (also see magnification geometry in chapter 4.3). For thin samples where the projection approximation holds z_1 and z_{exit} can be treated as equivalent.

Now, let us assume that in the near field all non-negligible plane wave components of the wave field are paraxial (see chapter 2.1). This means the wavevector component k_z along the optical axis is large compared to k_x and k_y, so that $k_z = \sqrt{k^2 - k_x^2 - k_y^2} \approx k - \frac{k_x^2+k_y^2}{2k}$, with $k = 2\pi/\lambda$. Using this assumption, we can move the factor $\exp(ikz_2)$ out of the inverse Fourier transform. The free-space propagation is then considered to be in the Fresnel regime, and we find the *Fresnel diffraction operator* $D_{z_2}^F$ to be

$$\psi(x,y,z_{tot}) \approx D_{z_2}^F\, \psi_{exit} = \exp(ikz_2)\, \mathcal{F}^{-1}\left(\exp\left(-iz_2 \left(\frac{k_x^2 + k_y^2}{2k} \right) \right) \mathcal{F}(\psi_{exit}) \right). \tag{4.3}$$

4.2.2 Transport-of-intensity Equation

Next, let us assume that the propagation distance z_2 is sufficiently small to also replace the second exponential function in eq. (4.3) by the first two terms of its Taylor expansion

$$\exp\left(-iz_2 \left(\frac{k_x^2 + k_y^2}{2k} \right) \right) \approx 1 - iz_2 \left(\frac{k_x^2 + k_y^2}{2k} \right). \tag{4.4}$$

If we apply this form of Fresnel diffraction to the exit wave $\psi_{exit} = \sqrt{I_{exit}(x,y)} \exp\left(i\phi_{exit}(x,y)\right)$ derived in chapter 2.1.2 and employ the Fourier derivative theorem

$$\frac{d}{dx} g(x) = \mathcal{F}^{-1}\left(ik_x \mathcal{F}\left(g(x) \right) \right), \tag{4.5}$$

we can replace the transversal Fourier components $k_{x/y}$ with the respective transversal gradients $\frac{d}{dx}/\frac{d}{dy}$ and arrive at a formula for the intensity $I(x, y, z_{tot})$ in the detector plane based on the intensity at the exit plane I_{exit}

$$I(x, y, z_{tot}) = |\psi(x, y, z_{tot})|^2 = I_{exit} - \frac{z_2}{k}\nabla_\perp[I_{exit}\nabla_\perp\phi_{exit}]\,. \tag{4.6}$$

Moreover, if the sample has a weak absorption contrast (all features absorb similar), the transversal derivatives of I_{exit} will be small and can be neglected. With this we find a simple expression for the propagated intensity

$$I(x, y, z_{tot}) = I_{exit}\left(1 - \frac{z_2}{k}\nabla_\perp^2\phi_{exit}\right). \tag{4.7}$$

This is known as the *transport-of-intensity equation* (TIE) and provides the foundation of some of the most common phase retrieval approaches in PB-PCI.[80] According to the TIE the intensity modulation is proportional to the propagation distance and the local transverse Laplacian, i.e., the second derivative of the integrated phase shift ϕ_{exit} of the sample. This means that the effect is strongest at sharp interfaces or edges in the sample. The second derivative of an edge is a pair of positive and negative fringes adjacent to the edge location – hence the name edge enhancement.

Before we move on, let us briefly review the approximations necessary to arrive at this formulation and their practical implications:

- paraxial approximation (propagation along the optical axis, Helmholtz equation)
- projection approximation (weak scattering)
- small propagation distance z_2 (large Fresnel numbers)
- negligible wave-front tilt directly after the sample (weak scattering)
- weak absorption contrast (homogeneous sample)
- monochromatic, fully coherent wave (plane wave)

The Fresnel number introduced above (see eq. (4.1)) helps to estimate suitable experimental propagation distances z_2: for samples with micrometre features and a wavelength around 1 Å (12 keV) the common distances for PB-PCI are in the centimetre range.

The sample needs to be weakly scattering, which is often fulfilled if it is thin and/or composed of light materials. Similarly, the absorption contrast should be low, which is intuitive since otherwise traditional absorption contrast imaging is sufficient. This is best fulfilled for homogeneous samples.

Note that the image will contain a mix of both absorption information I_{exit} and information about the second derivative of the phase $\nabla_\perp^2\phi$. How we can retrieve the phase information from such an image will be discussed in the next section.

4.2.3 Paganin Filter

The TIE predicts that the detected image after free-space propagation is a mixture of absorption and phase information. A decoding or phase-retrieval step is necessary to separate them. To this end, several phase retrieval approaches for PB-PCI have been developed.[78, 81-85] Since two unknowns need to be retrieved, they either require several images at different distances, iterative algorithms or stringent assumptions about the sample composition.[84, 86-88]

One of the most used and powerful tools is the so-called *Paganin filter*.[89] It is based on the inversion of the TIE for a single propagation distance. It was originally derived for monochromatic illumination and single material samples and assumes a linear proportionality between δ and β. With these assumptions and prior knowledge about the material a 'projected thickness image' can be retrieved. If either is missing, it still can be used to increase the contrast qualitatively. Before we discuss its applications, let us briefly sketch the main derivation steps.

As we have seen in chapter 2.1, we can describe the intensity I_{exit} at the exit surface of a homogeneous sample with the Beer-Lambert law eq. (2.12), relating it to the local projected thickness $T(x,y)$ and the absorption coefficient μ. Similarly, the phase ϕ_{exit} is proportional to δ, see eq. (2.13). Inserting these into the TIE (4.6) and using the identity

$$\begin{aligned}\nabla_\perp[I_{exit}\nabla_\perp\phi_{exit}] &= \nabla_\perp I_{exit}\nabla_\perp\phi_{exit} + I_{exit}\nabla_\perp^2\phi_{exit}\\ &= \frac{\delta k}{\mu} I_0\nabla_\perp^2 \exp\big(-\mu T(x,y)\big)\end{aligned} \tag{4.8}$$

we arrive at

$$I(x,y,z_{tot}) = I_0\left[1 - \frac{\delta k}{\mu}\frac{z_2}{k}\nabla_\perp^2\right]\exp\big(-\mu T(x,y)\big). \tag{4.9}$$

Using the Fourier transform identity $\mathcal{F}\big(\nabla^2 g(x,y)\big) = -\big(k_x^2 + k_y^2\big)\mathcal{F}\big(g(x,y)\big)$ and applying a logarithm we can solve for the projected thickness

$$T(x,y) = -\frac{1}{\mu}\log\left\{\mathcal{F}^{-1}\left[\frac{\mathcal{F}\left(I_{proj}\right)}{1+\frac{z_2\,\delta\cdot\left(k_x^2+k_y^2\right)}{\mu}}\right]\right\}. \qquad (4.10)$$

This means we can retrieve the thickness from a single, normalised, and flat field corrected PB-PCI image $I_{proj} = I(x,y,z_{tot})/I_0$ measured at distance z_2 behind the sample. Mathematically, the Paganin filter corresponds to a Lorentzian low-pass filter applied in Fourier space and therefore dampens the highest spatial frequencies in the image. This entails a smoothing of the signal, and an efficient denoising. If the spatial frequencies close to the Nyquist frequency are dominated by noise, meaning that the spatial resolution is lower than the Nyquist frequency, the filtered image does not necessarily loose resolution. Nevertheless, a different filter kernel that better preserves high frequencies can be used in order to maintain finer details.[90]

Figure 4.2 shows the effect of the Paganin filter on a real PB-PCI image of polymer fibres. In the original image the fibres have only little (absorption) contrast compared to the background but show fringes around their edges. After filtering the contrast is increased and the fringes suppressed.

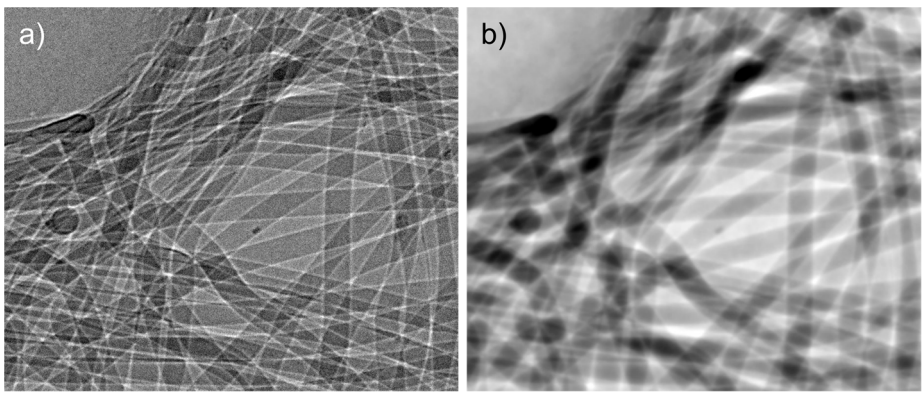

Figure 4.2: Effect of the Paganin filter. a) PB-PCI image of a filter layer from a face mask with pronounced edge enhancement fringes around the polymer fibres. b) Paganin filtered version of the image in a). Note the suppression of the edge enhancement fringes and the increased contrast.

Since most samples contain several materials choosing a single δ and μ will not model all interfaces equally well. In the image this will look like some of the fringes are still present after applying the filter, while some interfaces are overly blurred. To overcome this issue but still retain the simplicity of the retrieval step, multi-material algorithms

have been developed, that create composite images with locally applied mono-material filters.[91, 92]

4.2.4 Phase Contrast Tomography

Like absorption contrast tomography, phase contrast can be used to measure 3D information. Traditionally this is done by first performing the phase retrieval on the projection images according to the used phase contrast technique and then reconstructing the volume. For some combinations of phase retrieval techniques and tomographic reconstructions, such as the Paganin filter above and FBP (see chapter 2.3), it is computationally favourable to combine them directly into one step since they both involve a filtering in Fourier space.[93, 94]

Moreover, it has been shown that under certain conditions the phase retrieval can be performed as an operation directly on the reconstructed 3D volume instead of the 2D projections, essentially switching the order of the reconstruction steps.[95-97]

4.3 PB-PCI at a Laboratory Setup

The above derivation assumed a monochromatic, plane wave which is fully coherent. Laboratory sources usually do not fulfil these assumptions: they are polychromatic, have an extended source size and divergent wavefronts. Moreover, real detectors introduce noise, as well as a limited sampling and resolution (see chapter 2 & 3)

This chapter deals with the implications this has on PB-PCI. Besides amending the theory presented above, experimental results of geometry optimization studies performed with three different setups are provided. The full studies can be found in **paper II** & **III**.

4.3.1 Divergent Beams: Fresnel Scaling Theorem

In laboratory setups the illumination can often not be treated as a plane wave, because the source is close to the object and not ideal. An expanding spherical wave is thus a better approximation. Since the source aperture limits the radiation to one direction, this type of illumination is called *cone beam*. It accounts for the divergence of the source, while still assuming a locally flat wavefront.

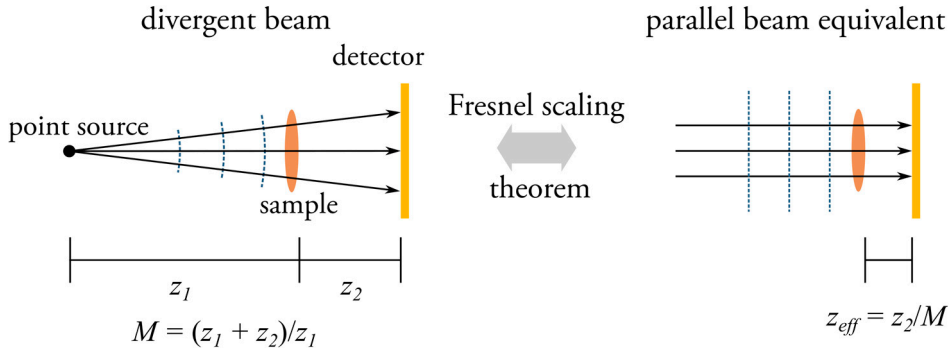

Figure 4.3: Illustration of the Fresnel scaling theorem. For a weakly scattering object illuminated by a point source an equivalent image can be found under parallel beam illumination with appropriate scaling of the distances. This makes it possible to describe a divergent beam scenario using a scaled version of the Fresnel diffraction theory discussed in chapter 4.2.

For divergent sources, the wavefronts expand with increasing distance. Accordingly, the geometrical magnification $M = (z_1 + z_2)/z_1$ needs to be considered. Conveniently, the *Fresnel scaling theorem* enables us to treat the case of a divergent source as a scaled version of the plane wave case if the projection approximation and paraxial approximation are met.

The Fresnel scaling theorem states that for any Fresnel diffraction pattern at sample-detector distance z_2 generated by a divergent beam illumination of a weakly scattering object (projection approximation) with a sufficiently large source-sample distance z_1 (paraxial approximation) an *equivalent* parallel beam illumination image exists. It can be derived by applying the free-space propagator (see eq. (4.2)) on a spherical exit wave ψ_{z_1} (divergent beam)

$$\psi_{z_1}(x, y, z_{exit}) = \psi_\infty(x, y, z_{exit}) \exp\left(\frac{ik}{2z_1}(x^2 + y^2)\right) \tag{4.11}$$

where $\psi_\infty(x, y, z_{exit})$ describes the exit wave for the case of plane wave (parallel beam) illumination, which is independent of the source distance z_1 and only depends on the wave-sample interaction. For a full derivation see respective textbooks.[17]

When performing the propagation, it becomes apparent, that the divergent source I_{z_1} and parallel beam intensities I_∞ are related via a scaling operation:

$$I_{z_1}(x, y, z_1, z_2) = \frac{1}{M^2} I_\infty\left(\frac{x}{M}, \frac{y}{M}, z_{eff} = \frac{z_2}{M}\right). \tag{4.12}$$

This means the divergent beam image at z_2 is equivalent to 1) an image taken under parallel beam illumination at z_2/M behind the sample, which is then 2) magnified by the magnification factor M and finally 3) intensity scaled by a factor of $1/M^2$ to provide energy conservation.[17]

The Fourier scaling theorem can be used to transform the TIE and Paganin filter to a cone beam scenario. Instead of z_2 the fringes then depend on the effective propagation distance $z_{eff} = z_2/M$ and effective pixel size $p_{eff} = p/M$ and the intensity of the image is scaled by a factor of M^2. The intensity scaling cancels itself out by the normalisation with the flat field image and the effective pixel size results in effective spatial frequencies $k_{x/y,eff} = M \cdot k_{x/y}$.

The Fresnel number eq. (4.1) changes accordingly to

$$N_F = {a^2}/{\lambda z_{eff}} = M \cdot {a^2}/{\lambda z_2}. \tag{4.13}$$

Practically speaking, this means that even for large z_2 we can stay in the PB-PCI regime ($N_F \geq 1$) if the magnification is high (short z_1). Note that a short distance z_1 reduces the coherence length on the sample (see chapter 2.1.3). This is therefore only possible if the source size is sufficiently small (smaller by a factor of M to reach the same coherence length, see eq. (2.22)).

4.3.2 Optimization of Laboratory Setups

According to the TIE, PB-PCI is sensitive to the distances in the setup, as well as the X-ray energy (see eq. (4.7)). This means that the height and separation of the edge enhancement fringes depend on the experimental geometry, the source, and the detector characteristics. Accordingly, a setup can be optimized to provide well defined fringes.

This chapter explores the optimization of common laboratory setups, based on the findings of **paper II** & **III**. First, a short literature review will provide context before summarizing the main findings of our studies regarding magnification and spectrum.

Review of Optimization Studies

In the 1990s, soon after it became clear that PB-PCI was experimentally possible in the lab, theoretical frameworks to describe and simulate the contrast formation were presented. Based on simulating the wave propagation these studies first assumed plane wave illumination, but soon were amended for spherical waves,[14, 98] extended sources,[79] and polychromatic radiation.[99] These early treatments laid the foundation to

understand the physics behind the observed effects and have subsequently been used for many simulation studies.

Since the early 2000s the group around Wilkins, Paganin and Gureyev at CSIRO (Australia) published a series of mostly theoretical optimization studies. They provide a thorough mathematical discussion of the contrast formation alongside some practical rules both for 2D and 3D imaging. The same group developed the Paganin phase retrieval filter (see chapter 4.2.3). Although these publications include some experimental data, these are mostly illustrative and/or serve as confirmations for the validity of the simulations.[98, 100-103]

In the early experimental optimization studies the observations were mostly qualitative. In 2003 Donnelly et al. used a low-resolution detector (45 µm pixel size) and a micro-focus W source (10-45 µm spot) for a series of experiments where they investigated the influence of exposure time, binning, tube voltage and source spot size. They concluded that a smaller source is favourable, the fringes are relatively independent of the tube voltage and that medium magnifications yield the most pronounced fringes.[104]

Gui et al. used a µCT setup (13-30 µm source, 24 µm pixel size) at different source sizes and magnifications. Like Donnelly et al. they found that a smaller source size gives a higher contrast. Their optimal magnification was in the range of 2.5-4.5,[105] but they did not provide any general rules which would make it possible to predict the optimal geometry for different source and detector parameters.

In 2015 Bidola et al. used a commercial µCT system (Xradia Versa 500, Zeiss) for a similar study. They went to high magnifications and concluded that the contrast increases with large z_{eff}, although the spatial resolution after phase retrieval decreases, which is consistent with the predictions of the TIE for very small source sizes (see chapter 4.3.1).[106]

Cheng et al. also worked with a high magnification setup (5 µm source, 20 µm pixel size). They included the effect of air absorption and spectral detector sensitivity in their models and concluded that both effects decrease the SNR and contrast. Moreover, they found that a larger z_{tot} increases the contrast but lowers the SNR and deducted an optimal magnification for their setup, but did not provide a more general rule.[107]

Optimizing the Magnification of a Low-Magnification Setup

As we have seen above, the TIE predicts that the relative intensity of the edge enhancement fringes depends on the experimental geometry (see eq. (4.7) and eq. (4.12)). Accordingly, the phase term will increase with increasing sample-detector distance. However, for a real experiment the extended source size and finite detector resolution also need to be considered.

As explained in the coherence section (chapter 2.1.3), a partially spatially coherent illumination will lead to a superposition of slightly offset fringes, which lowers the fringe visibility and looks like a blurring of the image. Similarly, the finite resolution of the detector will only allow fringes of a certain separation to be distinguished. For a setup with magnification M this can be expressed as a convolution (denoted by $*$) with the scaled source distribution S and detector PSF D[102]

$$I_{meas}(x, y, z_1, z_2; M; \lambda) = I\left(\frac{x}{M}, \frac{y}{M}, z_{eff}\right) * S\left(\frac{M}{M-1}x, \frac{M}{M-1}y;\ \lambda\right) * D(Mx, My; \lambda). \tag{4.14}$$

If the source spot has a size σ_s and the detector a resolution σ_d the overall spatial resolution therefore depends on the magnification M

$$\sigma = \sqrt{\sigma_{obj}^2 + \sigma_s^2\left(1 - \frac{1}{M}\right)^2 + \frac{\sigma_d^2}{M^2}} \tag{4.15}$$

where σ_{obj} is the inherent blurring of the object feature itself. This equation assumes Gaussian shaped PSFs (see chapter 2.2) of object, source, and detector. The convolution of a Gaussian with variance σ_1^2 and a Gaussian of variance σ_2^2 is a Gaussian of variance $\sigma^2 = \sigma_1^2 + \sigma_2^2$. In a magnification setting the effective PSFs at a respective common plane (here in the object plane) must be used (see Fresnel scaling theorem).[102] By minimizing σ with respect to M we find that the magnification that gives the best spatial resolution of the system is

$$M_{res} = 1 + \left(\frac{\sigma_d}{\sigma_s}\right)^2. \tag{4.16}$$

Now, we know that a larger propagation distance results in higher fringes but will eventually decrease the resolution when we move away from M_{res}. Therefore, there is a point where the fringes are blurred enough to impede this improvement. Accordingly, the question is: How far can we increase the propagation distance (and thus the magnification) before the loss of resolution will wash out the gain of fringe height in the phase term? Or differently put: At which magnification can we expect the most pronounced fringes?

Theoretically this question can be answered by performing the convolutions in eq. (4.14) for a given sample and setup. For simple object models this can be done analytically, as demonstrated by Nesterets et al. They provide an integral formula to simulate the expected fringe contrast based on different models for the object feature

(single edge, 1D or 2D Gauss feature). By specifying source, detector, and sample properties the expected contrast can then be predicted by numerical integration.[102]

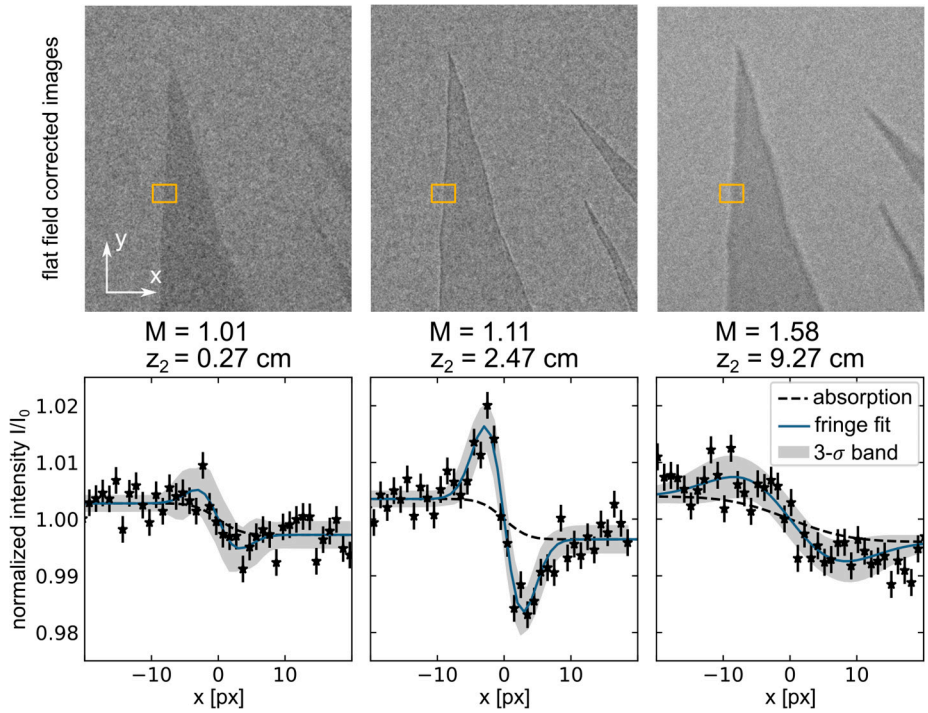

Figure 4.4: Fringe evolution with increasing magnification for a fixed overall distance. Top row shows images of a broken Si_3N_4 membrane (1 µm thick), bottom row the respective extracted 1D data from the yellow ROIs and a fit of the fringes. With increasing magnification, the fringes first grow from barely visible at close contact, then reach a maximum and are eventually washed out when the image becomes blurred due to the size of the X-ray source. Adapted with permission from **paper II** © Optica Publishing Group.[108]

In **paper II**, we combined such simulations for our low-magnification setup with measurements of a single edge of a thin Si_3N_4 membrane. In contrast to most previous publications, we measured many magnifications and found an overall very good match with the simulations.

As shown in fig. 4.4 and 4.5 the fringes first grow with increasing magnification and propagation distance. Note that a higher magnification is here achieved by moving the sample towards the source at fixed z_{tot}. They reach a maximum and then wash out when the blurring from the effective source size becomes dominant. Interestingly, the maximum fringe visibility is reached at a fixed magnification that is independent of the overall source-detector distance (see fig. 4.5). As we show in **paper II**, for a sharp edge ($\sigma_{obj} \approx 0$) this optimal magnification only depends on source size and detector resolution and differs from M_{res} (eq. (4.16)):

$$M_{opt} \approx 1 + \frac{\sigma_d}{\sigma_s}. \tag{4.17}$$

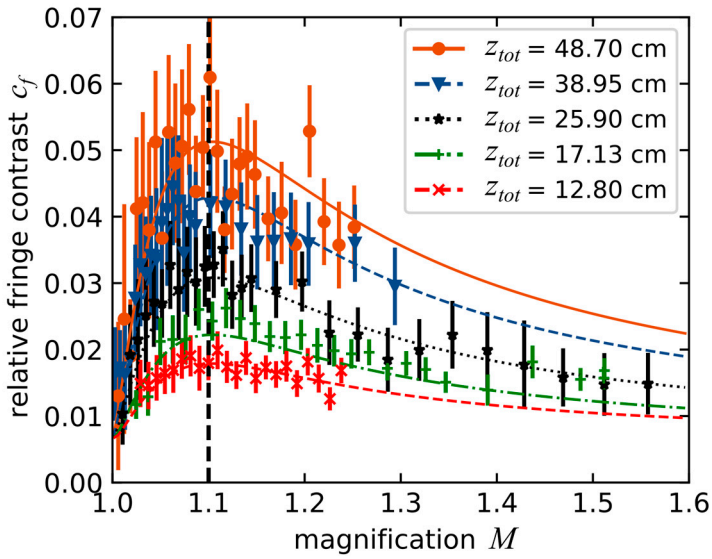

Figure 4.5: Relative fringe contrast vs. magnification for a low-magnification laboratory setup. Five different total distances z_{tot} are plotted. The data points are taken with our lab setup, while the curves are simulations (not fits). A very good agreement between experiments and theory can be observed. The highest relative fringe contrast for each z_{tot} is reached at the same magnification $M_{opt} = 1.1$ that is defined by source size and detector PSF (see eq. (4.17)). The overall contrast increases with longer total distance, due to the higher spatial coherence at the sample position. Note that this comes at the cost of photons, as discussed further in **paper II**. Reprinted with permission from **paper II** © Optica Publishing Group.[108]

Optimizing the Magnification of a High-Magnification Setup

Complimentary to the study at our low-magnification lab setup we performed a similar experiment at a high-magnification setup located at the Division of Medical Radiation Research at Lund University, see **paper III**.

This setup uses a source with a W transmission target (NanoTube N2 60 kV, Excillum) run at 60 kV, which gave a measured electron spot size of $\sigma_s \approx 0.22$ µm. The detector is a sCMOS (Photonic Science) with 9 µm physical pixel size using a GdOS scintillator without additional magnification. All data was recorded with a 2x2 hardware binning resulting in an estimated $\sigma_d \approx 23$ µm. Like in **paper II** a broken Si_3N_4 window of 1 µm thickness was imaged for four overall distances ranging from 14 cm to 34 cm.

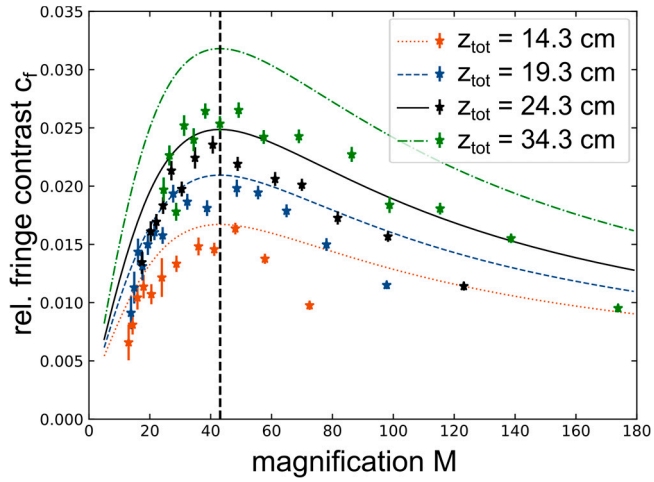

Figure 4.6: Relative fringe contrast vs. magnification for a high-magnification laboratory setup. Experimental data (points) measured with the NanoTube setup and simulations (curves) using $\sigma_s = 0.22$ µm, $\sigma_{obj} = 0.50$ µm and $\sigma_s = 23$ µm for different total distances z_{tot}. The best contrast is reached at a magnification of $M = 42$ independently of the total distance. Adapted from **paper III**.

As for the low-magnification setup, the experiments confirmed that the peak of the fringe contrast is independent of the overall distance (see fig. 4.6). However, in this study, σ_{obj} cannot be neglected in eq. (4.15), since a large ROI along the edge was used to get a sufficient SNR in the lineouts. Any small structuring of the edge within the ROI thus led to an apparent widening of the edge and fringes. Accordingly, the predicted optimal magnification including σ_{obj} is

$$M_{opt} = 1 + \sqrt{\frac{\sigma_{obj}^2 + \sigma_d^2}{\sigma_{obj}^2 + \sigma_s^2}} \,. \tag{4.18}$$

When assuming an object blur of $\sigma_{obj} = 0.50$ µm the optimal magnification for a straight edge imaged in this setup is $M_{opt} = 42$, which is in good agreement with the observed peak in the data (see fig. 4.6). It is noteworthy that in high-magnification setups the influence of σ_{obj} on M_{opt} is much higher compared to the low-magnification case, since M_{opt} is now dominated by the second term in eq. (4.18). This entails that different sample features can have different optimal magnifications. Generally, 'sharper' features (small σ_{obj}) will reach their peak contrast at higher magnifications, while 'softer' features (large σ_{obj}) are more pronounced at lower magnifications (see supplementary information of **paper III**).

Accounting for Polychromatic Radiation

As mentioned in chapter 2, a polychromatic wavefield can be described as a superposition of monochromatic waves. Since the refractive index is energy dependent each of these spectral components will undergo a slightly different absorption and phase shift in the sample. The detected image is a superposition of the respective monochromatic images. Working within the TIE approximation (eq. (4.7)), we can see that the wavelength and refractive index only appear as an intensity scaling factor, which does not affect the position of the phase contrast fringes (nor the absorption image). Spectral incoherence thus will not cause a blurring of the image in the same way as spatial incoherence does. Therefore, PB-PCI is a method that is considered well suited for polychromatic radiation.[14] Nevertheless, using polychromatic radiation entails that simple phase retrieval, using for example the Paganin filter, will not be quantitative anymore and beam hardening effects can occur (see chapter 2.3).[47]

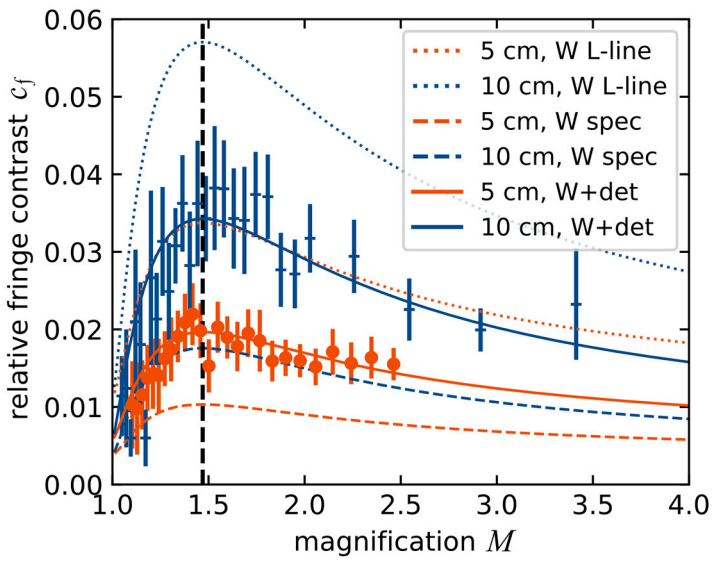

Figure 4.7: Relative fringe contrast over magnification measured with an Xradia (Zeiss). A W-target source at 80 kV tube voltage and a scintillator detector were used. Two different total distances (5 cm and 10 cm) were studied. The different curves represent simulations with different effective energies: the dotted line uses only the L fluorescence line of W (8.4 keV), the dashed line uses an effective energy and refractive index calculated as a weighted sum of the entire W spectrum, while the solid lines also include the spectral sensitivity of the detector. While the L-line simulation overestimates the contrast (underestimates the effective energy), the effective energy of only the source spectrum underestimates the contrast (overestimates the energy). By including the detector sensitivity, the experiment is well modelled. Reprinted with permission from **paper II** © Optica Publishing Group.[108]

If one aims for a semi-quantitative imaging or wants to simulate an experiment correctly, one can account for the average of the refracted index by using a weighted

sum to calculate the *effective energy/wavelength*.[77] This sum will be dominated by the characteristic fluorescence lines of the anode material of the source and can be extended to include air absorption and detector sensitivity.

Several studies have explored the effect of the spectrum on the fringe formation. Olivo et al. demonstrated that in most relevant cases polychromatic PB-PCI can provide images of similar quality to the monochromatic case,[109] while Cheng et al. concluded that polychromatic illumination and air absorption lower both SNR and contrast.[107] So how exactly do we have to understand the effect of the spectrum?

As we have shown in **paper II** the inclusion of the effective energy is crucial if simulations and experimental results should be compared quantitatively. Please note that the non-linear energy dependence of the refractive index (see fig. 2.3) moreover requires to also calculate effective values of δ and β, instead of using the respective value at the calculated effective energy (see supplementary information of **paper II**).

Even though the effective energy of a conventional X-ray tube is dominated by the characteristic lines, the bremsstrahlung will often move the actual value to higher energies. Especially for high voltage sources with heavy metal targets like W, the effective energy will change with the acceleration voltage, too. Moreover, the detector's spectral sensitivity will influence the effective energy. Since the absorption in the scintillators drops at higher X-ray energies this will often lead to lower effective values. How strong the influence of the detector can be on the quantitative accuracy of the simulation is shown in fig. 4.7 and **paper II**, for a commercial X-ray µCT system (Xradia) using a W source.

Including both source and detector in the calculation, as well as the air absorption for large z_{tot}, is therefore necessary to achieve accurate models. Generally, higher effective energies reduce the fringe contrast, as the TIE predicts.

5 Scintillator Detectors

When W. C. Röntgen discovered X-rays, it was by chance - thanks to a scintillator. He saw a faint glow on a barium platino-cyanide screen close to his optically shielded cathode tube, which made him realize that he was observing a new kind of highly penetrating, otherwise invisible radiation.[110] Without this lucky coincidence, X-rays might have taken many more years to be discovered.

To make the invisible visible one needs a suitable detector. Since traditional photographic plates only show insufficient responses to X-rays, the search for a new detection material started immediately after the discovery of X-rays. Already in 1896, a few months after the original discovery, the phosphor $CaWO_4$ was introduced as an X-ray screen by Pupin. Together with ZnS-based powders it is the oldest X-ray scintillator and has continued to be used for more than 75 years.[111]

Today, many different types of scintillators are available, ranging from powders and single crystals to structured nanomaterials. Scintillator fabrication is predominantly the field of material scientists, but the characterization involves testing of the imaging properties of the material. Ideally this is done in a realistic imaging scenario, where the true performance can be assessed. To facilitate this kind of characterization the setup described in chapter 3 was built to be used not only for application studies and method development but also as a test bench for scintillators.

This chapter explores the field of scintillators from the perspective of an X-ray physicist, not a material scientist. First, the mechanisms behind scintillation will be introduced, followed by a brief overview of the most common types of scintillators. In the second half of the chapter the material currently explored in our lab, a metal halide perovskite, is presented in more detail. Finally, the key characterization results of our newly developed $CsPbBr_3$ nanowire scintillator will be summarized (**papers IV**), including the first X-ray tomogram taken with it at our µCT setup (**papers V**).

5.1 Scintillators

A scintillator is any material that has an emission spectrum which is sufficiently separated from its excitation spectrum, like UV/visible emission under X-ray

excitation.[112] The general scintillation mechanism can be described in three main steps: absorption and multiplication, energy carrier transport, and relaxation/emission (see fig. 5.1).

In the first step the X-rays interact with the material. The main interaction process relevant for scintillation in the energy range below 100 keV is photoelectric absorption: an incoming X-ray frees an inner shell electron from its atom, leaving a hole (see chapter 2). This primary high-energy 'hot' electron and 'deep' hole scatter (elastically/inelastically) or trigger non-radiative processes such as Auger emission. The energy that the primary electron loses in these processes excites a cascade of many secondary electrons. These secondary electrons also lose part of their energy via scattering and thermalization (phonon emission) until they energetically reach the conduction band edge. The absorption of one high-energy photon can therefore generate thousands of electron-hole pairs with lower kinetic energy in a cloud around the incident absorption site. The average energy needed to create one electron-hole pair is the *creation energy* and is proportional to the band gap with an empirical factor of 1.5 - 3, usually 2.5.[113, 114] The whole absorption and multiplication step happens on a sub-picosecond time scale. Direct detectors use electrical fields to collect and measure the size of this charge cloud. In scintillators, the electrons and holes instead recombine radiatively, and the emitted light is detected.

In the second step the electrons in the conduction band travel through the material. This transport step takes place over periods of 10^{-12} to 10^{-8} s and the electrons travel over spatial ranges of around 100 nm. It is important to have a low trap density in the material to avoid non-radiative losses and delays in the radiative recombination. Typically trap states can be generated within the bandgap by ionic vacancies, surfaces, defects, grain boundaries or self-trapping in the crystal lattice.[111, 115] It is crucial to already avoid such trap states during fabrication, by improving the crystal growth and surface morphology. The large variety of interactions that can happen during the transport stage makes it complex and highly material dependent. It determines many of the scintillation properties.

The third and last step is the emission of a scintillation photon. This can be either by recombination of an electron and a hole at the band edges, at a luminescence centre or the decay of an exciton.[a] Traditional scintillators are doped to create luminescence centres (for example with Ce, Tb, Eu). The dopants create separate states in the bandgap of the host crystal that define the main emission wavelength. The energy of the emission is therefore smaller than the bandgap, which suppresses re-absorption of the scintillated light.

[a] An exciton is a bound state of an electron with a hole. Due to the binding energy, exciton recombination has a slightly lower energy than that of a free electron-hole pair.

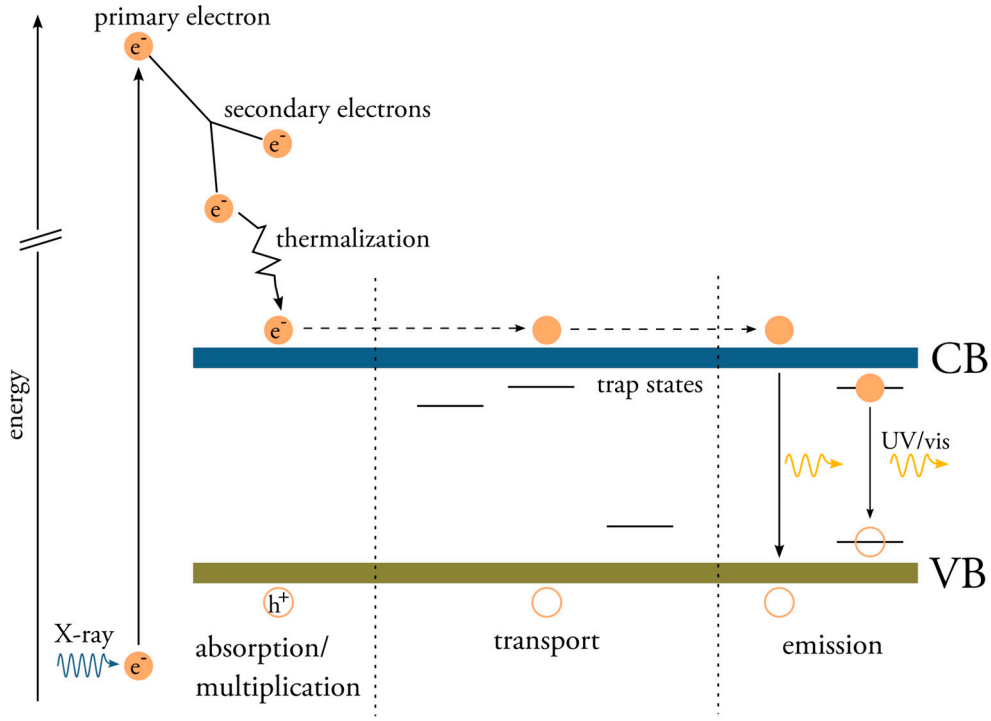

Figure 5.1: Illustration of the scintillation process, to be read from left to right. An incoming high energy photon is absorbed which ionizes an atom (energy axis not to scale). The hot primary electron excites a cascade of secondary electrons that lose energy until they reach the conduction band (CB) edge. During the transport stage the electrons and holes can get trapped and decay non-radiatively. Finally, the electrons and holes re-combine either from the band edges or, if they formed an exciton, from their exciton states.

There are several key parameters to characterise scintillator performance. The main physical metrics are the absorption coefficient, the decay time, and the light yield.[112] A high *absorption coefficient* is important to provide a high number of primary electrons. High-Z materials are therefore favourable. The *decay time* characterises the average delay between absorption and emission. It depends on the specific scintillation process in the material as well as on the properties of the crystal lattice and becomes especially relevant in time-resolved measurements. The *light yield* is given by the number of emitted luminescence photons per deposited energy as photons/MeV.[115] The fundamental limit of the light yield is based on the ratio between the creation energy of the material and the deposited energy.[116]

Besides these key parameters other properties characterise a scintillator and need to be considered when developing an X-ray detector:

- stability: dose (radiation hardness), time, mechanical, temperature, humidity
- detection: emission spectrum matching the sensitivity of the photodetector, flux matching the dynamical range

- sufficiently large Stokes shift[b] to avoid re-absorption
- linearity of the scintillation response with flux/dose
- low afterglow (for clinical CT < 0.1% @ 3 ms)[113]
- low optical scattering for high resolution
- technical aspects: easy fabrication, non-toxicity, machineability
- material and fabrication costs

So far, no material excels in all these points. Therefore, trade-offs depending on the main application are necessary.

5.1.1 Common Scintillator Types

Some of the most popular traditional scintillators are phosphor powder screens, thin single-crystals, ceramics, and (semi-)structured scintillators.

Phosphor powder screens are the oldest type of scintillator. They are cheap and easy to fabricate, but their granular structure is not optimal for microscopy due to scattering of the emitted light. The spatial resolution is approximately proportional to their thickness.[111] A trade-off between resolution (thin scintillator) and stopping power (thick scintillator) is thus often necessary.

Single crystals (SC) offer better resolution and stopping power, but are more expensive and, if thin, more fragile than powder screens. The most common materials are garnets such as $Y_3Al_5O_{12}$:Ce (YAG:Ce) and $Lu_3Al_5O_{12}$:Ce (LuAG:Ce). The high light yields and short decay times of SCs make them attractive. For sub-micron resolutions even a SC scintillator needs to be very thin (1-20 µm). Instead of thinning a bulk crystal, such thicknesses can be achieved by growing SC films epitaxially on a substrate. The challenge is here to avoid scintillation in the substrate itself. Usually, a doped film is grown on an undoped substrate of the same crystal, for example YAG:Ce on YAG or Eu- and Tb-doped gadolinium gallium garnets (GGGs) on undoped GGG. The emission spectra of these SC scintillators are usually fixed and need to be chosen matching to the sensitivity of the photodetector.

Like powder screens, *ceramics* are attractive because of their low cost and scalability. However, they only reach spatial resolutions in the several micrometre range and thus are not considered high-resolution screens.

The fundamental idea of using *structured scintillators* is to increase the scintillator thickness without losing spatial resolution. Columnar structures ('micro-needles') show light guiding properties that allow thicknesses up to several centimetres without substantial loss of resolution.[117] Either columnar grain boundaries are used directly, or core-shell structures are grown. Like in fibre optic plates, the shell reduces crosstalk

[b] The Stokes shift is the energy difference between the absorption and the emission peak.

between the cores. Traditionally the diameter of the needles is in the range of several micrometres, which is not sufficient for high resolution microscopy. Recently similar approaches have been developed with nanowires, which will be discussed later in this chapter.

5.2 Metal Halide Perovskite Scintillators

In the past years *metal halide perovskites* (MHP) have gained attention due to their excellent opto-electronical properties and ease of fabrication. They are studied as candidates for a new generation of solar cells, light-emitting diodes, photodetectors, and laser diodes.[118, 119] Here I will first introduce the properties that make MHPs a suitable material for X-ray scintillators, before discussing some open challenges.

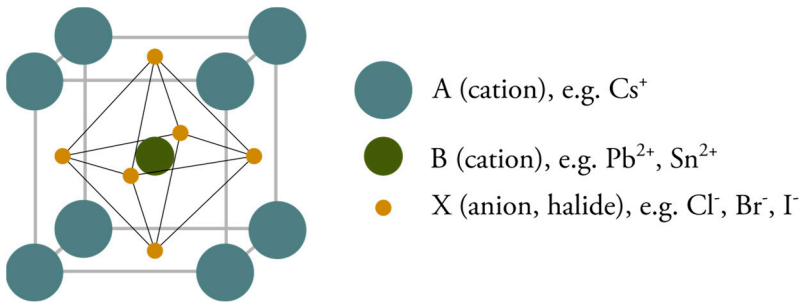

Figure 5.2: Illustration of the perovskite crystal structure in cubic configuration.

5.2.1 Properties as an X-ray Scintillator

Perovskites have the chemical structure ABX_3, where A and B are cations and X is an anion (see fig. 5.2). They are named after the mineral *perovskite* ($CaTiO_3$) but can be composed of any suitable cations and anion which form the same crystal structure. Depending on the composition, they form a cubic, tetragonal, or orthorhombic crystal phase at room temperature.

Many different perovskite materials are currently studied, and a comprehensive overview of their characteristics is outside of the scope of this thesis, but can be found in respective review papers.[115, 120] Here, I will focus on MHPs, with special attention to all-inorganic MHPs, since these are the materials currently studied in our lab.

In halide perovskites X is an anion from the halide group such as Cl^-, I^-, or Br^-. As mentioned above, the light yield is inversely proportional to the optical bandgap, which means that the smaller bandgap (1.6 - 3.1 eV) of halide perovskites when compared to

traditional scintillators (for comparison: CsI: 6.4 eV, NaI: 5.9 eV, $CaWO_4$: 4.6 eV) predicts high theoretical light yields of up to 130,000 - 250,000 ph/MeV.[112, 115] Nevertheless, in practice the light yield is lower, due to losses during the transport stage (non-radiative recombination), self-absorption, or imperfect light extraction (optical coupling).[113] Moreover, the low exciton binding energy in 3D perovskite SCs causes strong thermal quenching, which means that even though MHP SCs show high light yields at low temperatures ($CsPbBr_3$ 50,000 ± 10,000 ph/MeV at 7 K)[121] these drop significantly to about a few hundred ph/MeV at room temperature.[122]

In 2015 Protesescu et al. showed that all-inorganic MHP *nanocrystals* (NCs) have a strong luminescence with a tuneable bandgap at room temperatures, see fig. 5.3.[123] Since then, the research has focussed on assemblies of NCs instead of bulk SCs. The thermal quenching is significantly reduced when they are prepared as NCs or 2D materials[115] and the light yield of $CsPbBr_3$ NCs can reach up to 21,000 ph/MeV at room temperature.[124] Moreover it was reported that surface dangling bonds and point defects, caused for example by vacancies in the crystal lattice, do not form mid-gap states in NCs, which effectively protects them from photo-oxidation and improves the stability compared to SCs.[125]

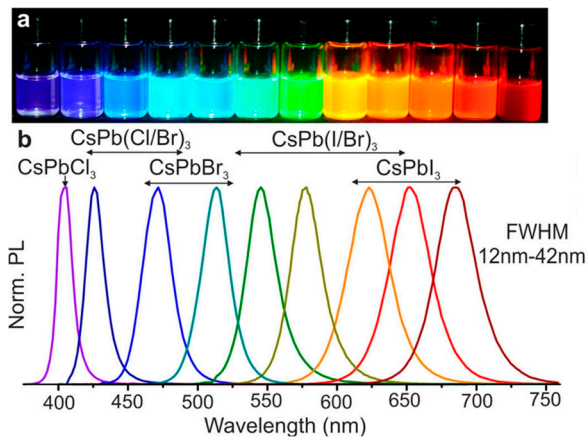

Figure 5.3: **$CsPbX_3$ nano crystals with tunable bandgap depending on the halide composition.** a) Photo of colloidal solutions in toluene under UV lamp (λ = 365 nm). b) PL spectra (excitation with λ = 400 nm for all but 350 nm for $CsPbCl_3$ samples). Reprinted from https://pubs.acs.org/doi/10.1021/nl5048779 © ACS[123]

The emission wavelength of MHPs can be tuned by adjusting the halide composition over the whole visible range from 400 nm to 700 nm, because the ionization potential varies between different halides. This tunability makes them attractive for opto-electronic applications. For scintillators it comes with the advantage of being able to match the emission wavelength with the sensitivity of the used photodetector.

Moreover, a change in halide composition will also influence the *photoluminescence* (PL) yield as well as the decay time, which is inversely linked to the emission wavelength.[112, 126]

Besides their promising performance, the research interest is further fuelled by the inexpensive precursors and simple fabrication: MHP NCs can be grown from solution, at low temperatures. This and the low price of the raw precursor makes their costs competitive with many commercial scintillators (e.g. CsI:Tl) and much cheaper than single crystals such as YAG:Ce or CdZnTe.[120]

5.2.2 Challenges

Although the above-mentioned properties make MHPs promising candidates for a new generation of X-ray scintillators, they still face some serious practical concerns. One of the main challenges for perovskites is their sensitivity to environmental conditions. They are *ionic crystals* and have a low enthalpy of formation and therefore easily react to changes in temperature, humidity, light exposure, gaseous environment, and solvents.[127, 128]

Temperature can cause morphological changes that can be detrimental or beneficial, but also structural changes in the crystal phase. For example, $CsPbBr_3$ which is orthorhombic at room temperature becomes tetragonal above 361 K and finally cubic above 403 K. Although all-inorganic MHPs have been found to be more thermally stable than their organic-inorganic relatives, many of their properties like the emission lifetime and wavelength still undergo changes with temperature: thermally induced PL quenching is common,[129] as well as a blue-shift and broadening of their PL peak with higher temperature.[130]

Due to their ionic nature, MHPs are solvable in polar solvents such as water and alcohol. This makes them sensitive to (air) humidity and is considered one of the main reasons why MHP scintillators degrade over time. When exposed to high humidity phase changes can occur, that strongly influence the PL intensity.[131] Interestingly, some studies have shown that high humidity can also have a beneficial effect on perovskite film formation.[132]

Obviously, the exposure to light is unavoidable in photoelectric applications. Although degradation effects induced by UV and X-rays have been observed, the underlying mechanisms are an active field of research. Again, all-inorganic MHPs show better stability and do not suffer noticeably from photo-oxidation,[125] but the effect of photo-ionisation still needs better understanding.[129] Moreover, photo-aggregation and a shift of the PL peak have been reported for *quantum dot* (QD) films.[133]

A common strategy to mitigate the effects of the environment is surface passivation and protection. Most research on surface protection has been carried out in the context of MHP solar cells, while dedicated studies on the stability of scintillators under X-ray

exposure are relatively sparse. Nevertheless, some of the proposed solutions can also be used or adapted for scintillators. Strategies can be broadly grouped into surface passivation and capping,[134-136] embedding into a matrix[137-140] and in-template growth.[125, 141] Coating or confinement to templates can prevent aggregations that can be induced by temperature or radiation.[133] In-template growth and its effect on the stability will be further discussed in the next chapter.

Besides the instability, there are environmental concerns for MHPs that contain Pb, which is a known environmental toxin. This issue has led to a branch of studies looking for Pb-free alternatives with similar performances, mostly driven by the hope to use them in large scale solar cell applications. Possible candidates are e.g., $CsSnX_3$,[142] or 2D $(C_8H_{17}NH_3)_2SnBr_4$.[143] Even though a Pb-free alternative would be favourable, risk analysis for large scale photovoltaic applications already suggests that the environmental risk is manageable since the amount of Pb is low and proper recycling channels are available.[144] Similar studies for scintillator applications have yet to be performed, but the smaller market and amounts of Pb, as well as the protected lab setting inherent to X-ray detectors make me expect that the risk is even smaller.

5.3 $CsPbBr_3$ Nanowires in AAO

The aim of this project was to fabricate a MHP scintillator suitable for laboratory X-ray μCT. This means that the spatial resolution and light yield of the scintillator needs to be as high as possible, but also that the scintillator needs to be stable over long timescales and under changing environmental conditions. To satisfy these requirements the idea was to grow aligned $CsPbBr_3$ NWs inside an *anodized aluminium oxide* (AAO) membrane. The shape and alignment of the NWs was expected to provide high spatial resolution due to light guiding and directional emission.[145] Moreover, the template would also provide stability and protect most of the NW surface from direct contact with the environment. In the following this scintillator will be referred to as $CsPbBr_3$ NW/AAO.

This chapter will first position our research in the field before presenting some of the key characteristics of our material and how it performs in our tomography setup. The results shown here can be found in more detail in **papers IV** & **V**.

5.3.1 State-of-the-art $CsPbBr_3$ Scintillators

Many different types of $CsPbBr_3$ NCs, such as 0D quantum dots, 1D nanowires and 2D nanoplates, have been proposed as X-ray scintillators, generally showing good

scintillation properties in terms of light yield, resolution and afterglow.[15, 113] An overview of some publications on $CsPbBr_3$ NC scintillators and their performance can be found in table 5.1.

In general, it must be noted that the resolutions reported for most $CsPbBr_3$ scintillators are moderate, in the order of several tens of micrometres. Only few groups have reported the spatial resolution necessary for X-ray microscopy, see table 5.1. To the best of my knowledge, the highest reported resolution to date is 2.4 µm.[146] Since in many publications the used visible light detectors themselves cannot reach resolutions better than several tens of micrometres it stands to expect that some materials actually perform better than reported. However, based on the published data it is difficult to judge if the resolution is limited by the scintillator or the photodetector. This was one of the motivations for the design of the setup presented in chapter 3 and **paper I**.

Some of these studies include a discussion of the stability, but unfortunately the metrics to quantify stability are diverse within the community, which makes comparisons difficult. In most studies the peak-height in the UV PL spectrum is taken as a measure for the stability, while only occasionally the X-ray PL or spatial resolution is monitored. Two types of stability can be distinguished: the storage stability in air and the stability under X-ray exposure (see table 5.1).

Unfortunately, the exact conditions of 'storage in air' (e.g., temperature, ambient humidity, light exposure) are rarely provided. In some cases, the storage stability has been investigated for several months mostly as a before-after experiment, and always without a continuous recording of the storage conditions.[140, 147, 148]

Similarly, the parameters of X-ray exposure (e.g., energy, dose, continuous/on-off-cycles) vary between the studies. The X-ray exposure times range from a couple of hours[148] to about 4 days,[149] with dose rates in the µGy/s to several mGy/s.

Besides comparing PL stability, it is important to monitor the resolution, since photo-aggregation can occur that might degrade the spatial resolution.[125] To the best of my knowledge our results in **paper V** are the first study on the resolution stability under X-ray exposure.

Accordingly, there is still a need for a stable high-resolution $CsPbBr_3$ scintillator, as well as an experimental setup that can monitor scintillator performance over long timescales.

material	spatial resolution (µm)	light yield (ph/MeV)	PL quantum yield (%)	detection limit (nGy/s)	UV/X-ray PL peak (nm)	air storage stability	UV/X-ray stability	decay time (ns)	Ref.
$CsPbBr_3$ NC in AAO	2.4	11100	83	33	UV: 522 X-ray: 530	> 42 days	-	9	146
$CsPbBr_3$@Cs_4PbBr_6	-	6000	60	-	UV: 520 X-ray: 518	4 months	UV: 4 h	3	140
$CsPbBr_3$ NC	51 (0.2MTF)	177000 (calculated)	-	-	UV: 550	-	X-ray: >40 Gy_{air}/s	2.87	15
$CsPbBr_3$ nanosheets	26	-	75.1 (external)	27	UV: 515	6 months in sealed petri dish: 21% of the PL QY	X-ray: 1 h (19 µGy/s)	5.03	148
$CsPbBr_3$ nanosheets	330	-	68	-	X-ray: 515-520	8 months in capped vial: 94% of the PL QY	-	5.6	150
$CsPbBr_3$ NC	250 (0.72MTF)	35676 [113]	-	13	X-ray: 530	-	X-ray: 120 on/off cycles over 4 days	44.6	149
$CsPbBr_3$ nanosheets	210	21000	63	-	UV: 515 X-ray: 520	-	X-ray: 2 h (18 µGy/s)	8.09	124
$CsPbBr_3$ NC with dye in PMMA	-	9000	75 +/- 8	-	UV: 518 X-ray: 620	6 months	X-ray: 1 h (800 Gy): 85% of PL	3.4	147
$CsPbBr_3$ nanosheets	8	21000	-	-	UV: 522	3 months (no data)	-	11.5	151
$CsPbBr_3$ single crystalline NWs in AAO	3.1 (0.1MTF)	5300 (corrected 19000)	-	-	UV: 530 X-ray: 535-540	2 months	X-ray: 2 weeks: above 85%[152]	7.3	paper IV & V[141, 152]

Table 5.1: Comparison of the performance and stability of some $CsPbBr_3$ NC scintillators.

5.3.2 Fabrication and Characterisation of $CsPbBr_3$ NW/AAO

The main idea of our approach is to directly grow the $CsPbBr_3$ NWs in a template which aligns them to the beam direction and thus provides an additional light guiding, a directed emission and a reduction of cross talk. This was expected to improve the spatial resolution like in scintillators based on micro-needles.[153, 154]

At the same time the template helps to protect most of the surface. The surface is the main interaction point of the scintillator with its environment, as well as the main location of defects. In nanostructures the surface area is large compared to the volume, therefore any surface treatment is expected to have a significant impact on the performance.

We used an AAO membrane as a template, which consist of a dense array of nano-sized pores, open at both ends, and grew single crystalline $CsPbBr_3$ NWs directly in the template from a drop of precursor solution. This differs from the reported fabrication method by Li et al. that also uses $CsPbBr_3$ and AAO but instead fills the pores with an assembly of QDs.[146] The single crystalline structure of our NWs was confirmed via X-ray diffraction and transmission electron microscopy (see **paper IV**).

The fabrication is simple (see fig. 5.4): a drop of precursor is deposited on a glass slide and covered with an AAO membrane. The precursor infuses into the pores via capillary forces and crystalises to NWs during the subsequent 30 min curing at 70°C. The NWs grow from the top surface of the membrane and are shorter than the membrane thickness (up to 9 µm NWs in 50 µm thick membranes).

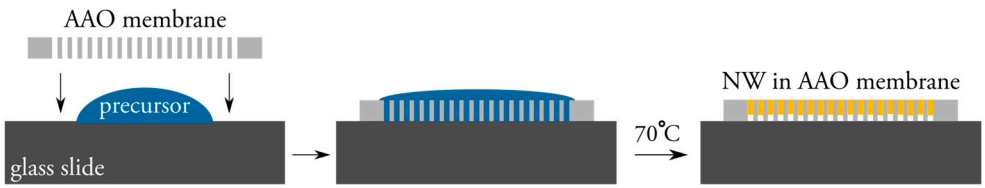

Figure 5.4: Fabrication process of $CsPbBr_3$ nanowires in an AAO membrane. First a drop of precursor deposited on a clean glass slide is covered with the AAO membrane. The precursor fills the pores via capillary forces and the sample is cured for 30 min at 70°C until all precursor has evaporated. Single crystalline nanowires fill the pores partially. Reprinted from **paper V** © Springer.[152]

As expected, we observed light guiding under UV illumination (see fig. 5.5c and **paper IV**), which helps to reduce the lateral scattering of scintillation light and decouple the scintillator thickness from the spatial resolution.[111]

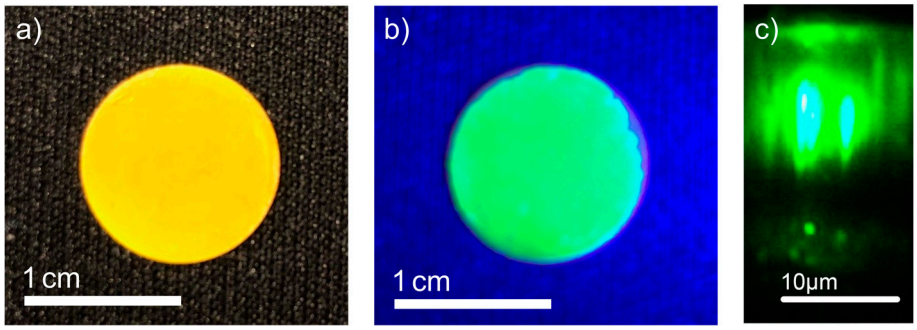

Figure 5.5: Photo of the NW/AAO scintillator. a) Visible light and b) UV illumination, membrane diameter about 1.3 cm. Note that the darker sections at the edge of the membrane in b) have not been filled with NWs and therefore show no UV luminescence. c) PL microscopy image of a cross-section, showing light guiding from the central excitation spot to the nanowire tips (excitation: 378 nm laser). Reprinted with permission from **paper IV** (ACS Appl. Nano Mater. 2022, 5, 1, 881–889. © 2022 American Chemical Society, https://doi.org/10.1021/acsanm.1c03575)

Moreover, we studied how the NW diameter and length influence the PL intensity and peak position. The intensity increases with NW length, which was expected since longer wires have a higher total absorption. The peak position showed a small red shift with increasing length, probably due to higher chances of self-absorption of the shorter wavelengths.

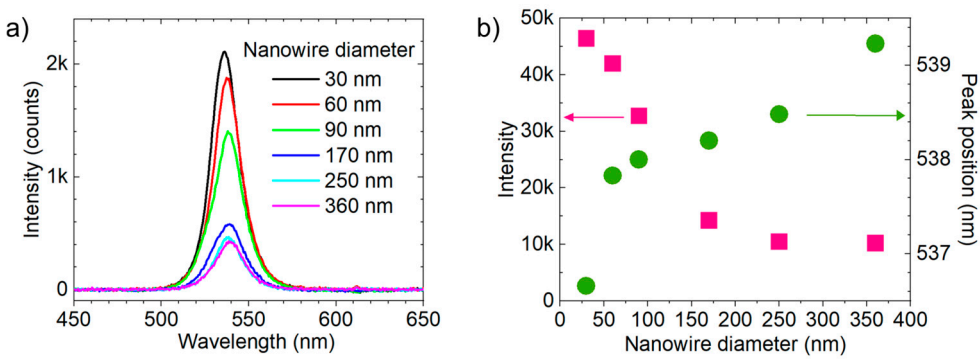

Figure 5.6: PL dependence on NW diameter. a) UV PL spectra of $CsPbBr_3$ NW/AAO scintillators with different NW diameters. b) Intensity and peak position over NW diameter. The peaks show a small blue shift as well as an increase of intensity with smaller diameter. Reprinted with permission from **paper IV** (ACS Appl. Nano Mater. 2022, 5, 1, 881–889. © 2022 American Chemical Society, https://doi.org/10.1021/acsanm.1c03575)

Surprisingly, the X-ray luminescence increased with decreasing NW diameter (see fig. 5.6). This was unexpected since the surface-to-volume ratio increases with thinner NWs, and most trap states are expected to be located on the surface. There are several possible reasons for this observation, as discussed in **paper IV**. Moreover, both UV and

X-ray PL peak have a small blue shift with decreasing diameter, which could be attributed to a larger strain and accordingly changed band structure in the NWs.

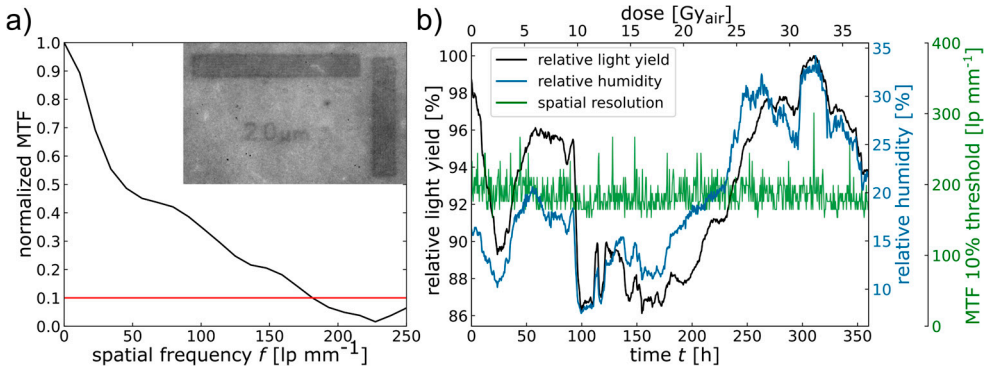

Figure 5.7: Resolution and stability of the scintillator. a) MTF of a $CsPbBr_3$ NW/AAO scintillator measured at our lab setup with the slanted edge method. The inset shows the 2 µm line pairs of a JIMA pattern. b) Stability under X-ray exposure measured over 2 weeks. The relative light yield fluctuated with the ambient humidity while the spatial resolution stayed stable. Note that the changes in brightness were small compared to the drastic changes in humidity. Reprinted from **paper V** © Springer.[152]

Both NW length and diameter showed no effect on the spatial resolution, which was measured to be about (180 ± 20) lp/mm (2.8 µm) using the slanted edge method, see fig. 5.7 (**paper V**).

Moreover, we studied the stability of the scintillator over 2 weeks under continuous low-dose X-ray exposure in our lab setup, monitoring both brightness and spatial resolution. We found a correlation of the brightness with air humidity while the resolution stayed unaffected, see fig. 5.7. Although the humidity in the lab changed drastically, at times dropping down to 20% of the peak value, the relative change in brightness was moderate, never falling under 85% of the peak value, which indicates a good stability compared to the state-of-the-art (see table 5.1). Interestingly the brightness increased with higher humidity levels (see **paper V**), which was unexpected since the opposite is usually reported for MHPs.[131] Moreover, we observed a predominantly reversible process, without clear indications of a long-term irreversible degradation.

These results made us confident that our scintillator was stable enough for acquiring a full tomogram, as will be discussed in the next section.

5.3.3 Tomography with a $CsPbBr_3$ NW/AAO Scintillator

Eventually, any scintillator that should be used for commercial X-ray detectors needs to be stable enough for tomography. Since a tomogram consists of several hundreds of

serial images, the stability requirements are more stringent than for 2D microscopy. The scintillator must be stable over long time periods of low dose (in lab setups), high doses rates (at synchrotron radiation sources) and have no significant afterglow (short decay times).

It is favourable if the scintillator is homogeneous over the whole FOV. This is not strictly necessary, since small inhomogeneities in brightness can be corrected for in the flat field correction of the images, but it is important that the resolution is not affected by the scintillator morphology. More important than homogeneity is that the brightness does not change locally during the measurement series. If some parts of the scintillator change differently than the rest the flat field correction will be incomplete and can cause artefacts (see chapter 2.3.2). For polychromatic setups it is also favourable if the scintillator response is insensitive to changes in the X-ray spectrum. Otherwise, the flat field correction for polychromatic radiation can be difficult, for example if beam hardening occurs (see chapter 2.3.2).

We have used the $CsPbBr_3$ NW/AAO scintillator in our laboratory setup (chapter 3) to acquire the first high resolution tomogram detected with an MHP material and a laboratory source (see fig. 5.8). The tomogram was taken in absorption contrast mode over 41 h, a relatively long period under which the scintillator showed only minor changes in brightness (< 5%), which were normalized during post-processing. No unexpected artefacts due to the scintillator could be identified and features in the range of a few micrometres diameter could be distinguished in the reconstruction (see fig. 5.8c and **paper V**).

Considering the stability issues of perovskites discussed in chapter 5.2, to the best of my knowledge this is the first tomogram recorded with a $CsPbBr_3$ scintillator in a lab µCT. There are currently only two other publications using MHP scintillators for tomography which I am aware of.

Zhou et al. used a $Cs_3Cu_2I_5$ film, a lead-free perovskite-like material that is currently studied as an alternative to lead halide perovskites. The tomogram showed a snail shell and had moderate resolution (visual estimation ~100 µm, no value or scale bar was given).[155] Although this is a promising result, our project aimed at developing a scintillator specifically for high resolution imaging, these results are therefore not directly relevant.

Very shortly after the publication of our **paper V**, Lü et al. also demonstrated tomography with a $CsPbBr_3$ scintillator.[151] Their publication was essentially simultaneous to ours, which shows the strong interest in this topic. The scintillator Lü et al. presented is based on self-assembling $CsPbBr_3$ nanosheets on a flexible membrane. They reported a slightly worse spatial resolution, but a higher light yield (21 000 ph/MeV) compared to our scintillator. In contrast to our lab measurements, they measured the tomogram at the Shanghai Synchrotron Radiation Facility. This entails

a much shorter acquisition time (90 min) due to the higher flux, but probably comparable integrated dose (no values given). Although they mention repeated measurements over a 3 months' period, they do not provide any data quantifying their stability or degradation. No long-term X-ray exposure was reported.

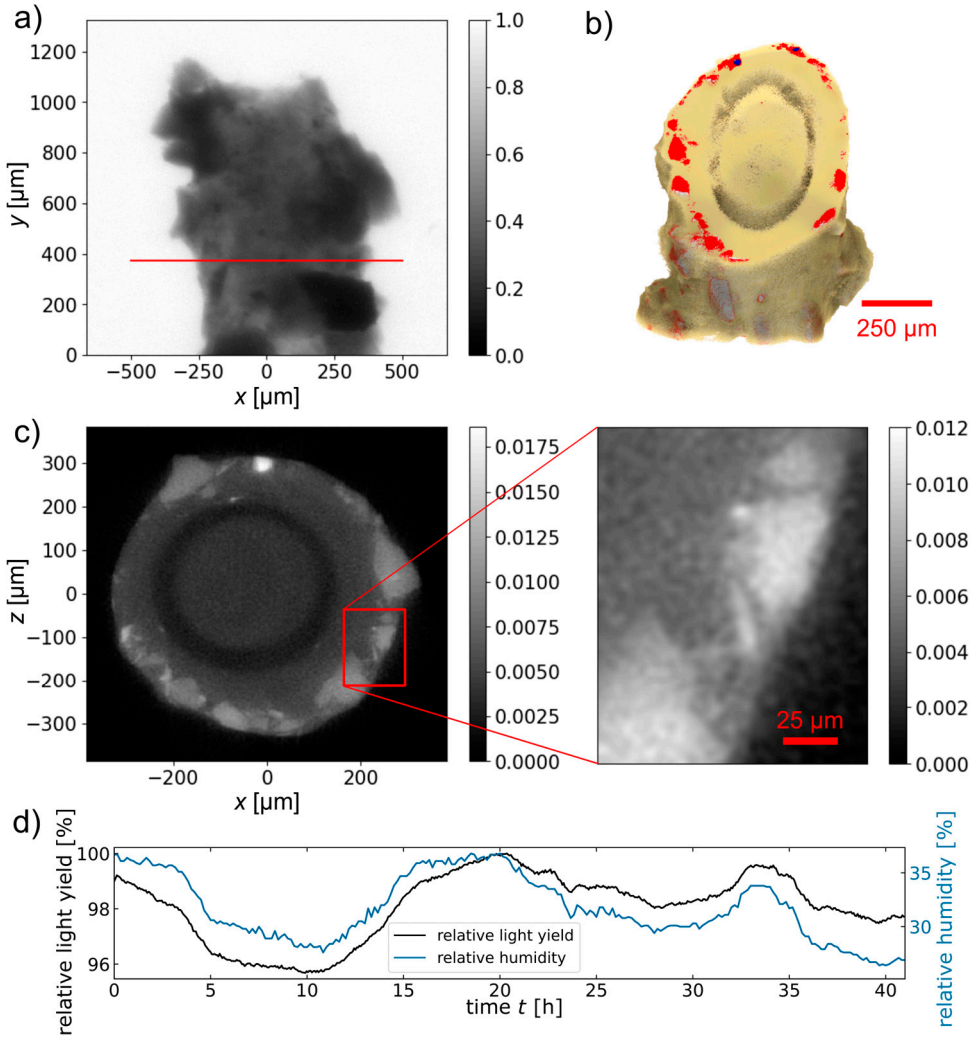

Figure 5.8: Tomogram of grains of crushed granite from the Siljan meteorite impact site acquired with a $CsPbBr_3$ NW/AAO scintillator. a) Projection image after flat field correction b) 3D representation of the tomogram segmented into rock (red) and mounting glue. c) Slice through the volume in a) showing grains of about 10 µm diameter. d) Relative light yield and humidity over time during the tomography acquisition. The light yield reacted to the humidity level, but only changed in a 5%-range even though the humidity values temporarily dropped to about half of the peak value. Reprinted from **paper V** © Springer.[152]

In comparison to these publications our scintillator had a similar or better performance in terms of spatial resolution and stability. Moreover, we showed the correlation of light yield and resolution with air humidity during continuous X-ray exposure, which has not been shown before. Importantly, even though the scintillator reacted to the ambient humidity, the response was weak considering the strong fluctuations. The resolution was stable over the whole measurement series and no clear overall degradation trend due to the X-rays could be identified. Accordingly, even though additional protection of the NWs might improve the performance, our scintillator is already very stable compared to the state-of-the-art (see table 5.1).

5.3.4 Outlook

As demonstrated above, MHPs have the potential to become a new generation of X-ray scintillators that combine good spatial resolution and low fabrication costs. The main challenge for commercialization, the stability, can be mitigated by in-template growth. Using a structured template gives the additional advantage of a light-guiding effect, which helps to decouple spatial resolution from scintillator thickness.

The next step would be to develop a coating to protect the remaining surface area of the NWs. Moreover, systematic studies to gain better understanding of the degradation processes of the scintillator under both X-ray and humidity exposure, including a decoupling of the two, would help to improve the protection strategies. A first step would be to follow the PL signal while cycling through humidity levels under a controlled atmosphere, with and without X-rays. Moreover, different analysis methods, for example X-ray diffraction to map the changes in crystal structure and strain in the NWs under different humidity levels or near-edge X-ray absorption spectroscopy to follow chemical changes, would help understanding the underlying processes.

In terms of fabrication, the growth of the NWs itself can be improved aiming for more control over the process, for example by controlling the gaseous environment during growths. Ultimately, the goal is to further increase the light yield by having longer and thinner nanowires and a homogeneous filling of all pores. Moreover, the scintillator should become even flatter to match the small focal depth of the visible light objective. Currently the small surface curvature is most likely due to strain induced into the template during growth. A more controlled growth process and homogeneous filling will hopefully reduce this effect.

6 Conclusion and Outlook

In this thesis I have demonstrated the development of a laboratory X-ray μCT setup with PB-PCI modality, which is suitable for applications but also for methodological studies in X-ray physics and material science.

Complimentary to the technical improvements for my setup and the next steps in MHP scintillator development that were already discussed in chapter 3.2.3 and 5.3.4, respectively, I here want to give a more general and personal outlook on laboratory X-ray microscopy itself.

I expect that some of the mentioned source and detector technologies like nano-focus sources and photon counting detectors that are currently still new and expensive will soon become a standard in labs, routinely providing sub-micron resolution. Traditionally higher resolution comes at the price of a smaller FOV, which often is not sufficient for the sample size or research question. Therefore, we can already see an increasing interest to overcome this limitation, for example via stitching of sub-images/volumes or a combination of different magnifications (zoom tomography) to access a hierarchical understanding of the sample. Laboratory based setups can here be a great complimentary tool to synchrotron radiation measurements and other imaging methods such as electron microscopy.[156-159]

Already now dynamic, time-resolved tomography studies, relying on a series of fast scans are possible, predominantly at synchrotron radiation sources.[4, 160, 161] Thanks to more brilliant X-ray tubes and high-sensitivity detectors I expect them to soon become more common in laboratory setting, too. This will allow to follow complex processes in biology (such as breathing, muscle contractions, germination) and material science (such as mechanical load, battery degradation, crack formation) in real time and 3D.

Phase-contrast methods are already part of most recently built setups, especially experimentally simple approaches such as PB-PCI or mask-based techniques. Their potential is widely recognized, and I expect that phase contrast imaging will soon become common even in clinical applications.[162] Advances in computational phase retrieval will eventually overcome many of the issues that still exist, such as multi-material samples, polychromatic effects, instable illumination, and artefacts due to geometry or motion. Efforts to implement phase retrieval and post-processing algorithms in toolboxes, such as PyPhase[163] or HoloTomo[164], are already made, which

greatly facilitates the data analysis even for non-expert users. Moreover, more approaches will undoubtedly include artificial intelligence.[165]

Besides phase retrieval, image analysis itself is a thriving research field with applications in many different sectors of science and society. Many innovations developed for non-scientific applications, such as segmentation, classification and rendering for virtual reality or self-driving cars, already have substantial value for today's research. In my opinion the bottleneck is here not the availability of suitable algorithms, but rather the knowledge transfer between computer scientists and physicists.

Besides technological solutions following the advances in physics, computer science or engineering, I also believe that X-ray microscopy would benefit from being developed in even closer cooperation with the 'application disciplines' that provide the samples, such as medicine, biology, material science or archaeology. Microscopy is often more of a tool, than a research question itself, which I do not see as a drawback but rather as a chance to inspire 'innovation by demand'. However, this could mean that it is not always the technologically most advanced setups that are needed, but rather *suitable* setups. This sometimes conflicts with the idea that significant research needs to push towards the limits of what is possible. Instead, I think that the tool needs to match the task, which could be a specific sample environment, dose rate, statistics, stability, resolution or simply availability. Knowing what is needed requires effective communication, across disciplines, which comes with its own challenges. Still, I believe it is worth the effort to start this dialogue early, especially in instrumentation projects, since even the best setup might stand idle if no applications can be found that matches its capabilities or the data cannot be analysed without an expert user.

References

1. Hounsfield, G. N., Computerized transverse axial scanning (tomography): Part 1. Description of system. *The British Journal of Radiology* **1973,** *46* (552), 1016-1022.
2. Rankin, K. E.; Hazell, Z. J.; Middleton, A. M.; Mavrogordato, M. N., Micro-focus X-ray CT scanning of two rare wooden objects from the wreck of the London, and its application in heritage science and conservation. *Journal of Archaeological Science: Reports* **2021,** *39*.
3. Romell, J.; Vagberg, W.; Romell, M.; Haggman, S.; Ikram, S.; Hertz, H. M., Soft-Tissue Imaging in a Human Mummy: Propagation-based Phase-Contrast CT. *Radiology* **2018,** *289* (3), 670-676.
4. Taiwo, O. O.; Paz-García, J. M.; Hall, S. A.; Heenan, T. M. M.; Finegan, D. P.; Mokso, R.; Villanueva-Pérez, P.; Patera, A.; Brett, D. J. L.; Shearing, P. R., Microstructural degradation of silicon electrodes during lithiation observed via operando X-ray tomographic imaging. *Journal of Power Sources* **2017,** *342*, 904-912.
5. Mayo, S. C.; Stevenson, A. W.; Wilkins, S. W., In-Line Phase-Contrast X-ray Imaging and Tomography for Materials Science. *Materials (Basel)* **2012,** *5* (5), 937-965.
6. Eckermann, M.; van der Meer, F.; Cloetens, P.; Ruhwedel, T.; Möbius, W.; Stadelmann, C.; Salditt, T., Three-dimensional virtual histology of the cerebral cortex based on phase-contrast X-ray tomography. *Biomed. Opt. Express* **2021,** *12* (12), 7582-7598.
7. Le Cann, S.; Tudisco, E.; Tagil, M.; Hall, S. A.; Isaksson, H., Bone Damage Evolution Around Integrated Metal Screws Using X-Ray Tomography - in situ Pullout and Digital Volume Correlation. *Front Bioeng Biotechnol* **2020,** *8*, 934.
8. Peruzzi, N.; Veress, B.; Dahlin, L. B.; Salditt, T.; Andersson, M.; Eckermann, M.; Frohn, J.; Robisch, A.-L.; Bech, M.; Ohlsson, B., 3D analysis of the myenteric plexus of the human bowel by X-ray phase-contrast tomography – a future method? *Scandinavian Journal of Gastroenterology* **2020,** *55* (10), 1261-1267.
9. Dreier, T.; Bernström, G.; Ganji, S.; Norvik, C.; Tran-Lundmark, K.; Bech, M. In *Radiopaque dyes allow vessel imaging in lung tissue using laboratory phase contrast micro-CT*, SPIE Optical Engineering + Applications, SPIE: 2022.
10. De Chiffre, L.; Carmignato, S.; Kruth, J. P.; Schmitt, R.; Weckenmann, A., Industrial applications of computed tomography. *CIRP Annals* **2014,** *63* (2), 655-677.

11. Erb, A.; Turner, A. H., Braincase anatomy of the Paleocene crocodyliform Rhabdognathus revealed through high resolution computed tomography. *PeerJ* **2021,** *9*.
12. Fella, C.; Dittmann, J.; Muller, D.; Donath, T.; Murer, D.; Tuohimaa, T.; Sofiienko, A.; Zabler, S.; Hanke, R., Implementation of a Computed Tomography System based on a laboratory-based nanofocus X-ray source. *Microscopy and Microanalysis* **2018,** *24* (S2), 236-237.
13. Pollock, H. C., The discovery of synchrotron radiation. *American Journal of Physics* **1983,** *51* (3), 278-280.
14. Wilkins, S. W. G., T. E.; Gao, D.; Pogany, A.; Stevenson, A. W., Phase-contrast imaging using polychromatic hard X-rays. *Nature* **1996,** *384* (6607), 335-338.
15. Heo, J. H.; Shin, D. H.; Park, J. K.; Kim, D. H.; Lee, S. J.; Im, S. H., High-Performance Next-Generation Perovskite Nanocrystal Scintillator for Nondestructive X-Ray Imaging. *Adv Mater* **2018**, e1801743.
16. Jens Als-Nielsen; McMorrow, D., X-rays and their interaction with matter. In *Elements of Modern X-ray Physics*, 2011; pp 1-28.
17. Paganin, D., *Coherent X-Ray Optics*. Oxford University: 2006.
18. Saleh, B. E.; Teich, M. C., *Fundamentals of photonics*. john Wiley & sons: 2019.
19. Born, M.; Wolf, E., *Principles of optics: electromagnetic theory of propagation, interference and diffraction of light*. Elsevier: 2013.
20. Berger, M. J.; Hubbell, J. H.; Seltzer, S. M.; Chang, J.; Coursey, J. S.; Sukumar, R.; Zucker, D. S.; Olsen, K., XCOM: Photon Cross Sections Database (version 1.5). National Institute of Standards and Technology: Gaithersburg, MD., 2010.
21. Henke, B. L.; Gullikson, E. M.; Davis, J. C., X-Ray Interactions: Photoabsorption, Scattering, Transmission, and Reflection at E = 50-30,000 eV, Z = 1-92. *Atomic Data and Nuclear Data Tables* **1993,** *54* (2), 181-342.
22. Peli, E., Contrast in complex images. *Journal of the Optical Society of America A* **1990,** *7* (10), 2032-2040.
23. Eisebitt, S.; Lüning, J.; Schlotter, W. F.; Lörgen, M.; Hellwig, O.; Eberhardt, W.; Stöhr, J., Lensless imaging of magnetic nanostructures by X-ray spectro-holography. *Nature* **2004,** *432* (7019), 885-888.
24. Beckhoff, B.; Kanngießer, B.; Langhoff, N.; Wedell, R.; Wolff, H., *Handbook of practical X-ray fluorescence analysis*. Springer Science & Business Media: 2007.
25. Abbe, E., Beiträge zur Theorie des Mikroskops und der mikroskopischen Wahrnehmung. *Archiv für mikroskopische Anatomie* **1873,** *9* (1), 413-468.
26. Rayleigh, XXXI. Investigations in optics, with special reference to the spectroscope. *The London, Edinburgh, and Dublin Philosophical Magazine and Journal of Science* **1879,** *8* (49), 261-274.
27. Shannon, C. E., Communication in the Presence of Noise. *Proceedings of the IRE* **1949,** *37* (1), 10-21.

28. van Heel, M.; Schatz, M., Fourier shell correlation threshold criteria. *J Struct Biol* **2005,** *151* (3), 250-62.
29. Buhr, E.; Gunther-Kohfahl, S.; Neitzel, U., Accuracy of a simple method for deriving the presampled modulation transfer function of a digital radiographic system from an edge image. *Med Phys* **2003,** *30* (9), 2323-31.
30. Van Heel, M.; Keegstra, W.; Schutter, W.; Van Bruggen, E., Arthropod hemocyanin structures studied by image analysis. *Life Chem. Rep. Suppl* **1982,** *1* (69-73), 5.
31. Saxton, W. O.; Baumeister, W., The correlation averaging of a regularly arranged bacterial cell envelope protein. *Journal of Microscopy* **1982,** *127* (2), 127-138.
32. Van Heel, M., Similarity measures between images. *Ultramicroscopy* **1987,** *21* (1), 95-100.
33. Webb, S., *From the Watching of Shadows: The Origins of Radiological Tomography*. 1990.
34. Buzug, T. M., *Computed Tomography*. Springer-Verlag: 2008.
35. Gordon, R.; Bender, R.; Herman, G. T., Algebraic reconstruction techniques (ART) for three-dimensional electron microscopy and x-ray photography. *J Theor Biol* **1970,** *29* (3), 471-81.
36. Andersen, A. H.; Kak, A. C., Simultaneous Algebraic Reconstruction Technique (SART): A superior implementation of the ART algorithm. *Ultrasonic Imaging* **1984,** *6* (1), 81-94.
37. Debasish Mishra, K. M. P. M., A robust MART algorithm for tomographic applications. *Numerical Heat Transfer, Part B: Fundamentals* **1999,** *35* (4), 485-506.
38. Crowther, R. A.; DeRosier, D. J.; Klug, A., The reconstruction of a three-dimensional structure from projections and its application to electron microscopy. *Proceedings of the Royal Society of London. A. Mathematical and Physical Sciences* **1970,** *317* (1530), 319-340.
39. Feldkamp, L. A.; Davis, L. C.; Kress, J. W., Practical cone-beam algorithm. *Journal of the Optical Society of America A* **1984,** *1* (6), 612-619.
40. Töpperwien, M.; Krenkel, M.; Müller, K.; Salditt, T.; Stock, S. R.; Müller, B.; Wang, G. In *Phase-contrast tomography of neuronal tissues: from laboratory- to high resolution synchrotron CT*, Proc.SPIE, 2016; p 99670T.
41. Münch, B.; Trtik, P.; Marone, F.; Stampanoni, M., Stripe and ring artifact removal with combined wavelet — Fourier filtering. *Opt. Express* **2009,** *17* (10), 8567-8591.
42. Miqueles, E. X.; Rinkel, J.; O'Dowd, F.; Bermudez, J. S., Generalized Titarenko's algorithm for ring artefacts reduction. *J Synchrotron Radiat* **2014,** *21* (Pt 6), 1333-46.
43. Mouton, A.; Megherbi, N.; Van Slambrouck, K.; Nuyts, J.; Breckon, T. P., An experimental survey of metal artefact reduction in computed tomography. *Journal of X-Ray Science and Technology* **2013,** *21*, 193-226.

44. Zefreh, K. Z. In *Afterglow artifacts correction for ultra-fast tomography acquisition by synchrotron radiation*, 2016 IEEE Nuclear Science Symposium, Medical Imaging Conference and Room-Temperature Semiconductor Detector Workshop (NSS/MIC/RTSD), 29 Oct.-6 Nov. 2016; 2016; pp 1-4.
45. Adibhatla, A.; Espes, E., *MetalJet X-ray tube for high speed CT (Conference Presentation)*. SPIE: 2022; Vol. PC12240.
46. Flohr, T.; Petersilka, M.; Henning, A.; Ulzheimer, S.; Ferda, J.; Schmidt, B., Photon-counting CT review. *Physica Medica* **2020,** *79*, 126-136.
47. Brombal, L.; Kallon, G.; Jiang, J.; Savvidis, S.; De Coppi, P.; Urbani, L.; Forty, E. J.; Chambers, R. C.; Longo, R.; Olivo, A.; Endrizzi, M., Monochromatic Propagation-Based Phase-Contrast Microscale Computed-Tomography System with a Rotating-Anode Source. *Physical Review Applied* **2019,** *11* (3).
48. Eckermann, M.; Topperwien, M.; Robisch, A. L.; van der Meer, F.; Stadelmann, C.; Salditt, T., Phase-contrast x-ray tomography of neuronal tissue at laboratory sources with submicron resolution. *J Med Imaging (Bellingham)* **2020,** *7* (1), 013502.
49. Dierks, H.; Stjärneblad, P.; Wallentin, J., A versatile laboratory setup for high resolution X-ray phase contrast tomography and scintillator characterization. *Journal of X-Ray Science and Technology* **2023,** *31*, 1-12.
50. Töpperwien, M. 3d virtual histology of neuronal tissue by propagation-based x-ray phase-contrast tomography. Georg-August-Universität Göttingen, 2018.
51. Kitchen, M. J.; Buckley, G. A.; Gureyev, T. E.; Wallace, M. J.; Andres-Thio, N.; Uesugi, K.; Yagi, N.; Hooper, S. B., CT dose reduction factors in the thousands using X-ray phase contrast. *Sci Rep* **2017,** *7* (1), 15953.
52. Snigirev, A.; Snigireva, I.; Kohn, V.; Kuznetsov, S.; Schelokov, I., On the possibilities of x-ray phase contrast microimaging by coherent high-energy synchrotron radiation. *Review of Scientific Instruments* **1995,** *66* (12), 5486-5492.
53. Zernike, F., Phase contrast, a new method for the microscopic observation of transparent objects. *Physica* **1942,** *9* (7), 686-698.
54. Tochigi, H.; Nakatsuka, H.; Fukami, A.; Kanaya, K., The improvement of the image contrast by using the phase plate in the TEM. *Microscopie Electronique* **1970,** *1*, 73.
55. Bonse, U.; Hart, M., AN X-RAY INTERFEROMETER. *Applied Physics Letters* **1965,** *6* (8), 155-156.
56. Kunz, C., Synchrotron radiation: third generation sources. *Journal of Physics: Condensed Matter* **2001,** *13* (34), 7499.
57. Bravin, A.; Coan, P.; Suortti, P., X-ray phase-contrast imaging: from pre-clinical applications towards clinics. *Physics in Medicine & Biology* **2013,** *58* (1), R1.

58. Massimi, L.; Bukreeva, I.; Santamaria, G.; Fratini, M.; Corbelli, A.; Brun, F.; Fumagalli, S.; Maugeri, L.; Pacureanu, A.; Cloetens, P.; Pieroni, N.; Fiordaliso, F.; Forloni, G.; Uccelli, A.; Kerlero de Rosbo, N.; Balducci, C.; Cedola, A., Exploring Alzheimer's disease mouse brain through X-ray phase contrast tomography: From the cell to the organ. *Neuroimage* **2019,** *184*, 490-495.

59. Pfeiffer, F.; Herzen, J.; Willner, M.; Chabior, M.; Auweter, S.; Reiser, M.; Bamberg, F., Grating-based X-ray phase contrast for biomedical imaging applications. *Zeitschrift für Medizinische Physik* **2013,** *23* (3), 176-185.

60. Cloetens, P.; Pateyron-Salomé, M.; Buffière, J. Y.; Peix, G.; Baruchel, J.; Peyrin, F.; Schlenker, M., Observation of microstructure and damage in materials by phase sensitive radiography and tomography. *Journal of Applied Physics* **1997,** *81* (9), 5878-5886.

61. Weitkamp, T.; Nöhammer, B.; Diaz, A.; David, C.; Ziegler, E., X-ray wavefront analysis and optics characterization with a grating interferometer. *Applied Physics Letters* **2005,** *86* (5), 054101.

62. Kayser, Y.; David, C.; Flechsig, U.; Krempasky, J.; Schlott, V.; Abela, R., X-ray grating interferometer for in situ and at-wavelength wavefront metrology. *Journal of Synchrotron Radiation* **2017,** *24* (1), 150-162.

63. Endrizzi, M., X-ray phase-contrast imaging. *Nuclear Instruments and Methods in Physics Research Section A: Accelerators, Spectrometers, Detectors and Associated Equipment* **2018,** *878*, 88-98.

64. Kalbfleisch, S.; Zhang, Y.; Kahnt, M.; Buakor, K.; Langer, M.; Dreier, T.; Dierks, H.; Stjarneblad, P.; Larsson, E.; Gordeyeva, K.; Chayanun, L.; Soderberg, D.; Wallentin, J.; Bech, M.; Villanueva-Perez, P., X-ray in-line holography and holotomography at the NanoMAX beamline. *J Synchrotron Radiat* **2022,** *29* (Pt 1), 224-229.

65. Miao, J.; Sandberg, R. L.; Song, C., Coherent X-Ray Diffraction Imaging. *IEEE Journal of Selected Topics in Quantum Electronics* **2012,** *18* (1), 399-410.

66. Pfeiffer, F., X-ray ptychography. *Nature Photonics* **2018,** *12* (1), 9-17.

67. Momose, A.; Kawamoto, S.; Koyama, I.; Hamaishi, Y.; Takai, K.; Suzuki, Y., Demonstration of X-Ray Talbot Interferometry. *Japanese Journal of Applied Physics* **2003,** *42* (Part 2, No. 7B), L866-L868.

68. Weitkamp, T.; Diaz, A.; David, C.; Pfeiffer, F.; Stampanoni, M.; Cloetens, P.; Ziegler, E., X-ray phase imaging with a grating interferometer. *Opt. Express* **2005,** *13* (16), 6296-6304.

69. Momose, A.; Yashiro, W.; Takeda, Y.; Suzuki, Y.; Hattori, T., Phase Tomography by X-ray Talbot Interferometry for Biological Imaging. *Jpn. J. Appl. Phys.* **2006,** *45* (6A), 5254.

70. Pfeiffer, F.; Weitkamp, T.; Bunk, O.; David, C., Phase retrieval and differential phase-contrast imaging with low-brilliance X-ray sources. *Nat. Phys.* **2006,** *2*, 258–261.

71. Olivo, A.; Ignatyev, K.; Munro, P. R. T.; Speller, R. D., Noninterferometric phase-contrast images obtained with incoherent x-ray sources. *Applied Optics* **2011,** *50* (12), 1765-1769.

72. Olivo, A., Edge-illumination x-ray phase-contrast imaging. *J. Phys.: Condens. Matter* **2021,** *33* (363002).

73. Zdora, M.-C., State of the Art of X-ray Speckle-Based Phase-Contrast and Dark-Field Imaging. *Journal of Imaging* **2018,** *4* (5).

74. Zanette, I.; Zhou, T.; Burvall, A.; Lundström, U.; Larsson, D. H.; Zdora, M.; Thibault, P.; Pfeiffer, F.; Hertz, H. M., Speckle-Based X-Ray Phase-Contrast and Dark-Field Imaging with a Laboratory Source. *Physical Review Letters* **2014,** *112* (25), 253903.

75. Morgan, K. S.; Paganin, D. M.; Siu, K. K. W., X-ray phase imaging with a paper analyzer. *Applied Physics Letters* **2012,** *100* (12), 124102.

76. Berujon, S.; Wang, H.; Sawhney, K., X-ray multimodal imaging using a random-phase object. *Physical Review A* **2012,** *86* (6), 063813.

77. Arhatari, B. D.; Hannah, K.; Balaur, E.; Peele, A. G., Phase Imaging Using A Polychromatic X-ray Laboratory Source. *Opt. Express* **2008,** *16*, 19950-19956.

78. Gureyev, T. E.; Mayo, S. C.; Myers, D. E.; Nesterets, Y.; Paganin, D. M.; Pogany, A.; Stevenson, A. W.; Wilkins, S. W., Refracting Röntgen's rays: Propagation-based x-ray phase contrast for biomedical imaging. *J. Appl. Phys.* **2009,** *105* (10), 102005.

79. Pogany, A.; Gao, D.; Wilkins, S. W., Contrast and resolution in imaging with a microfocus x-ray source. *Rev. Sci. Instrum.* **1997,** *68* (7), 2774-2782.

80. Teague, M. R., Image formation in terms of the transport equation. *Journal of the Optical Society of America A* **1985,** *2* (11), 2019-2026.

81. Burvall, A.; Lundström, U.; Takman, P. A. C.; Larsson, D. H.; Hertz, H. M., Phase retrieval in X-ray phase-contrast imaging suitable for tomography. *Opt. Express* **2011,** *19* (11), 10359-10376.

82. Nugent, K. A., X-ray noninterferometric phase imaging: a unified picture. *J. Opt. Soc. Am. A* **2007,** *24*.

83. Pogany, A.; Gao, D.; Wilkins, S. W., Contrast and resolution in imaging with a microfocus x-ray source. *Review of Scientific Instruments* **1997,** *68* (7), 2774-2782.

84. Hehn, L.; Gradl, R.; Dierolf, M.; Morgan, K. S.; Paganin, D. M.; Pfeiffer, F., Model-Based Iterative Reconstruction for Propagation-Based Phase-Contrast X-Ray CT including Models for the Source and the Detector. *IEEE Trans Med Imaging* **2020,** *39* (6), 1975-1987.

85. K. A. Mohan; D. Parkinson; Cuadra, J. A., Constrained Non-Linear Phase Retrieval for Single Distance X-ray Phase Contrast Tomography. **2020**.

86. Yan, A.; Wu, X.; Liu, H., An attenuation-partition based iterative phase retrieval algorithm for in-line phase-contrast imaging. **2008**.

87. Cloetens, P.; Ludwig, W.; Baruchel, J.; Dyck, D. V.; Landuyt, J. V.; Guigay, J. P.; Schlenker, M., Holotomography: Quantitative phase tomography with micrometer resolution using hard synchrotron radiation x rays. *Applied Physics Letters* **1999,** *75* (19), 2912-2914.

88. Yu, B.; Weber, L.; Pacureanu, A.; Langer, M.; Olivier, C.; Cloetens, P.; Peyrin, F., Evaluation of phase retrieval approaches in magnified X-ray phase nano computerized tomography applied to bone tissue. *Opt Express* **2018,** *26* (9), 11110-11124.

89. Paganin, D.; Mayo, S. C.; Gureyev, T. E.; Miller, P. R.; Wilkins, S. W., Simultaneous phase and amplitude extraction from a single defocused image of a homogeneous object. *J. Microsc.* **2002,** *206*, 33.

90. Paganin, D. M.; Favre-Nicolin, V.; Mirone, A.; Rack, A.; Villanova, J.; Olbinado, M. P.; Fernandez, V.; da Silva, J. C.; Pelliccia, D., Boosting spatial resolution by incorporating periodic boundary conditions into single-distance hard-x-ray phase retrieval. *Journal of Optics* **2020,** *22* (11), 115607.

91. Beltran, M., 2D and 3D X-ray phase retrieval of multi-material objects using a single defocus distance. **2010**.

92. Häggmark, I.; Vågberg, W.; Hertz, H. M.; Burvall, A., Comparison of quantitative multi-material phase-retrieval algorithms in propagation-based phase-contrast X-ray tomography. *Opt. Express* **2017,** *25* (26), 33543.

93. Bronnikov, A. V., Reconstruction formulas in phase-contrast tomography. **1999**.

94. Bronnikov, A. V., Theory of quantitative phase-contrast computed tomography. *J. Opt. Soc. Am.* **2002,** *19* (3).

95. Ruhlandt, A.; Krenkel, M.; Bartels, M.; Salditt, T., Three-dimensional phase retrieval in propagation-based phase-contrast imaging. *Physical Review A* **2014,** *89* (3).

96. Brun, F.; Brombal, L.; Di Trapani, V.; Delogu, P.; Donato, S.; Dreossi, D.; Rigon, L.; Longo, R., Post-reconstruction 3D single-distance phase retrieval for multi-stage phase-contrast tomography with photon-counting detectors. *J Synchrotron Radiat* **2019,** *26* (Pt 2), 510-516.

97. Thompson, D. A.; Nesterets, Y. I.; Pavlov, K. M.; Gureyev, T. E., Fast three-dimensional phase retrieval in propagation-based X-ray tomography. *J Synchrotron Radiat* **2019,** *26* (Pt 3), 825-838.

98. Gureyev, T. E., On x-ray phase imaging with a point source. **1998**.

99. Gureyev, T. E.; Wilkins, S. W., On X-ray phase retrieval from polychromatic images. *Optics Communications* **1998,** *147* (4), 229-232.

100. Gureyev, T. E.; Nesterets, Y. I.; Stevenson, A. W.; Miller, P. R.; Pogany, A.; Wilkins, S. W., Some simple rules for contrast, signal-to-noise and resolution in in-line x-ray phase-contrast imaging. *Opt. Express* **2008,** *16* (5), 3223-3241.

101. Nesterets, Y. I.; Gureyev, T. E.; Dimmock, M. R., Optimisation of a propagation-based x-ray phase-contrast micro-CT system. *J. Phys. D: Appl. Phys.* **2018,** *51* (11), 115402.

102. Nesterets, Y. I.; Wilkins, S. W.; Gureyev, T. E.; Pogany, A.; Stevenson, A. W., On the optimization of experimental parameters for x-ray in-line phase-contrast imaging. *Rev. Sci. Instrum.* **2005,** *76* (9), 093706.

103. Gureyev, T. E.; Mayo, S.; Wilkins, S. W.; Paganin, D.; Stevenson, A. W., Quantitative In-Line Phase-Contrast Imaging with Multienergy X Rays. *Physical Review Letters* **2001,** *86* (25), 5827-5830.

104. Donnelly, E. F.; Price, R. R.; Pickens, D. R., Quantification of the effect of system and object parameters on edge enhancement in phase-contrast radiography. *Med Phys* **2003,** *30* (11), 2888-96.

105. Gui, J.; Zou, J.; Rong, J.; Hu, Z.; Zhang, Q.; Zheng, H.; Xia, D., Investigation of the effect of tube voltage and imaging geometry on phase contrast imaging for a micro-CT system. *Nuclear Instruments and Methods in Physics Research Section A: Accelerators, Spectrometers, Detectors and Associated Equipment* **2012,** *669*, 97-102.

106. Bidola, P. M.; Zanette, I.; Achterhold, K.; Holzner, C.; Pfeiffer, F., Optimization of propagation-based phase-contrast imaging at a laboratory setup. *Opt. Express* **2015,** *23* (23), 30000-30013.

107. Cheng, J.; Cao, Y.; Yang, Q.; Qi, S.; Ye, Y.; Qian, W.; Liu, D.; Meng, L.; Zhu, P.; Li, J., The influence of spectrum and imaging geometry on propagation-based phase-contrast imaging for micro-focus source. *Optik* **2016,** *127* (6), 3286-3291.

108. Dierks, H.; Wallentin, J., Experimental optimization of X-ray propagation-based phase contrast imaging geometry. *Opt Express* **2020,** *28* (20), 29562-29575.

109. Olivo, A.; Speller, R., Polychromatic phase contrast imaging as a basic step towards a widespread application of the technique. *Nuclear Instruments and Methods in Physics Research Section A: Accelerators, Spectrometers, Detectors and Associated Equipment* **2007,** *580* (2), 1079-1082.

110. Nüsslin, F., Wilhelm Conrad Röntgen: The scientist and his discovery. *Physica Medica* **2020,** *79*, 65-68.

111. Nikl, M., Scintillation detectors for x-rays. *Measurement Science and Technology* **2006,** *17* (4), R37-R54.

112. Kumar, V.; Luo, Z., A Review on X-ray Excited Emission Decay Dynamics in Inorganic Scintillator Materials. *Photonics* **2021,** *8* (3).

113. Wu, H.; Ge, Y.; Niu, G.; Tang, J., Metal Halide Perovskites for X-Ray Detection and Imaging. *Matter* **2021,** *4* (1), 144-163.

114. Alig, R. C.; Bloom, S., Electron-Hole-Pair Creation Energies in Semiconductors. *Physical Review Letters* **1975,** *35* (22), 1522-1525.

115. Jana, A.; Cho, S.; Patil, S. A.; Meena, A.; Jo, Y.; Sree, V. G.; Park, Y.; Kim, H.; Im, H.; Taylor, R. A., Perovskite: Scintillators, direct detectors, and X-ray imagers. *Materials Today* **2022,** *55*, 110-136.

116. Lempicki, A.; Wojtowicz, A. J.; Berman, E., Fundamental limits of scintillator performance. *Nuclear Instruments and Methods in Physics Research Section A: Accelerators, Spectrometers, Detectors and Associated Equipment* **1993,** *333* (2), 304-311.

117. Zhao, W.; Ristic, G.; Rowlands, J. A., X-ray imaging performance of structured cesium iodide scintillators. *Medical Physics* **2004,** *31* (9), 2594-2605.

118. Ghasemi, M.; Yuan, S.; Fan, J.; Jia, B.; Wen, X., The Challenges Toward the Development of Metal-Halide Perovskite Single Crystal Solar Cells. *Journal of Materials Chemistry A* **2023**.

119. Dong, H.; Ran, C.; Gao, W.; Li, M.; Xia, Y.; Huang, W., Metal Halide Perovskite for next-generation optoelectronics: progresses and prospects. *eLight* **2023,** *3* (1), 3.

120. Zhou, Y.; Chen, J.; Bakr, O. M.; Mohammed, O. F., Metal Halide Perovskites for X-ray Imaging Scintillators and Detectors. *ACS Energy Letters* **2021,** *6* (2), 739-768.

121. Mykhaylyk, V. B.; Kraus, H.; Kapustianyk, V.; Kim, H. J.; Mercere, P.; Rudko, M.; Da Silva, P.; Antonyak, O.; Dendebera, M., Bright and fast scintillations of an inorganic halide perovskite CsPbBr3 crystal at cryogenic temperatures. *Scientific Reports* **2020,** *10* (1), 8601.

122. Xie, A.; Nguyen, T. H.; Hettiarachchi, C.; Witkowski, M. E.; Drozdowski, W.; Birowosuto, M. D.; Wang, H.; Dang, C., Thermal Quenching and Dose Studies of X-ray Luminescence in Single Crystals of Halide Perovskites. *The Journal of Physical Chemistry C* **2018,** *122* (28), 16265-16273.

123. Protesescu, L.; Yakunin, S.; Bodnarchuk, M. I.; Krieg, F.; Caputo, R.; Hendon, C. H.; Yang, R. X.; Walsh, A.; Kovalenko, M. V., Nanocrystals of Cesium Lead Halide Perovskites (CsPbX(3), X = Cl, Br, and I): Novel Optoelectronic Materials Showing Bright Emission with Wide Color Gamut. *Nano Lett* **2015,** *15* (6), 3692-6.

124. Zhang, Y.; Sun, R.; Ou, X.; Fu, K.; Chen, Q.; Ding, Y.; Xu, L. J.; Liu, L.; Han, Y.; Malko, A. V.; Liu, X.; Yang, H.; Bakr, O. M.; Liu, H.; Mohammed, O. F., Metal Halide Perovskite Nanosheet for X-ray High-Resolution Scintillation Imaging Screens. *ACS Nano* **2019,** *13* (2), 2520-2525.

125. Dirin, D. N.; Protesescu, L.; Trummer, D.; Kochetygov, I. V.; Yakunin, S.; Krumeich, F.; Stadie, N. P.; Kovalenko, M. V., Harnessing Defect-Tolerance at the Nanoscale: Highly Luminescent Lead Halide Perovskite Nanocrystals in Mesoporous Silica Matrixes. *Nano Lett* **2016,** *16* (9), 5866-74.

126. Tong, Y.; Bladt, E.; Ayguler, M. F.; Manzi, A.; Milowska, K. Z.; Hintermayr, V. A.; Docampo, P.; Bals, S.; Urban, A. S.; Polavarapu, L.; Feldmann, J., Highly Luminescent Cesium Lead Halide Perovskite Nanocrystals with Tunable Composition and Thickness by Ultrasonication. *Angew Chem Int Ed Engl* **2016,** *55* (44), 13887-13892.

127. Tenuta, E.; Zheng, C.; Rubel, O., Thermodynamic origin of instability in hybrid halide perovskites. *Sci Rep* **2016,** *6*, 37654.

128. Zhu, Z.; Sun, Q.; Zhang, Z.; Dai, J.; Xing, G.; Li, S.; Huang, X.; Huang, W., Metal halide perovskites: stability and sensing-ability. *Journal of Materials Chemistry C* **2018,** *6* (38), 10121-10137.

129. Li, X.; Cao, F.; Yu, D.; Chen, J.; Sun, Z.; Shen, Y.; Zhu, Y.; Wang, L.; Wei, Y.; Wu, Y.; Zeng, H., All Inorganic Halide Perovskites Nanosystem: Synthesis, Structural Features, Optical Properties and Optoelectronic Applications. *Small* **2017,** *13* (9).

130. Liu, Z.; Shang, Q.; Li, C.; Zhao, L.; Gao, Y.; Li, Q.; Chen, J.; Zhang, S.; Liu, X.; Fu, Y.; Zhang, Q., Temperature-dependent photoluminescence and lasing properties of CsPbBr3 nanowires. *Applied Physics Letters* **2019,** *114* (10), 101902.

131. Xiang, X.; Ouyang, H.; Li, J.; Fu, Z., Humidity-sensitive CsPbBr3 perovskite based photoluminescent sensor for detecting Water content in herbal medicines. *Sensors and Actuators B: Chemical* **2021,** *346*.

132. Di Girolamo, D.; Dar, M. I.; Dini, D.; Gontrani, L.; Caminiti, R.; Mattoni, A.; Graetzel, M.; Meloni, S., Dual effect of humidity on cesium lead bromide: enhancement and degradation of perovskite films. *Journal of Materials Chemistry A* **2019,** *7* (19), 12292-12302.

133. Chen, J.; Liu, D.; Al-Marri, M. J.; Nuuttila, L.; Lehtivuori, H.; Zheng, K., Photo-stability of CsPbBr3 perovskite quantum dots for optoelectronic application. *Science China Materials* **2016,** *59* (9), 719-727.

134. Palazon, F.; Akkerman, Q. A.; Prato, M.; Manna, L., X-ray Lithography on Perovskite Nanocrystals Films: From Patterning with Anion-Exchange Reactions to Enhanced Stability in Air and Water. *ACS Nano* **2016,** *10* (1), 1224-30.

135. Pan, J.; Sarmah, S. P.; Murali, B.; Dursun, I.; Peng, W.; Parida, M. R.; Liu, J.; Sinatra, L.; Alyami, N.; Zhao, C.; Alarousu, E.; Ng, T. K.; Ooi, B. S.; Bakr, O. M.; Mohammed, O. F., Air-Stable Surface-Passivated Perovskite Quantum Dots for Ultra-Robust, Single- and Two-Photon-Induced Amplified Spontaneous Emission. *J Phys Chem Lett* **2015,** *6* (24), 5027-33.

136. Ahmed, Y.; Khan, B.; Bilal Faheem, M.; Huang, K.; Gao, Y.; Yang, J., Organic additives in all-inorganic perovskite solar cells and modules: from moisture endurance to enhanced efficiency and operational stability. *Journal of Energy Chemistry* **2022,** *67*, 361-390.

137. Huang, H.; Chen, B.; Wang, Z.; Hung, T. F.; Susha, A. S.; Zhong, H.; Rogach, A. L., Water resistant CsPbX3 nanocrystals coated with polyhedral oligomeric silsesquioxane and their use as solid state luminophores in all-perovskite white light-emitting devices. *Chem Sci* **2016,** *7* (9), 5699-5703.

138. Wang, H. C.; Lin, S. Y.; Tang, A. C.; Singh, B. P.; Tong, H. C.; Chen, C. Y.; Lee, Y. C.; Tsai, T. L.; Liu, R. S., Mesoporous Silica Particles Integrated with All-Inorganic CsPbBr3 Perovskite Quantum-Dot Nanocomposites (MP-PQDs) with High Stability and Wide Color Gamut Used for Backlight Display. *Angew Chem Int Ed Engl* **2016,** *55* (28), 7924-9.

139. Wang, C.; Lin, H.; Zhang, Z.; Qiu, Z.; Yang, H.; Cheng, Y.; Xu, J.; Xiang, X.; Zhang, L.; Wang, Y., X-ray excited CsPb(Cl,Br)3 perovskite quantum dots-glass composite with long-lifetime. *Journal of the European Ceramic Society* **2020,** *40* (5), 2234-2238.

140. Cao, F.; Yu, D.; Ma, W.; Xu, X.; Cai, B.; Yang, Y. M.; Liu, S.; He, L.; Ke, Y.; Lan, S.; Choy, K. L.; Zeng, H., Shining Emitter in a Stable Host: Design of Halide Perovskite Scintillators for X-ray Imaging from Commercial Concept. *ACS Nano* **2020,** *14* (5), 5183-5193.

141. Zhang, Z.; Dierks, H.; Lamers, N.; Sun, C.; Nováková, K.; Hetherington, C.; Scheblykin, I. G.; Wallentin, J., Single-Crystalline Perovskite Nanowire Arrays for Stable X-ray Scintillators with Micrometer Spatial Resolution. *ACS Applied Nano Materials* **2022,** *5* (1), 881-889.

142. Jellicoe, T. C.; Richter, J. M.; Glass, H. F.; Tabachnyk, M.; Brady, R.; Dutton, S. E.; Rao, A.; Friend, R. H.; Credgington, D.; Greenham, N. C.; Bohm, M. L., Synthesis and Optical Properties of Lead-Free Cesium Tin Halide Perovskite Nanocrystals. *J Am Chem Soc* **2016,** *138* (9), 2941-4.

143. Cao, J.; Guo, Z.; Zhu, S.; Fu, Y.; Zhang, H.; Wang, Q.; Gu, Z., Preparation of Lead-free Two-Dimensional-Layered (C8H17NH3)2SnBr4 Perovskite Scintillators and Their Application in X-ray Imaging. *ACS Applied Materials & Interfaces* **2020,** *12* (17), 19797-19804.

144. Billen, P.; Leccisi, E.; Dastidar, S.; Li, S.; Lobaton, L.; Spatari, S.; Fafarman, A. T.; Fthenakis, V. M.; Baxter, J. B., Comparative evaluation of lead emissions and toxicity potential in the life cycle of lead halide perovskite photovoltaics. *Energy* **2019,** *166*, 1089-1096.

145. Barrelet, C. J.; Greytak, A. B.; Lieber, C. M., Nanowire Photonic Circuit Elements. *Nano Letters* **2004,** *4* (10), 1981-1985.

146. Li, H.; Yang, H.; Yuan, R.; Sun, Z.; Yang, Y.; Zhao, J.; Li, Q.; Zhang, Z., Ultrahigh Spatial Resolution, Fast Decay, and Stable X-Ray Scintillation Screen through Assembling CsPbBr3 Nanocrystals Arrays in Anodized Aluminum Oxide. *Advanced Optical Materials* **2021**.

147. Gandini, M.; Villa, I.; Beretta, M.; Gotti, C.; Imran, M.; Carulli, F.; Fantuzzi, E.; Sassi, M.; Zaffalon, M.; Brofferio, C.; Manna, L.; Beverina, L.; Vedda, A.; Fasoli, M.; Gironi, L.; Brovelli, S., Efficient, fast and reabsorption-free perovskite nanocrystal-based sensitized plastic scintillators. *Nature Nanotechnology* **2020,** *15* (6), 462-468.

148. Wang, Z.; Sun, R.; Liu, N.; Fan, H.; Hu, X.; Shen, D.; Zhang, Y.; Liu, H., X-Ray imager of 26-μm resolution achieved by perovskite assembly. *Nano Research* **2022,** *15* (3), 2399-2404.

149. Chen, Q.; Wu, J.; Ou, X.; Huang, B.; Almutlaq, J.; Zhumekenov, A. A.; Guan, X.; Han, S.; Liang, L.; Yi, Z.; Li, J.; Xie, X.; Wang, Y.; Li, Y.; Fan, D.; Teh, D. B. L.; All, A. H.; Mohammed, O. F.; Bakr, O. M.; Wu, T.; Bettinelli, M.; Yang, H.; Huang, W.; Liu, X., All-inorganic perovskite nanocrystal scintillators. *Nature* **2018,** *561* (7721), 88-93.

150. Wang, L.; Fu, K.; Sun, R.; Lian, H.; Hu, X.; Zhang, Y., Ultra-stable CsPbBr3 Perovskite Nanosheets for X-Ray Imaging Screen. *Nanomicro Lett* **2019,** *11* (1), 52.

151. Lü, Z.-W.; Wei, G.-X.; Wang, H.-Q.; Guan, Y.; Jiang, N.; Liu, Y.-Y.; Li, Z.; Qin, H.; Liu, H.-Q., New flexible CsPbBr3-based scintillator for X-ray tomography. *Nuclear Science and Techniques* **2022,** *33* (8).

152. Dierks, H.; Zhang, Z.; Lamers, N.; Wallentin, J., 3D X-ray microscopy with a CsPbBr3 nanowire scintillator. *Nano Research* **2022**.

153. Nagarkar, V. V.; Gupta, T. K.; Miller, S. R.; Klugerman, Y.; Squillante, M. R.; Entine, G., Structured CsI(Tl) scintillators for X-ray imaging applications. *IEEE Transactions on Nuclear Science* **1998,** *45* (3), 492-496.

154. Hormozan, Y.; Sychugov, I.; Linnros, J., High-resolution x-ray imaging using a structured scintillator. *Med Phys* **2016,** *43* (2), 696-701.

155. Zhou, J.; An, K.; He, P.; Yang, J.; Zhou, C.; Luo, Y.; Kang, W.; Hu, W.; Feng, P.; Zhou, M.; Tang, X., Solution-Processed Lead-Free Perovskite Nanocrystal Scintillators for High-Resolution X-Ray CT Imaging. *Advanced Optical Materials* **2021,** *9* (11).

156. Besnard, C.; Harper, R. A.; Moxham, T. E. J.; James, J. D.; Storm, M.; Salvati, E.; Landini, G.; Shelton, R. M.; Korsunsky, A. M., 3D analysis of enamel demineralisation in human dental caries using high-resolution, large field of view synchrotron X-ray micro-computed tomography. *Materials Today Communications* **2021,** *27*, 102418.

157. Meyer, Q.; Hack, J.; Mansor, N.; Iacoviello, F.; Bailey, J. J.; Shearing, P. R.; Brett, D. J. L., Multi-Scale Imaging of Polymer Electrolyte Fuel Cells using X-ray Micro- and Nano-Computed Tomography, Transmission Electron Microscopy and Helium-Ion Microscopy. *Fuel Cells* **2019,** *19* (1), 35-42.

158. Cakmak, E.; Bingham, P.; Cunningham, R. W.; Rollett, A. D.; Xiao, X.; Dehoff, R. R., Non-destructive characterization of additively manufactured components with x-ray computed tomography for part qualification: A study with laboratory and synchrotron x-rays. *Materials Characterization* **2021,** *173*, 110894.

159. Walsh, C. L.; Tafforeau, P.; Wagner, W. L.; Jafree, D. J.; Bellier, A.; Werlein, C.; Kühnel, M. P.; Boller, E.; Walker-Samuel, S.; Robertus, J. L.; Long, D. A.; Jacob, J.; Marussi, S.; Brown, E.; Holroyd, N.; Jonigk, D. D.; Ackermann, M.; Lee, P. D., Imaging intact human organs with local resolution of cellular structures using hierarchical phase-contrast tomography. *Nature Methods* **2021,** *18* (12), 1532-1541.

160. Schwyn, D. A.; Mokso, R.; Walker, S. M.; Doube, M.; Wicklein, M.; Taylor, G. K.; Stampanoni, M.; Krapp, H. G., High-Speed X-ray Imaging on the Fly. *Synchrotron Radiation News* **2013,** *26* (2), 4-10.

161. Garcia-Moreno, F.; Kamm, P. H.; Neu, T. R.; Bulk, F.; Mokso, R.; Schleputz, C. M.; Stampanoni, M.; Banhart, J., Using X-ray tomoscopy to explore the dynamics of foaming metal. *Nat Commun* **2019,** *10* (1), 3762.

162. Havariyoun, G.; Vittoria, F. A.; Hagen, C. K.; Basta, D.; Kallon, G. K.; Endrizzi, M.; Massimi, L.; Munro, P.; Hawker, S.; Smit, B.; Astolfo, A.; Larkin, O. J.; Waltham, R. M.; Shah, Z.; Duffy, S. W.; Nelan, R. L.; Peel, A.; Suaris, T.; Jones, J. L.; Haig, I. G.; Bate, D.; Olivo, A., A compact system for intraoperative specimen imaging based on edge illumination x-ray phase contrast. *Phys Med Biol* **2019,** *64* (23), 235005.

163. Langer, M.; Zhang, Y.; Figueirinhas, D.; Forien, J.-B.; Mom, K.; Mouton, C.; Mokso, R.; Villanueva-Perez, P., PyPhase - a Python package for X-ray phase imaging. *Journal of Synchrotron Radiation* **2021,** *28* (4), 1261-1266.

164. Lohse, L. M.; Robisch, A.-L.; Töpperwien, M.; Maretzke, S.; Krenkel, M.; Hagemann, J.; Salditt, T., A phase-retrieval toolbox for X-ray holography and tomography. *Journal of Synchrotron Radiation* **2020,** *27* (3).

165. Zhang, Y.; Andreas Noack, M.; Vagovic, P.; Fezzaa, K.; Garcia-Moreno, F.; Ritschel, T.; Villanueva-Perez, P., PhaseGAN: a deep-learning phase-retrieval approach for unpaired datasets. *Opt. Express* **2021,** *29* (13), 19593-19604.

Printed by Media-Tryck, Lund 2023 NORDIC SWAN ECOLABEL 3041 0903

LUND UNIVERSITY

ISBN 978-91-8039-590-8
Division of Synchrotron Radiation Research
Department of Physics
Faculty of Science
Lund University